

11 SEP 1997

Technical Report UILU-ENG 97-0510

AAE 97-10

FINAL TECHNICAL REPORT

For research supported by
AFOSR Contract No. F49620-95-1-0363
for period 08/30/95 to 07/30/97

FUNDAMENTALS OF 1 kW HYDRAZINE ARCJET THRUSTERS

Prepared by

Herman Krier ⁽¹⁾, Rodney L. Burton ⁽²⁾
N.T. Tiliakos ⁽³⁾, and J. Lu ⁽³⁾

Department of Aeronautical and Astronautical Engineering
University of Illinois at Urbana-Champaign
104 S. Wright Street
Urbana, IL 61801

Work supported by

Air Force Office of Scientific Research
Program Manager: Dr. Mitat Birkan

19971002 016

-
- (1) Co-Principal Investigator; Department of Mechanical and Industrial Engineering
 - (2) Co-Principal Investigator; Dept. Of Aeronautical and Astronautical Engineering
 - (3) Graduate Research Assistants; Ph.D. Candidates

APPROVED FOR PUBLIC RELEASE; DISTRIBUTION UNLIMITED

September, 1997

AFOSR-TR-97-0341

REPORT DOCUMENTATION PAGEFORM APPROVED
OMB No. 0704-0188

Public reporting burden for this collection of information is estimated to average 1 hour per response, including the time for reviewing instructions, searching existing data sources, gathering and maintaining the data needed and completing and reviewing the collection of information. Send comments regarding this burden estimate or any other aspect of the collection of information, including suggestions for reducing the burden to: Washington Headquarters Services, Directorate for Information Operations and Reports, 1216 Jefferson Davis highway, Suite 1204, Arlington, VA 22202-4302 and to the Office of Management and Budget, Paperwork Reduction Project (0704-0188), Washington, DC 20503

1. AGENCY USE ONLY (Leave Blank)		Report Date: August 30, 1997		3. REPORT TYPE AND DATES COVERED Final Technical Report; Aug 30, 1995 - July 30, 1997	
4. TITLE AND SUBTITLE OF REPORT FUNDAMENTALS OF 1 KW HYDRAZINE ARCJET THRUSTERS				5. FUNDING NUMBERS AFOSR; F49620-95-1-0363	
6. AUTHOR(S) H. Krier, R.L. Burton, N.T. Tiliakos, and J. Lu					
7. PERFORMING ORGANIZATION NAME(S) AND ADDRESS(ES) University of Illinois at Urbana-Champaign c/o Grants and Contracts Office 109 Coble Hall; 801 South Wright St. Champaign, IL 61820-6242				8. PERFORMING ORGANIZATION REPORT NUMBER UIU ENG 97- 0510 (AAE 97-10)	
9. SPONSORING/MONITORING AGENCY NAME(S) AND ADDRESS(ES) AFOSR/NA 110 Duncan Avenue; Suite B115 Bolling AFB, DC 20332-0001				10. SPONSORING/MONITORING ORGANIZATION REPORT NUMBER	
11. SUPPLEMENTARY NOTES:					
12a. DISTRIBUTION AVAILABILITY STATEMENT Approved for Public Release; Distribution Unlimited				12b. DISTRIBUTION CODE	
13. ABSTRACT (Maximum 200 words) This final technical report summarizes the research carried out by our group concerned with the fundamentals of hydrazine 1 kW arcjet thrusters. Section I presents modeling analysis that predict the nonequilibrium plasmadynamic processes by solving the two-dimensional, axisymmetric, chemical nonequilibrium viscous flows including heat transfer to the anode con-divergent nozzle. Section II presents the coupling of cathode sheath potential models necessary to account for the total voltage operating at 10 A. Excellent agreement is predicted to match data for a 1 kW hadrazine arcjet. Section III presents experimental studies of the internal anode sheath layer by utilizing an array of 14 electrostatic micro-probes. Axial and azimuthal distributions of such plasma properties as the floating potential, anode sheath potential, wall current density, electron number density and electron temperature are reported for power/mass flow ratios ranging between 18 to 30 MJ/kg. Excellent agreement between the data and the numerical models (Sec I and II) is found.					
14. SUBJECT TERMS Arcjet (Electric) Propulsion; Probe Diagnostics; Plasmadynamics and Thermophysics				15. NUMBER OF PAGES: 123	
				16. PRICE CODE	
17. SECURITY CLASSIFICATION OF REPORT: UNCLASSIFIED/UNLIMITED		18. SECURITY CLASSIFICATION OF THIS PAGE UNCLASSIFIED		19. SECURITY CLASSIFICATION OF ABSTRACT UNCLASSIFIED	
				20. LIMITATION OF ABSTRACT NONE	

Technical Report UILU-ENG 97-0510

AAE 97-10

FINAL TECHNICAL REPORT

For research supported by
AFOSR Contract No. F49620-95-1-0363
for period 08/30/95 to 07/30/97

FUNDAMENTALS OF 1 kW HYDRAZINE ARCJET THRUSTERS

Prepared by

Herman Krier ⁽¹⁾, Rodney L. Burton ⁽²⁾
N.T. Tiliakos ⁽³⁾, and J. Lu ⁽³⁾

Department of Aeronautical and Astronautical Engineering
University of Illinois at Urbana-Champaign
104 S. Wright Street
Urbana, IL 61801

Work supported by

Air Force Office of Scientific Research
Program Manager: Dr. Mitat Birkan

-
- (1) Co-Principal Investigator; Department of Mechanical and Industrial Engineering
 - (2) Co-Principal Investigator; Dept. Of Aeronautical and Astronautical Engineering
 - (3) Graduate Research Assistants; Ph.D. Candidates

APPROVED FOR PUBLIC RELEASE; DISTRIBUTION UNLIMITED

September, 1997

Table of Contents

	<u>Page</u>
Form DD298	i
Abstract	3
I. Modeling Plasma Processes in 1kW Hydrazine Arjets Thrusters	5
II. Collisionless Cathode Sheath Models to Predict Power Distribution in 1 kW Hydrazine Arcjets	44
III. Arjet Anode Plasma Measurements Using Electrostatic Probes	81

Abstract

Section I.

This section presents predictions of a nonequilibrium 1-kW hydrazine arcjet model with sensitivity studies on generalized Ohm's Law and electron-molecule inelastic collision factor δ . The model treats steady-state, two-dimensional, axisymmetric, two temperature (electrons and heavy species), chemical nonequilibrium viscous flow, and includes flow swirl and anode heat transfer in a converging-diverging nozzle. Key results indicate that the arcjet flow is in thermal and chemical nonequilibrium. Sensitivity studies show that the modeling of the inelastic coupling of electrons-molecules significantly alters the predicted anode current attachment location and subsequently the predicted plasma voltage drop, and that the electron pressure gradient term does not significantly affect the current distribution. With an appropriate choice of the electron-molecule inelastic collision factor δ , and adopting values from the literature for the cathode and anode sheath voltages, the model predictions are in good agreement with the experimental values.

Section II.

This Section presents two different approaches to predict the cathode sheath potential necessary to account for the total voltage in a 1 kW hydrazine arcjet operating at 10 A. The first approach is a modification of the sheath model first developed by K. Fujita, and the second approach is the cathode sheath model developed by K. D. Goodfellow. The Fujita cathode sheath model is modified here to calculate the cathode sheath potential, electron temperature and number density at the cathode sheath edge of a 1 kW hydrazine arcjet, using near-cathode bulk plasma properties from a nonequilibrium numerical model developed by Megli, Krier, and Burton. The sheath potential is sensitive to current attachment area, cathode tip temperature, and the properties of the near-cathode bulk plasma. For a 1 kW hydrazine arcjet operating at 10 A and 50 mg/s, the sheath potential from the modified Fujita model is approximately -30 volts for a pure tungsten cathode with $2 \times 10^{-8} \text{ m}^2$ attachment area, and 3680 K cathode tip temperature.

The Goodfellow model consists of a near-cathode plasma model and a thermal model of the cathode. The plasma model contains models for the surface, sheath, presheath and ionization regions. The input parameters for the combined model are the total pressure, the arcjet current, and one of the following: cathode temperature, sheath voltage, or attachment area/current density. The cathode temperature is the best understood of these three parameters and is used here. Comparisons between the two cathode models have shown good agreement for the determinations of the sheath voltage, electron temperature and the electron number density. However, a factor of 10 or more is calculated for the electric field at the cathode surface.

Section III.

A 1 kW hydrazine arcjet thruster has been modified for internal probing of the anode sheath boundary layer with an array of fourteen electrostatic micro-probes flush-mounted into the anode body. Axial and azimuthal distributions of the plasma properties floating potential, anode sheath potential, wall current density, electron number density and electron temperature have been obtained for arc currents between 7.8 and 10.6 A and propellant flow rates of 40 to 60 mg/s. P/\dot{m} ranged from 18.8 to 27.4 MJ/kg. Azimuthal symmetry has been verified for all arcjet operating conditions. The electron temperature data show that the near-anode plasma is highly non-equilibrium. Most of the current density and anode heating is located within 2-4 mm of the constrictor exit, with the location affected more by mass flow rate than by arc current. The anode heating distribution is closely coupled to current density and accounts for ~18-24% of the total input power. Reasonable agreement between a numerical model and the experimental results is found for a constant value of the electron inelastic energy loss factor.

Modeling Plasma Processes in 1 kW Hydrazine Arcjet Thrusters

Thomas W. Megli,^{*} Junqing Lu,^{**} Herman Krier,[†] and Rodney L. Burton^{††}

University of Illinois at Urbana-Champaign

Urbana, IL 61801

Abstract

This paper presents predictions of a nonequilibrium 1-kW hydrazine arcjet model with sensitivity studies on generalized Ohm's Law and electron-molecule inelastic collision factor δ . This model treats steady-state, two-dimensional, axisymmetric, two temperature (electrons and heavy species), chemical nonequilibrium viscous flow, and includes flow swirl and anode heat transfer in a converging-diverging nozzle. Key results indicate that the arcjet flow is in thermal and chemical nonequilibrium. Sensitivity studies show that the modeling of the inelastic coupling of electrons-molecules significantly alters the predicted anode current attachment location and subsequently the predicted plasma voltage drop, and that the electron pressure gradient term does not significantly affect the current distribution. With an appropriate choice of the electron-molecule inelastic collision factor δ , and adopting values from the literature for the cathode and anode sheath voltages, the model predictions are in good agreement with the experimental values.

Nomenclature

B	magnetic field [T]
CE	chemical equilibrium
CNE	chemical nonequilibrium
C_{pe}	thermodynamic function for electrons [J]
e	electric charge [C]
E	electric field [Volts/m]
elst	elastic energy transfer [W/m ³]
f	mass fraction of un-ionized atoms; or electron energy distribution function [eV ^{3/2}]
g₀	gravitational acceleration at sea level [m/s ²]
I	current [A]
I_{sp}	specific impulse [s]
j	current density [A/m ²]
k_b	Boltzmann's constant [J/K]
L_e	individual energy loss rates [J/s]
m_i	mass of species i [kg]
\dot{m}	mass flow rate [mg/s]
N	total particle number density [m ⁻³]
n_e	electron number density [m ⁻³]
n_i	number density of the heavy species i [m ⁻³]
P	electric power [W]
p	pressure [N/m ²]
p_e	electron pressure [N/m ²]
Q_{ei}	collision cross section between the electrons and the heavy species i [m ²]
T_a	anode temperature [K]
T_e	electron temperature [K]
T_g	heavy species temperature [K]

u	axial velocity [m/s]
\mathbf{v}	velocity vector [m/s]
V	voltage [volts]
w	azimuthal swirl velocity [m/s]
x, r, θ	cylindrical coordinates
x_{cat}	cathode gap [mm]
x_i	mole fraction of species i
y_e	mass fraction of electrons
α	nozzle half angle; or degree of ionization
δ_i	Electron-molecule inelastic loss factor for species i
ε	electron energy [eV]
η	thrust efficiency
λ_e	electron thermal conductivity [W/m-K]
ρ	mass density [kg/m ³]
σ	electric conductivity [ohm-m] ⁻¹
τ_{In}	collision time for ions and neutrals [s]
$\bar{\nu}_{ei}$	average collision frequencies between electrons and heavy species i [1/s]

Introduction

A challenging and important area of satellite propulsion is the application of low power thrusters, and in particular, the arcjet thruster. Typically, a specific impulse significantly higher than 400 seconds is called for, in order to provide greatly increased payload mass fraction for high ΔV missions such as LEO-GEO orbit transfer. Further development requires an understanding of the internal energy transfer and flow processes in 1-kW class hydrazine arcjets, and in particular the modeling of the thermal and chemical nonequilibrium in the flow. This paper continues the development of the 1-kW hydrazine arcjet model developed earlier by Megli, Krier, and Burton (the MKB model).¹

It has been determined empirically that for arcjets in the 1-kW range, the most important issues are constrictor and anode life, which are mostly affected by heating in the constrictor region. An understanding of current attachment and anode heating is required, and can be achieved with a validated plasmadynamics model. Besides the MKB model, two existing hydrogen arcjet models^{2,3} are capable of modeling two-dimensional thermal and chemical nonequilibrium arcjet physics. The emphasis here has been development of a thermo-physical flow modeling tool, coupled with detailed experimental boundary measurements of plasma parameters, with model validation as the primary goal. This approach is expected to produce a relatively complete understanding of the plasmadynamics of 1-kW arcjets, and to predict arcjet performance at high P/\dot{m} (power / mass flow rate).

Description of the Arcjet Thruster

The azimuthally symmetric arcjet is shown schematically in Fig. 1. The fluid dynamics and energy transfer within the thruster are nonlinear and strongly coupled. The propellant is injected upstream of the constrictor, typically with an azimuthal (or 'swirl') velocity component. The energy conversion mechanism for an arcjet is an arc discharge, produced by a voltage difference between the thruster nozzle, which is the anode, and a conical cathode on the upstream side of the constrictor. Electron current is supplied by field-enhanced thermionic emission from

the cathode tip. Typical operating voltages for 1-kW class arcjets are about 115 V DC at a current of $I = 10$ A. The arc current distribution depends on several factors in addition to the geometry, and is coupled to the propellant mass flow rate, composition, thermal properties, electric conductivity, and gas-dynamic properties.

Both chemical and thermal processes in the arcjet are nonequilibrium. Arc current is converted to electron thermal energy through ohmic dissipation. The electrons transfer thermal energy to the heavy species in the arc plasma through collisions. This thermal energy is then converted to kinetic energy and therefore thrust as the fluid accelerates through the nozzle. In regions of low pressure and/or elevated ohmic heating, collisional coupling between electrons and heavy species may not establish equal gas and electron temperatures. Additionally, flow velocities are large so that fluid residence time in the nozzle is on the order of $1 \mu\text{s}$. Thus, much of the energy invested in dissociation and ionization is frozen. The pressure drops from roughly 1 atm at the constrictor to millitorr conditions at the exit. The radial diffusion of electrons from the arc core is important in determining the arc structure.

Small mass flow rates of tens of milligrams per second are used to operate the thruster at a specific power P/\dot{m} of 15 - 45 MJ/kg. Typical 1-kW class arcjet thrusters have constrictor diameters of 0.6 mm, with nozzle expansion half-angles of 20° and exit diameters of 9 mm. Velocities vary from approximately 10 km/s on the centerline to zero at the wall with gas temperatures ranging from 20,000 K near the cathode tip to roughly 1500 K at the anode.¹ Despite the high velocities, the arcjet is a viscous, low Reynolds number device ($Re = O(100 - 1000)$) due to low mass flow rates, high gas temperatures, and mm-size dimensions.

The thrust and specific impulse produced by an arcjet are determined by several factors including the power transferred to the propellant, the extent of both thermal and chemical nonequilibrium, the propellant gas mixture, viscous losses, and the arcjet nozzle geometry. Factors which detract from performance include heat loss to the anode and the voltage sheaths at the electrodes. A comprehensive model of an arcjet thruster is highly complex, and must include plasmadynamic, fluid dynamic, and surface and volumetric heat transfer phenomena.^{1,4}

The energy loss mechanisms can be more readily appreciated by examining the thrust efficiency η of the device, which is a measure of the ratio of the directed kinetic power of the exiting propellant to the electric power input:

$$\eta = \frac{\dot{m}u^2}{2P} = \frac{\dot{m}I_{sp}^2 g_0^2}{2P} \quad (1)$$

The thrust efficiencies of 35% typical of 1-kW arcjets clearly indicate significant room for design improvements through the reduction of frozen flow, viscous, electric sheath, and heat transfer losses.

The MKB Arcjet Model

The model is a steady, two-dimensional, axisymmetric, two-temperature, chemical nonequilibrium model which includes flow swirl and anode heat transfer in a converging-diverging nozzle geometry with variable cathode gap. The model assumes the radiating plasma to be optically thin.¹ The gas is simulated hydrazine, $0.5\text{N}_2 + \text{H}_2$. Input parameters are thruster geometry, mass flow rate, total applied current, and the inlet flow swirl velocity.

The model predicts thrust, specific impulse, and internal fields for pressure p , mass density ρ , seven species density n_i , and temperatures of the anode T_a , electrons T_e , and heavy species T_g . Additionally, the model predicts the current density distribution j , voltage potential V , and velocity components u , v , and w .

Equations are presented in Refs. 1 and 4 to model the following: (a) fluid dynamics, (b) electron and heavy species energy, (c) electromagnetics, (d) species number densities, (e) transport coefficients, and (f) boundary conditions. The arcjet geometry is described as (x, r, θ) , representing the axial, radial, and the azimuthal coordinates.

The important assumptions are:

- (a) axisymmetric, steady, continuum, and viscous nozzle flow;
- (b) Maxwellian energy distributions for electrons and the heavy species;

- (c) independent relations for electron energy (temperature) and heavy species energy (temperature) for atoms, molecules, and ions, coupled by elastic and inelastic collisions and radiation;
- (d) for N_2H_4 (hydrazine) arc-heating, finite-rate chemistry for dissociation, ionization and their reverse reactions (considers 11 reactions);
- (e) generalized Ohm's Law for current density;
- (f) two-dimensional heat conduction in anode;
- (g) multi-component energy-averaged collision integrals for calculations of the mixture transport properties (viscosity, diffusivity, and conductivity);
- (h) neutral plasma, i.e., $n_e = n_{H^+} + n_{N^+}$.
- (i) ideal (mixture) two-temperature plasma equation of state: $p = n_e k_b T_e + (n_{N_2} + n_{H_2} + n_N + n_H + n_e) k_b T_g$;
- (j) individual species conservation and diffusion (affects energy conservation as "chemical source terms.");
- (k) total pressure (≈ 3 atm) fixes mass flow at inlet;
- (l) at the supersonic nozzle exit plane, the static pressure is extrapolated from flow interior, despite the presence of a 'mixed', supersonic and (annular) subsonic flow;
- (m) anode is modeled as an equipotential ($V=0$) surface;
- (n) a cathode sheath voltage of 30 volts (from cathode sheath models⁵) and an anode sheath voltage of 11 volts (from anode probe measurements⁶) are added to the plasma voltage to yield the total arcjet voltage; and
- (o) geometry is modeled as the NASA 1-kW arcjet.⁷

The computational grids are composed of 62 axial by 17 radial nodes for the plasma, and 62 axial by 9 radial nodes for the anode domain.¹ The grids are tuned such that denser grids are located near the electrode surfaces and the constrictor, where gradients in plasma properties are large.¹ A recent grid study demonstrated that this grid system cannot be refined without violating the continuum assumption of the model.⁵

Baseline Flowfield Results for Hydrazine

The characteristics of the plasma flowfield were investigated for the NASA-Lewis 1-kW thruster.^{1,4,8} In Ref. 8 chemical equilibrium (CE) and chemical nonequilibrium (CNE) predictions are compared for the velocity, temperature, current density, and number densities. These results correspond to cases 1 and 2 listed in Table 1.

The CE and CNE hydrazine simulations are systematically compared in Figs. 2 and 3, demonstrating the necessity of CNE formulation. At the cathode tip the current density is 40,000 A/cm² for the CE case. A peak anode attachment current density of 18 A/cm² is noted at a location of $x \approx 11$ mm, or roughly 5 mm downstream of the constrictor. The anode temperature increases from the upstream boundary value of 1000 K to about 1300 K near the exit plane. For the CNE hydrazine simulation, the peak anode current density of $j \approx 15$ A/cm² occurs at $x \approx 8$ mm, upstream from that for the CE case. The CNE anode temperature is somewhat lower than for CE, with a value of about 1200 K at the exit plane.

The marked difference in the current attachment predictions is clearly illustrated in Fig. 2, where the anode current densities are indicated. For CNE, a more diffuse, bimodal distribution is noted, with the attachment closer to the constrictor. The voltage prediction for CNE (115 volts) is 23% lower than that for CE (141 volts), as shown in Table 1, casting doubt about the CE assumption.

The anode/plasma interface T_e distributions are indicated in Fig. 3. A high degree of thermal nonequilibrium is noted, with maximum electron temperatures of approximately 8,000 K and 12,000 K for the CE and CNE simulations respectively. The thermal nonequilibrium condition largely controls the near-anode electron densities, which in turn determine the electric conductivity of the plasma. For the CNE simulations, increased ionization rate coefficients are predicted by the elevated T_e . The mechanism of arc attachment captured by this model is the increased ionization fractions predicted by the relatively high near-anode T_e , although these fractions are only $O(10^{-4})$. Radial diffusion of electrons from the arc core also enhances the

electron populations. These processes give a finite, non-zero prediction for the electric conductivity near the electrodes where T_g is low.

Although both CE and CNE results indicate significant thermal nonequilibrium near the anode, the central region of the arc is near equilibrium.^{1,4,8} For example, a maximum $T_g \approx 22,000$ K occurs near the center of the constrictor for CE hydrazine, and a maximum $T_e \approx 25,000$ K occurs at the same location.^{4,8} The higher ionization fractions on centerline efficiently couple the electron and gas temperatures through coulombic collisions between the electrons and ions. The results for CNE hydrazine are similar, with maxima of $T_g \approx 22,000$ K and $T_e \approx 28,000$ K.^{1,8}

Arcjet conditions can indicate when finite-rate chemistry must be included to predict frozen flow losses accurately. Bose¹⁰ warned that the results from Saha's equation would be incorrect if the electron temperature is more than twice the heavy species temperature. Richley and Tuma¹¹ also recommended that the difference between the electron and the heavy temperature should not exceed 2000 K, otherwise, finite-rate chemistry should replace the Saha equation. CNE conditions therefore exist here.

In Figs. 4 and 5, exit plane predictions of electron number density n_e are presented. The Saha-predicted centerline density for CE (Fig. 4) hydrazine is $n_e = 1.6 \times 10^{11} \text{ cm}^{-3}$ while the density for CNE (Fig. 5) is 3 orders of magnitude higher at $n_e = 1.6 \times 10^{14} \text{ cm}^{-3}$. The CNE predictions for centerline distributions of electron density are in better agreement with the internal nozzle measurements of Zube and Myers.^{1,4,9}

Also shown in Figs. 4 and 5 are T_e and T_g profiles. More thermal nonequilibrium is indicated for the CE case with $T_e/T_g \approx 2.0$ at the centerline, while the CNE case is near equilibrium at $T_e/T_g \approx 1.1$. The degree of thermal nonequilibrium scales inversely with electron density, so that the lower electron concentrations predicted for CE translate directly to higher predicted exit plane electron temperatures.

The reason for CNE is two-fold. First, competing rate processes have different temperature dependencies which are not captured by the CE formulation. Second, the arcjet flow has high velocity and low residence time inside the nozzle, thus the reactions do not have enough

time to reach the equilibrium state. The MKB model results indicate that the electron temperature is an order of magnitude higher than the heavy species temperature near the anode and the fluid residence time in the nozzle is on the order of 1 μ s, so that finite-rate chemistry (CNE) should be used.

The results for H- and N-atom mole fractions at the arcjet exit plane are shown in Fig. 6. The CNE radial profiles are generally smoother in the central portion of the flow due to radial diffusion. The CE predictions for N-atom mole fractions are several orders of magnitude lower than those for CNE, with centerline values of 1×10^{-5} and 3×10^{-2} , respectively. This is in contrast to the centerline predictions for H-atom mole fractions, where CE calculations indicate a significantly higher H dissociation fraction in the center of the flow. The respective centerline mole fractions for H in CE and CNE are 0.35 and 0.04.

Results for H_2 and N_2 mole fractions are shown in Fig. 7. Again, the effects of radial diffusion are evident, with smoother profiles indicated for the CNE predictions, and elevated molecular mole fractions in the hotter central region of the flow. At the anode wall ($r \approx 4.8$ mm) both the CNE and CE mole fraction predictions are approximately that of the inflowing propellant ($N_2 + 2H_2$ for simulated hydrazine) with $x_{H_2} \approx 0.67$ and $x_{N_2} \approx 0.33$. Centerline H_2 mole fractions of 0.58 and 0.38 are indicated for the CNE and CE simulations, respectively. The diffusive effects are less pronounced for the heavier N_2 molecule. Centerline values for the respective CNE and CE simulations are $x_{N_2} \approx 0.30$ and 0.28, respectively.

Voltage contours are shown in Fig. 8. (Note that the sheath voltage contributions have not been added to the contours shown here.) Even outside the sheath, strong electric fields are noted near the electrode surfaces. At the cathode tip, the plasma voltage decreases axially from 74 volts to 67 volts (only the *magnitude* of the voltages is listed, following the convention for arcjet literature) over a distance of $\Delta x \approx 0.03$ mm, indicating a strong axial electric field strength of $E \approx 230$ V/mm. The net axial voltage rise across the constrictor is roughly $\Delta V \approx 34$ volts, corresponding to an average electric field strength of $E \approx 136$ V/mm. The plasma voltage drop predicted from current conservation and Ohm's Law is 74 volts. The total arcjet voltage is 115

volts, including 30 volts from the cathode sheath⁵ and 11 volts from the anode sheath⁶. This indicates that 56% of the arcjet power is deposited in the constrictor. Strong radial gradients in voltage are also noted near the anode. A 13 volt drop at an axial location of $x \approx 7$ mm occurs over a radial distance of $\Delta r \approx 0.05$ mm. This gives an estimate for the radial electric field strength of $E \approx 260$ V/mm.

Ohmic heating contours proportional to j^2/σ are plotted in Fig. 9. In the constrictor the small cross sectional area and the strong axial electric fields produce high current density and electric heating of the plasma. The peak ohmic heating just off the cathode tip is $j^2/\sigma \approx 3.6 \times 10^{13}$ W/m³ (not shown in Fig. 9). The heating is largely confined to the central region of the flow, as indicated by high radial gradients in j^2/σ . Strong radial electric fields produce elevated heating near the anode, $\sim 10^{10}$ W/m³. The j^2/σ distribution is qualitatively similar to the electron temperature. The high near-anode heating couples with low electron populations to produce the high degree of thermal nonequilibrium.

Ionization fraction α -contours are shown in Fig. 10. The plasma near the cathode tip is highly ionized, with $\alpha \geq 0.6$. In the constrictor region, ionization levels of $\alpha \geq 0.01$ are maintained over roughly 50% of the nozzle radius. The distribution of electric conductivity σ is largely determined by the ionization fraction and the electron temperature. In the hot, highly ionized arc region, the electric conductivity is $\sigma \approx 5,000 - 10,000$ [ohm-m]⁻¹, corresponding to the Spitzer limit, where σ is controlled by large cross-section electron-ion coulomb collisions. The electric conductivity decreases with radius, eventually reaching a level of $\sigma \approx 0.7$ [ohm-m]⁻¹ at the current attachment region of the anode. The flow is molecule-rich in this region. The plasma conductivity near the anode is primarily determined by the elevated electron temperature, the electron-molecule collision cross sections, and the finite, non-zero ionization levels of $\alpha \approx 10^{-4}$.

Generalized Ohm's Law

The above results are obtained with the electron pressure gradient term neglected in generalized Ohm's Law. There were concerns that the electron gradient term may significantly

affect the current distribution in the arcjet. Moreover, there are uncertainties in the value of the electron-molecule inelastic collision factor, δ . Hence, the sensitivities of the MKB model results to the electron pressure gradient term and the δ factor were investigated.

The correct approach to the arc attachment problem is to model the anode as an equipotential surface and allow the current distribution to be a model output which is independent of artificial restrictions. This self-consistent approach solves the current distribution and electric field simultaneously, for which the current distribution is properly coupled to the flow-field. The Ohm's Law expression for current density in partially ionized gases can be written in generalized form as¹²

$$\mathbf{j} = \sigma \left\{ \mathbf{E} + \frac{\nabla p_e}{en_e} - \frac{\mathbf{j} \times \mathbf{B}}{en_e} - \frac{f^2 \tau_{ln}}{m_I n_e} [(2 - \alpha) p_e \times \mathbf{B} + \mathbf{B} \times (\mathbf{j} \times \mathbf{B})] \right\} \quad (2)$$

and

$$\nabla \cdot \mathbf{j} = 0 \quad (3)$$

where the first term accounts for the electric field, the second term accounts for electron pressure gradients, the third term is the Hall effect, and the last term is ion current. Since the plasma is electrically neutral and $\mathbf{B} \approx 0$, $\mathbf{E} = -\nabla V$ and the last two terms may be neglected. In Refs. 1, 4, and 8, the electron pressure gradient term is also neglected, and the expression for current density is

$$\mathbf{j} = -\sigma \nabla V \quad (4)$$

Here we present results using Eq. (2) to include the electron pressure term. Thus,

$$\mathbf{j} = \sigma \left(-\nabla V + \frac{\nabla p_e}{en_e} \right) = \sigma (\mathbf{E} + \mathbf{E}^*) \quad (5)$$

where

$$\mathbf{E}^* \equiv \frac{\nabla p_e}{en_e} \quad (6)$$

Numerical instabilities can be encountered in the incorporation of the electron pressure gradient term, caused by the enormous electron pressure gradient in the cathode tip region. To obtain a stable solution, the electron pressure term has to be rewritten in the form:

$$\frac{\nabla p_e}{en_e} = \frac{\nabla(n_e k_b T_e)}{en_e} = \frac{k_b T_e}{e} \nabla \ln n_e + \frac{k_b}{e} \nabla T_e \quad (7)$$

Note that the gradient of $\ln(n_e)$ is much less severe than that of p_e . This stabilized the code.

The axial electric fields E and E^* are shown in Fig. 11. The electric field E^* induced by the electron pressure gradient is very strong at the cathode tip, and has the opposite sign of the electric field E . E^* rapidly decreases to less than E in magnitude one node into the constrictor, at $x \approx 6$ mm. Downstream of $x \approx 6$ mm, both E and E^* are small.

The predicted electron number density distribution (as well as the electron and heavy species temperature distributions) changes only slightly when Eq. (5), instead of Eq. (4), is used. The predicted plasma voltage decreases from 74 to 71 volts when the electron pressure gradient is included in Ohm's Law. Overall, the electron pressure gradient term did not significantly affect the current distribution, and could be neglected if approximate results were desired.

Inelastic Electron-Molecule Collisions

The assumption of thermal nonequilibrium requires independent energy equations for the electrons and heavy species (molecules, atoms, and ions). In the MKB model the electron energy is separated from the total energy, allowing for a distinct electron temperature T_e . The electron kinetic energy is negligible, so that energy conservation is written as:

$$\nabla \cdot \left[C_{pe} T_e \left(n_e \mathbf{v} - \frac{\mathbf{j}}{e} \right) \right] = \nabla \cdot (\lambda_e \nabla T_e) + \nabla \cdot \left(\frac{1}{m_e} \rho C_{pe} T_e D_e \nabla y_e \right) + \frac{\mathbf{j} \cdot \mathbf{j}}{\sigma} - \text{elst} - \text{radiation} - \sum L_e \quad (8)$$

where L_e is the individual energy loss rate.¹ Here, the electric current density $\mathbf{j} = \sigma(\mathbf{E} + \mathbf{E}^*)$ is assumed to be primarily due to the electrons, so that the convection of the electrons due to the mean flow velocity \mathbf{v} is reduced by the drift flux of electrons \mathbf{j}/e . The convection of electron

energy is balanced by thermal conduction, energy transport due to diffusion, and ohmic heating. Additionally, the electrons lose energy through elastic and inelastic collisions with molecules, atoms, and ions,¹³ and through optically thin radiation loss due to continuum bremsstrahlung.¹⁴ The energy loss due to elastic transfer is:

$$elst = 3k_b(T_e - T_g)n_e m_e \sum_{i \neq e} \frac{\bar{v}_{ei}}{m_i} \quad (9)$$

where the average collision frequencies \bar{v}_{ei} between electrons and heavy species i are calculated using the mean electron thermal speed, heavy species number density n_i , and collision cross section Q_{ei} as¹⁴

$$\bar{v}_{ei} = \sqrt{\frac{8k_b T_e}{\pi m_e}} n_i Q_{ei}. \quad (10)$$

In this research the ionization and recombination processes for H and N are included in the finite-rate chemistry model; thus these inelastic losses are accounted for in the $\sum L_e$ term in Eq. (8). To account for electron energy losses to molecular vibration, rotation, electronic excitation, and ionization modes during the electron-molecule inelastic collision, the electron energy loss during the collision is modeled as δ times the elastic loss:

$$\text{electron energy loss during an electron-molecule inelastic collision} = elst + \sum_i L_e \equiv \delta_i \cdot elst, \quad (11)$$

where the expression for $elst$ is given in Eq. (9), and the subscript i denotes either H₂ or N₂. This is necessary because the molecular excited states are not treated as separate species in the finite rate chemistry model. Although δ_{H_2} and δ_{N_2} are generally energy dependent, $\delta_{H_2} = \delta_{N_2} = 3000$ was chosen for the majority of the simulations in Refs. 1, 4, and 8. Note that Martinez-Sanchez and Miller re-examined δ_{N_2} , and found values as high as $\delta_{N_2} = 4000$, as per Ref. 15.

Parametric studies⁸ showed that the current attached to the constrictor region and the predicted plasma voltage drop was only 40 volts at 10 A when δ from Ref. 12, on the order of 10 to 100, was used. Increasing δ moved the arc attachment location downstream of the constrictor, in agreement with measurements of the current distribution using segmented anodes¹⁶ and anode probe measurements⁶. The values of $\delta_{N_2} = \delta_{H_2} = 3000$ were chosen for the majority of the

simulations because reasonable convective effects were noted, as the arc was swept farther downstream for increasing mass flow rate, and better agreement was achieved between the predicted and experimentally observed operating voltage of 115 volts for the hydrazine CNE simulation (cases 2 and 10, Table 1).

The motivation for the present analysis stems from the potential uncertainties in δ . These are summarized in Fig. 12, where the loss factors from various sources are plotted as a function of T_e . A software package (MacELENDFIF)¹⁷ is also used to estimate δ_{N_2} and δ_{H_2} .

The ELENDFIF software solves the time-dependent Boltzmann transport equation.¹⁸ The software was used to calculate the electron energy distribution function $f(\epsilon)$ for weakly ionized hydrogen or nitrogen plasmas. The δ factor was extracted from the relative percentages of inelastic and elastic energy losses using the relation

$$\delta = \frac{100}{\% \text{ of elastic energy transfer}} \quad (12)$$

The effective electron temperature was calculated from the mean electron energy. This was necessary because the distributions can be non-Maxwellian.

The δ factor is dependent strongly on the collision partner and the electron temperature, and weakly on the gas temperature. Moreover, in a 1-kW arcjet, the molecule-rich anode region is slightly above the wall temperature, so the gas (molecule) temperature was chosen to be 1000 K for both hydrogen and nitrogen simulations. The δ_{H_2} values were fitted by a sixth-order polynomial, and the δ_{N_2} values by four piecewise polynomials, in order to incorporate δ into the MKB model.

Figure 12 shows δ_{N_2} and δ_{H_2} calculated by ELENDFIF with δ_{N_2} from Refs. 12 and 15 and δ_{H_2} from Ref. 12. The ELENDFIF results indicate $\delta_{N_2} \approx 800$ for T_e above 10,000 K, while the δ_{H_2} are in rough agreement with those from Ref. 12. The results from Ref. 15 indicate a maximum $\delta_{N_2} \approx 4000$ at $T_e \approx 10,000$ K. The δ_{N_2} from Ref. 15 are mostly higher than the results of ELENDFIF. Thus, it appears that for $T_e > 10,000$ K, the appropriate values for δ_{H_2} and δ_{N_2}

may be of order 10 and 800, respectively. The discrepancies among the δ_{N_2} values require further investigation.

The implications of the high degree of inelastic losses may be further appreciated by examining representative calculations for the electron energy distribution functions.¹⁷ Results for N_2 are shown in Fig. 13 for three ratios of the applied electric field E to the total particle number density N . For respective values of $E/N = 5, 50,$ and 100 Td (1 Townsend (Td) = 1×10^{-17} V-cm²), the 'effective' temperatures are $T_e = 2\varepsilon_{ave}/3k_b \approx 6960, 9390,$ and 18340 K, respectively. (Note that $E/N \approx 65$ Td for typical near-anode predictions of $E \approx 250$ V/mm, $p \approx 1$ atm and $T_g \approx 1000$ K.) The Maxwellian-distribution function:

$$f(\varepsilon) = \frac{2}{\sqrt{\pi}(k_b T_e)^{3/2}} \exp\left(\frac{-\varepsilon}{k_b T_e}\right) \quad (13)$$

appears as a straight line with a slope inversely proportional to T_e in Fig. 13. The distributions are clearly non-Maxwellian. The inelastic losses into the vibration and rotation modes of N_2 reduce significantly the number of electrons at the higher translation energies, and lead to an overpopulation at the lower energies. Because, as appears likely, distributions similar to those indicated in Fig. 13 occur in the arcjet plasma, then the electron-impact ionization and dissociation chemical rate coefficients used in the present model may incur substantial errors. The cross sections and the rate coefficients are energy-averaged over a Maxwellian-distribution function, and thus will introduce similar errors in the electrical conductivity.

Figure 14 indicates that the electron number density along the centerline is similar for both the variable δ and $\delta_{H_2} = \delta_{N_2} = 3000$ cases. The electron number density at the anode wall is much higher for the variable δ case compared to $\delta_{H_2} = \delta_{N_2} = 3000$ case, causing the plasma voltage to drop from 71 volts ($\delta_{H_2} = \delta_{N_2} = 3000$) to 50 volts (variable δ).

When assuming an artificially larger $\delta_{H_2} = \delta_{N_2} = 3000$, the energy transfer from the electrons to the heavy species is increased. Hence, the thermal diffusivity of the electrons is lowered. This low thermal diffusivity enables the electrons to flow downstream rather than to diffuse radially to the anode. When the variable (smaller) δ factors from ELENDIF are used, the

thermal diffusivity of the electrons increases. This results in an increased anode electron temperature upstream, as shown in Fig. 15. As a result, the electrons diffuse to the anode wall in a more upstream location, and this, coupled with higher σ , causes the plasma voltage to decrease by 21 volts.

Additional effects of the electron-molecule inelastic loss δ factor are investigated by comparing the predictions summarized as cases 3, 4, and 5 in Table 1. For the NASA-Lewis arcjet geometry, the current is constant at $I = 10$ A, while the mass flow rate is approximately 50 mg/s. Simulations were performed using $\delta_{H_2} = \delta_{N_2} = 3000, 300$, and 30. The results indicate that the anode attachment location, hence the total voltage, are strongly dependent on the δ factor. With $\delta_{H_2} \approx 10$ and δ_{N_2} increased from 800 to 4000, the total arcjet voltage increases from 88 to 101 volts (cases 6, 7 and 8, Table 1) which is still 14 volts lower than the experimentally observed⁷ 115 volts. Hence, uncertainties in δ_{N_2} do not produce a large variation in voltage as long as $\delta_{H_2} \approx 10$.

The results in Table 1 indicate that increasing the cathode gap, x_{cat} , increases the total voltage (cases 2, 3, and 4). The reason is that increasing the cathode gap increases the length of the arc, and this causes the plasma resistance to increase. The total voltage then increases to maintain the same current (current = total voltage / plasma resistance). The predicted total voltage and specific impulse from the CNE simulation with $\delta_{H_2} = \delta_{N_2} = 3000$ (cases 2 and 9, Table 1) are within $\pm 5\%$ of the experimental measurements (case 10, Table 1). The predicted efficiencies (cases 2 and 9, Table 1) are 5-6% higher than the experimental value (case 10, Table 1).

Conclusions

A detailed nonequilibrium 1-kW hydrazine arcjet model (the MKB model) has been used successfully to interpret the complicated physics of the arcjet. The model treats thermal and chemical nonequilibrium, which includes finite-rate chemical kinetics and mass diffusion. The model is geometry-flexible, and also includes a thermal model for the anode. These features make

the description sufficiently comprehensive for continuing arcjet analyses and design studies. The MKB model is presently the only 1-kW hydrazine arcjet model that treats two-dimensional flow and thermal and chemical nonequilibrium.

The major conclusions are summarized below:

(1) A nonequilibrium description of the plasma flowfield is required to model the arcjet physics accurately. The thermal nonequilibrium, chemical nonequilibrium (CNE) model reveals a high degree of thermal nonequilibrium near the electrode surfaces. The predicted thermal nonequilibrium near the anode is $T_e/T_g \approx 12$, and is in qualitative agreement with the $T_e/T_g \approx 10 - 20$ from anode probe measurements⁶. The large thermal nonequilibrium is responsible for increased ionization rates. The elevated population of charged species permits the conduction of electric current through near-anode regions of the plasma where T_g is low. The incorporation of a separate energy equation for the electron gas is required to capture this arc conduction mechanism.

The CNE simulations reveal radial ambipolar diffusion as a significant factor. The radial diffusion of charged species also controls the near-anode electron populations. The chemical nonequilibrium predictions indicate a reduced arc length, partially due to radial ambipolar diffusion. The incorporation of finite-rate chemistry also permits a more accurate description of the inelastic energy exchange between the electrons and heavy species.

(2) Finite-rate chemistry models are required to accurately capture the flowfield species distributions. Radial species diffusion is also important. The dissociated H and N atoms diffuse from the hotter central region of the flow to the cooler anode wall. Diffusive transport of the molecular N_2 and H_2 species from the cooler anode radially inward to the hot central flow region is also significant.

(3) The anode arc attachment is strongly dependent on the chosen value for the electron-molecule inelastic collision factor δ . Generally, the arc attaches farther downstream and the plasma voltage increases as δ increases. Large variations in δ_{H_2} and δ_{N_2} (from 300 to 3000)

produce a 7 volt change in the arcjet voltage, similar to that caused by a 76% increase in cathode gap (cases 2, 3, and 4, Table 1).

(4) The predicted global performance and local variables generally follow experimental measurements. The predicted total voltage and specific impulse I_{sp} for hydrazine is within $\pm 5\%$ of measured values (cases 2, 9, and 10, Table 1). The slight under-predictions in voltage and over-predictions in the specific impulse translate to over-predictions in the thrust efficiency of 5-6% higher than the experimental value (cases 2, 9, and 10, Table 1).

The correct prediction for the arc attachment location and operating voltage is of paramount concern for continuing research. As the arcjet community moves to higher specific power designs, the anode current density distribution will ultimately determine the severity of the anode thermal loading, and therefore the long term reliability of the thruster.

Acknowledgments

This work was funded by AFOSR under contract F49620-95-1-0363. Dr. Mitat Birkan is the program manager. The authors wish to acknowledge helpful discussions with Ph.D. candidate N. Tiliakos. We also thank Prof. Mark Kushner (Department of Electrical and Computer Engineering, University of Illinois at Urbana-Champaign) for helpful advice in modeling inelastic energy processes in weakly ionized gases.

References

- ¹Megli, T. W., Krier, H. and Burton, R. L., "Plasmadynamics Model for Nonequilibrium Processes in N_2/H_2 Arcjets," *Journal of Thermophysics and Heat Transfer*, Vol. 10, No. 4, 1996, pp. 554-562.
- ²Miller, S. A., and Martinez-Sanchez, M., "Two-Fluid Nonequilibrium Simulation of Hydrogen Arcjet Thrusters," *Journal of Propulsion and Power*, Vol. 12, No. 1, 1996, pp. 112-119.
- ³Fujita, K., "Performance Computation of a Low-Power Hydrogen Arcjet," AIAA Paper 96-3183, July 1996.
- ⁴Megli, T. W., Krier, H., Burton, R. L., and Mertogul, A., "Two-Temperature Modeling of Nitrogen/Hydrogen Arcjets," *Journal of Propulsion and Power*, Vol. 12, No. 6, 1996, pp. 1062-1069.
- ⁵Lu, J., Krier, H., Burton, R. L., and Goodfellow, K. D., "Collisionless Cathode Sheath Models to Predict Power Distribution in 1 kW Hydrazine Arcjet Thrusters," AIAA Paper 97-3206, July, 1997; in review, *Journal of Thermophysics and Heat Transfer*.
- ⁶Tiliakos, N. T., Burton, R. L., and Krier, H., "Arcjet Anode Plasma Measurements Using Electrostatic Probes," AIAA Paper 97-3201, July 1997; to appear in *Journal of Propulsion and Power*.
- ⁷Curran, F. M., and Haag, T. W., "Extended Life and Performance Test of a Low-Power Arcjet," *Journal of Spacecraft and Rockets*, Vol. 29, No. 4, 1992, pp. 444-452.
- ⁸Megli, T. W., "A Nonequilibrium Plasmadynamics Model for Nitrogen/Hydrogen Arcjets," Ph.D. thesis, Department of Mechanical and Industrial Engineering, University of Illinois, Urbana, IL, 1995.
- ⁹Zube, D. M., and Myers, R. M., "Thermal Nonequilibrium in a Low-Power Arcjet Nozzle," *Journal of Propulsion and Power*, Vol. 9, No. 4, 1993, pp. 545-552.
- ¹⁰Bose, T. K., "Thermophysical and Transport Properties of Multi-Component Gas Plasmas at Multiple Temperatures," *Progress in Aerospace Sciences*, Vol. 25, No. 1, 1988, pp. 1-42.

- ¹¹Richley, E., and Tuma D. T., "On the Determination of Particle Concentrations in Multitemperature Plasmas," *Journal of Applied Physics*, Vol. 53, No. 12, 1982, pp. 8537-8542.
- ¹²Sutton, G. W., and Sherman, A., *Engineering Magneto-Hydrodynamics*, McGraw-Hill, New York, 1965, pp. 148-190.
- ¹³Kruger, C. H., and Mitchner, M., "Kinetic Theory of Two Temperature Plasmas," *Physics of Fluids*, Vol. 10, No. 9, 1967, pp. 1953-1961.
- ¹⁴Mertogul, A. E., "Modeling and Experimental Measurements of Laser Sustained Plasmas," Ph.D. Thesis, Department of Mechanical and Industrial Engineering, University of Illinois at Urbana-Champaign, 1993.
- ¹⁵Martinez-Sanchez, M., and Miller, S. A., "Arcjet Modeling: Status and Prospects," *Journal of Propulsion and Power*, Vol. 12, No. 6, 1996, pp. 1035-1043.
- ¹⁶Curran, F. M., Manzella, D. H., and Pencil, E. J., "Performance Characterization of a Segmented Anode Arcjet Thruster," AIAA Paper, 90-2582, June, 1990.
- ¹⁷Morgan, W. L., and Penetrante, B. M., MacELENDIF version 1.1, Kinema Software, 1994.
- ¹⁸Morgan, W. L., and Penetrante, B. M., "ELENDIF: A Time-Dependent Boltzmann Solver for Partially Ionized Plasmas," *Computer Physics Communications*, Vol. 58, No. 1 & 2, 1990, pp. 127-152.

Table 1 Summary of predictions for 1-kW hydrazine (N_2H_4) arcjets operating at 10 A and approximately 50 mg/s. The geometry is the NASA-Lewis Arcjet.⁷ Note that x_{cat} is the cathode gap spacing measured axially from the cathode surface to the converging portion of the anode surface. The total voltage predictions include a cathode sheath voltage of 30 volts (Ref. 5) and an anode sheath voltage of 11 volts (Ref. 6). The experimental values are from Ref. 7.

case	∇p_e term	δ_{N_2}	δ_{H_2}	x_{cat} (mm)	total voltage (volts)	I_{sp} (sec)	η (%)
1*	N	3000	3000	0.58	141	440	33
2	N	3000	3000	0.58	115	439	40
3	N	3000	3000	1.02	122	446	39
4	N	300	300	1.02	115	440	40
5	N	30	30	1.02	104	423	41
6	Y	variable	variable	0.58	88	402	44
7	Y	3000	10	0.58	99	414	42
8	Y	4000	10	0.58	101	416	41
9	Y	3000	3000	0.58	112	436	41
10 (experimental)	--	--	--	0.58	115	419	35

*This is the only CE case.

Figure Captions

Fig. 1 A typical electrothermal arcjet thruster. A voltage difference between the cathode and anode produces an electric discharge which heats the propellant. The thermal energy is converted to kinetic energy as the propellant expands to high velocities in the converging-diverging nozzle.

Fig. 2 Current density at the anode surface for simulated hydrazine. Results are shown for both chemical equilibrium (CE) and chemical nonequilibrium (CNE) simulations. These predictions are for cases 1 and 2 of Table 1; NASA-Lewis geometry.

Fig. 3 Electron temperature at the anode surface for simulated hydrazine. Results are shown for both chemical equilibrium (CE) and chemical nonequilibrium (CNE) simulations. These predictions are for cases 1 and 2 of Table 1; NASA-Lewis geometry.

Fig. 4 Radial distributions of electron number density, electron temperature, and heavy species temperature at the exit plane for the hydrazine chemical equilibrium (CE) case 1 of Table 1; NASA-Lewis geometry.

Fig. 5 Radial distributions of electron number density, electron temperature, and heavy species temperature at the exit plane for the hydrazine chemical nonequilibrium (CNE) case 2 of Table 1; NASA-Lewis geometry.

Fig. 6 Radial distributions of hydrogen H- and nitrogen N-atom mole fractions at the exit plane for the hydrazine chemical equilibrium (CE) and chemical nonequilibrium (CNE) simulations. These predictions are for cases 1 and 2 of Table 1; NASA-Lewis geometry.

Fig. 7 Radial distributions of hydrogen H₂- and nitrogen N₂-molecule mole fractions at the exit plane for the hydrazine chemical equilibrium (CE) and chemical nonequilibrium (CNE) simulations. These predictions are for cases 1 and 2 of Table 1; NASA-Lewis geometry.

Fig. 8 Voltage contours for the NASA-Lewis arcjet; simulated hydrazine, chemical nonequilibrium (CNE) simulation, $I = 10$ A, $\dot{m} \approx 50$ mg/s (case 2) of Table 1.

Fig. 9 Ohmic heating contours for the NASA-Lewis arcjet; simulated hydrazine, chemical nonequilibrium (CNE) simulation, $I = 10$ A, $\dot{m} \approx 50$ mg/s (case 2) of Table 1.

Fig. 10 Ionization fraction contours for the NASA-Lewis arcjet; simulated hydrazine, chemical nonequilibrium (CNE) simulation, $I = 10$ A, $\dot{m} \approx 50$ mg/s (case 2) of Table 1.

Fig. 11 Electric field E and E^* induced by electron pressure gradient along the centerline with $\delta_{N_2} = \delta_{H_2} = 3000$ and Eq. (5). Note that the constrictor is 0.25 mm long, and is located between $x = 5.92$ mm and $x = 6.17$ mm.

Fig. 12 Electron-molecule inelastic loss delta factor δ from various sources.

Fig. 13 Calculated electron energy distribution function, f , for various ratios of the electric field to the total number density E/N for a nitrogen plasma.¹⁷ The Maxwellian distribution function is a straight line.

Fig. 14 Electron number density at the centerline and the anode for $\delta_{N_2} = \delta_{H_2} = 3000$ and variable δ_{N_2} and δ_{H_2} from Ref. 17.

Fig. 15 Electron and heavy species temperature along the anode for $\delta_{N_2} = \delta_{H_2} = 3000$ and variable δ_{N_2} and δ_{H_2} from Ref. 17.

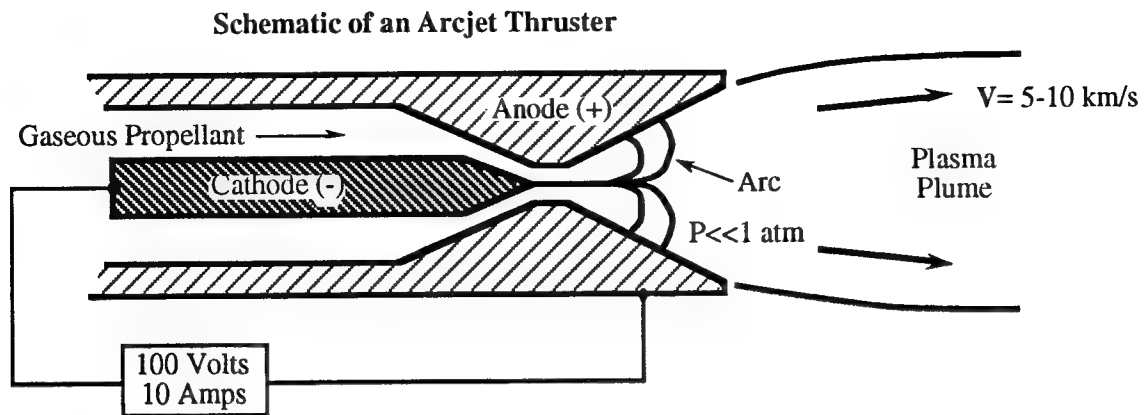


Fig. 1 A typical electrothermal arcjet thruster. A voltage difference between the cathode and anode produces an electric discharge which heats the propellant. The thermal energy is converted to kinetic energy as the propellant expands to high velocities in the converging-diverging nozzle.

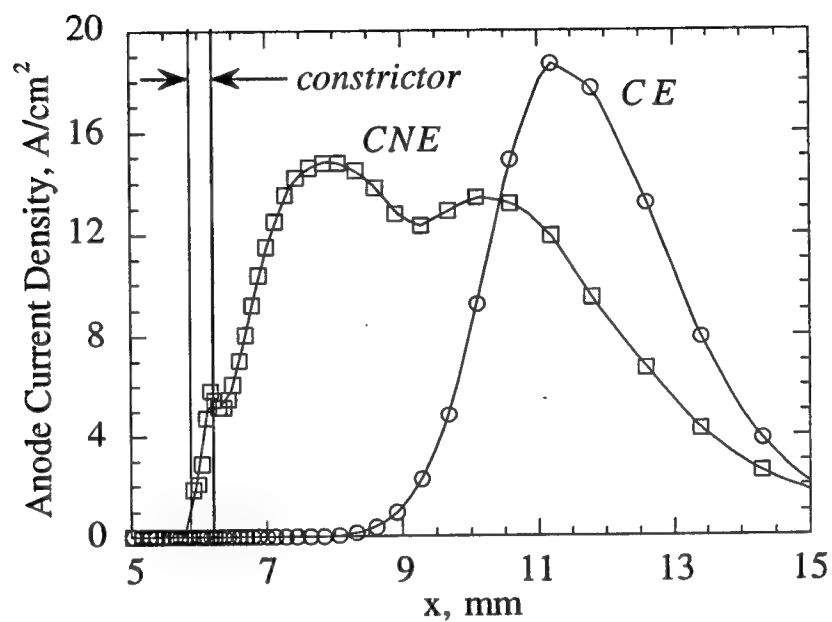


Fig. 2 Current density at the anode surface for simulated hydrazine. Results are shown for both chemical equilibrium (CE) and chemical nonequilibrium (CNE) simulations. These predictions are for cases 1 and 2 of Table 1; NASA-Lewis geometry.

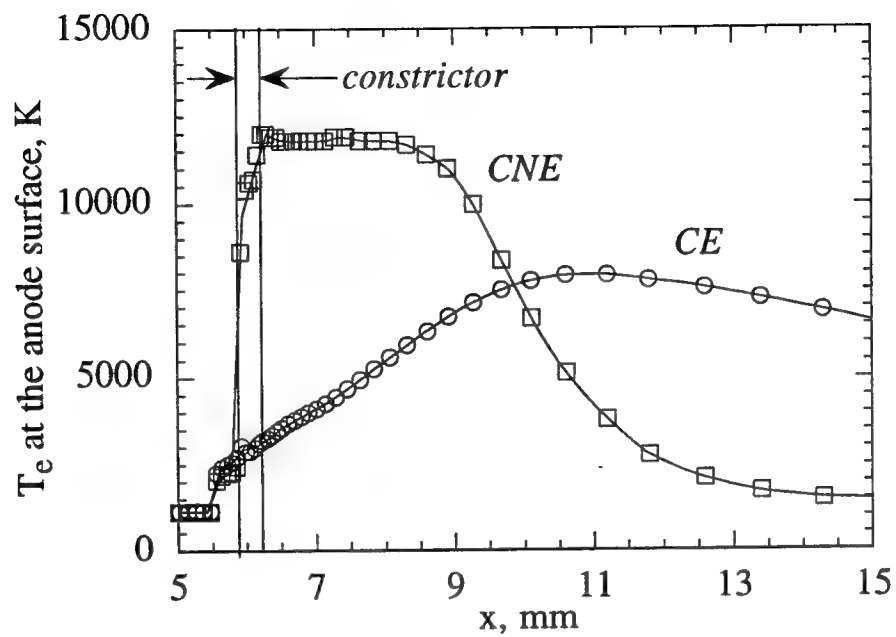


Fig. 3 Electron temperature at the anode surface for simulated hydrazine. Results are shown for both chemical equilibrium (CE) and chemical nonequilibrium (CNE) simulations. These predictions are for cases 1 and 2 of Table 1; NASA-Lewis geometry.

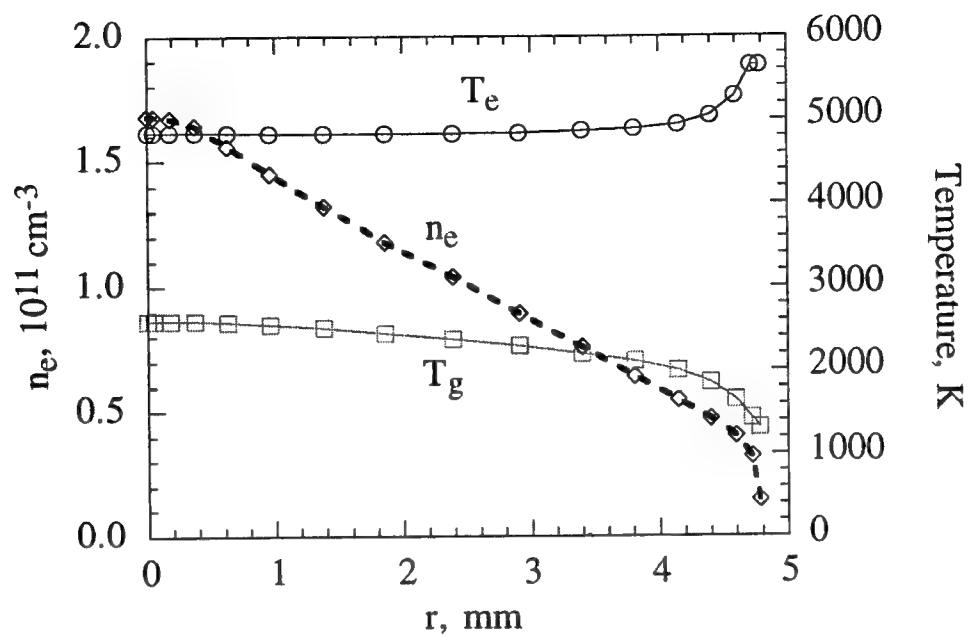


Fig. 4 Radial distributions of electron number density, electron temperature, and heavy species temperature at the exit plane for the hydrazine chemical equilibrium (CE) case 1 of Table 1; NASA-Lewis geometry.

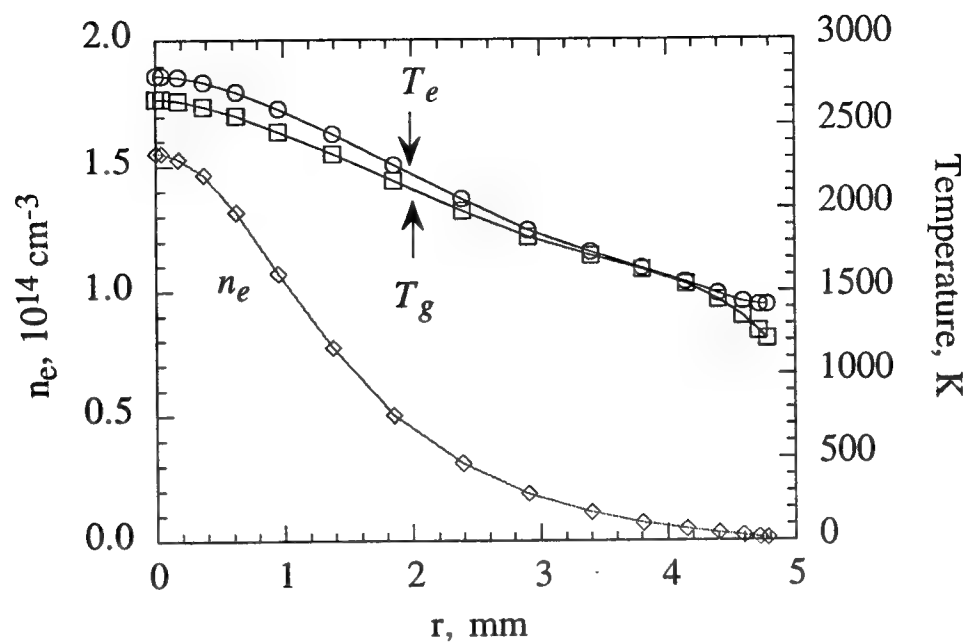


Fig. 5 Radial distributions of electron number density, electron temperature, and heavy species temperature at the exit plane for the hydrazine chemical nonequilibrium (CNE) case 2 of Table 1; NASA-Lewis geometry.

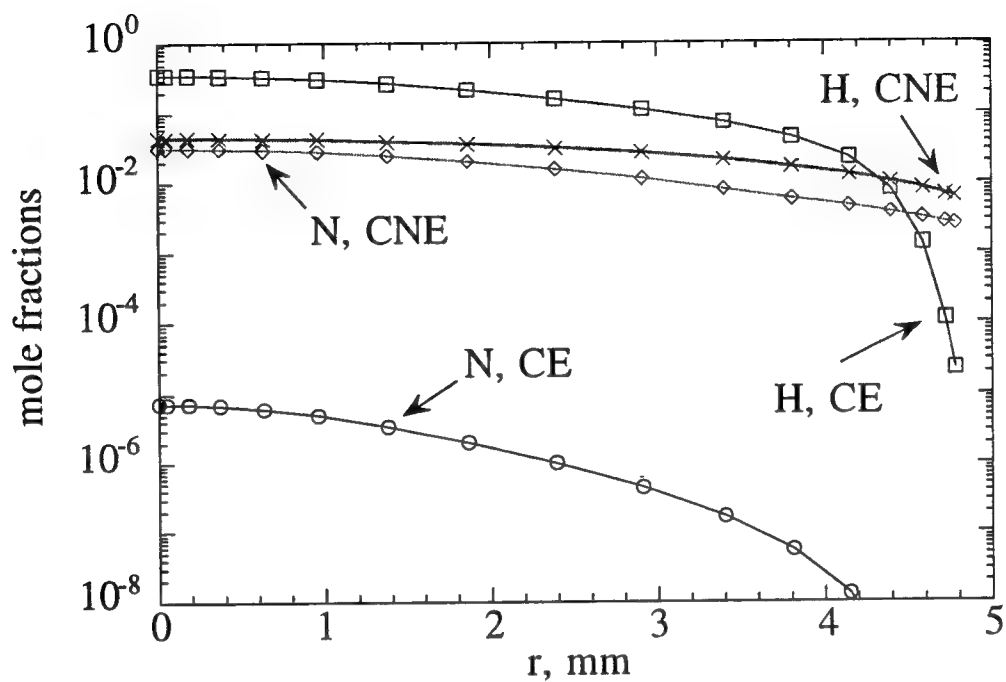


Fig. 6 Radial distributions of hydrogen H- and nitrogen N-atom mole fractions at the exit plane for the hydrazine chemical equilibrium (CE) and chemical nonequilibrium (CNE) simulations. These predictions are for cases 1 and 2 of Table 1; NASA-Lewis geometry.

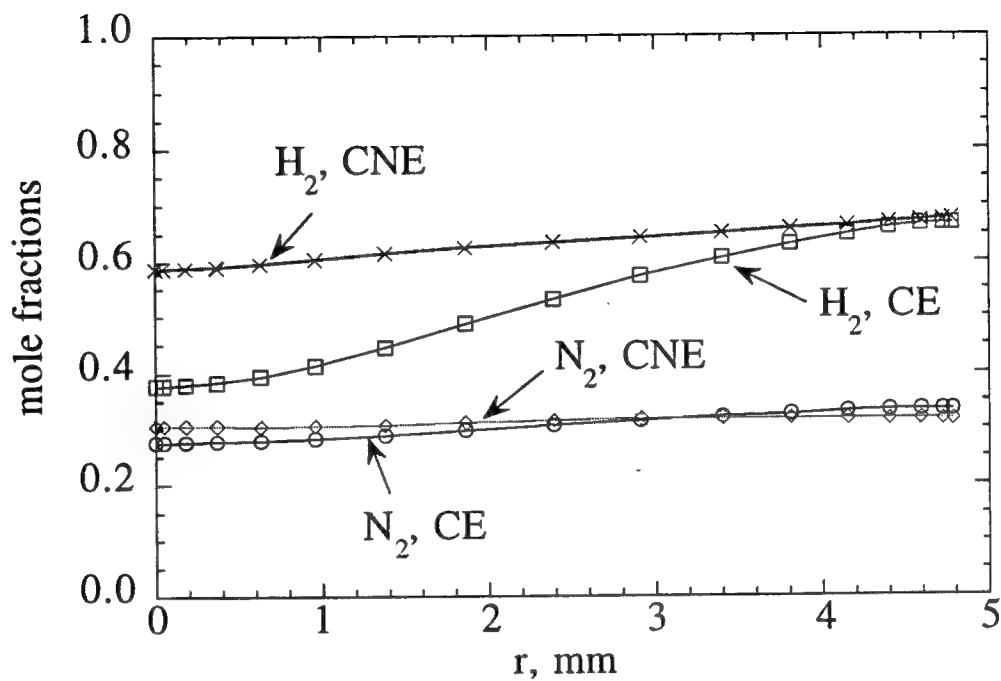


Fig. 7 Radial distributions of hydrogen H₂- and nitrogen N₂-molecule mole fractions at the exit plane for the hydrazine chemical equilibrium (CE) and chemical nonequilibrium (CNE) simulations. These predictions are for cases 1 and 2 of Table 1; NASA-Lewis geometry.

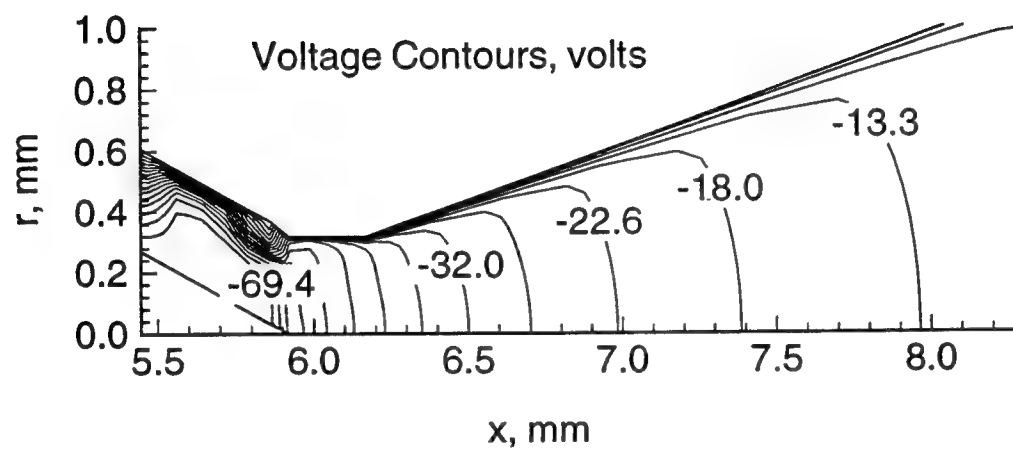


Fig. 8 Voltage contours for the NASA-Lewis arcjet; simulated hydrazine, chemical nonequilibrium (CNE) simulation, $I = 10$ A, $\dot{m} \approx 50$ mg/s (case 2) of Table 1.

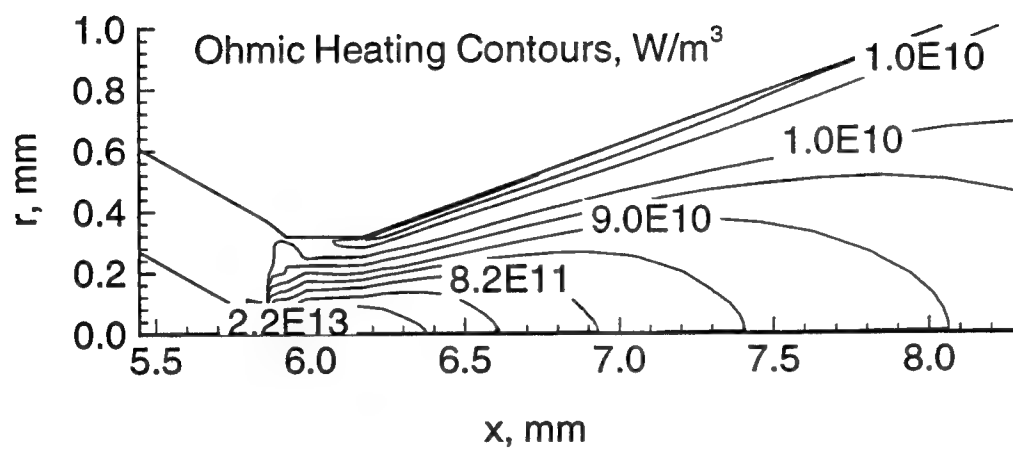


Fig. 9 Ohmic heating contours for the NASA-Lewis arcjet; simulated hydrazine, chemical nonequilibrium (CNE) simulation, $I = 10$ A, $\dot{m} \approx 50$ mg/s (case 2) of Table 1.

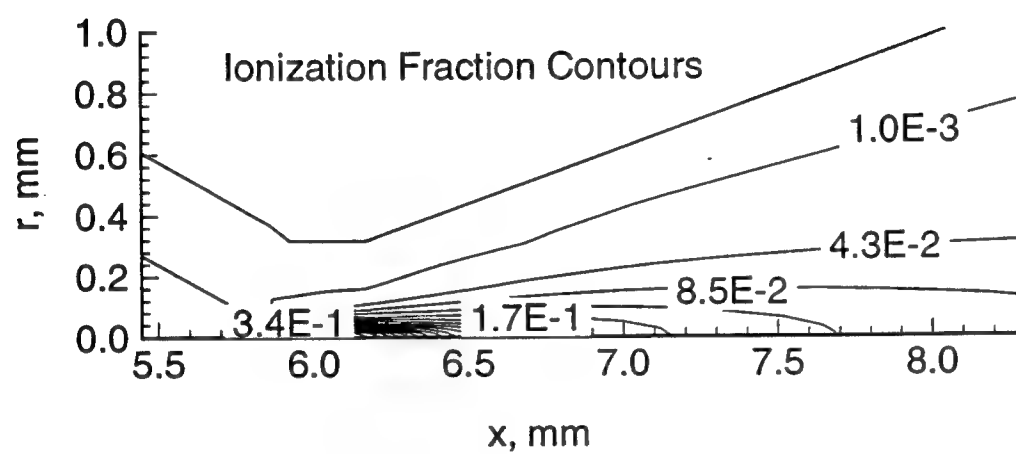


Fig. 10 Ionization fraction contours for the NASA-Lewis arcjet; simulated hydrazine, chemical nonequilibrium (CNE) simulation, $I = 10$ A, $\dot{m} \approx 50$ mg/s (case 2) of Table 1.

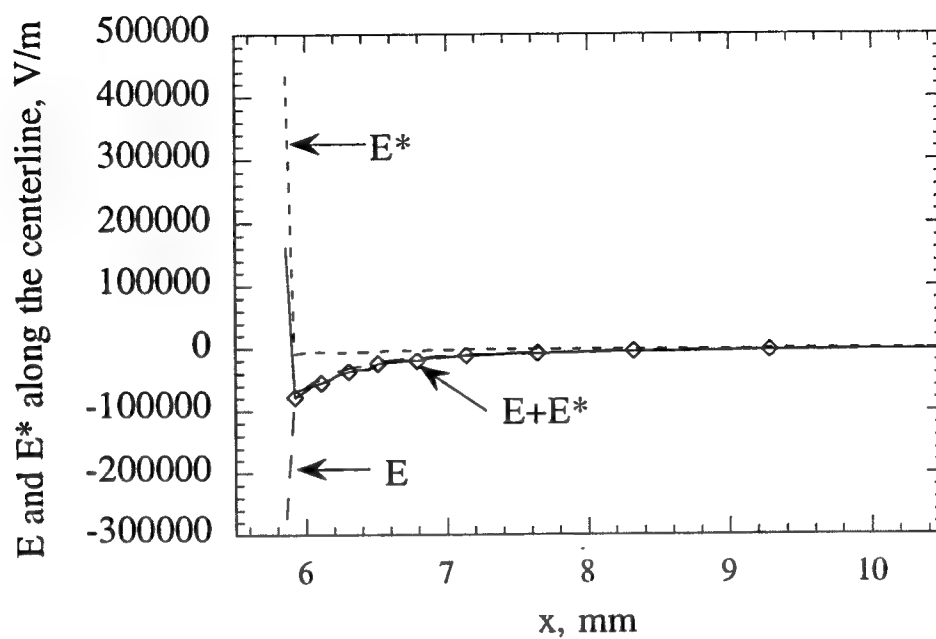


Fig. 11 Electric field E and E^* induced by the electron pressure gradient along the centerline with $\delta_{N2} = \delta_{H2} = 3000$ and Eq. (5). Note that the constrictor is 0.25 mm long, and is located between $x = 5.92$ mm and $x = 6.17$ mm.

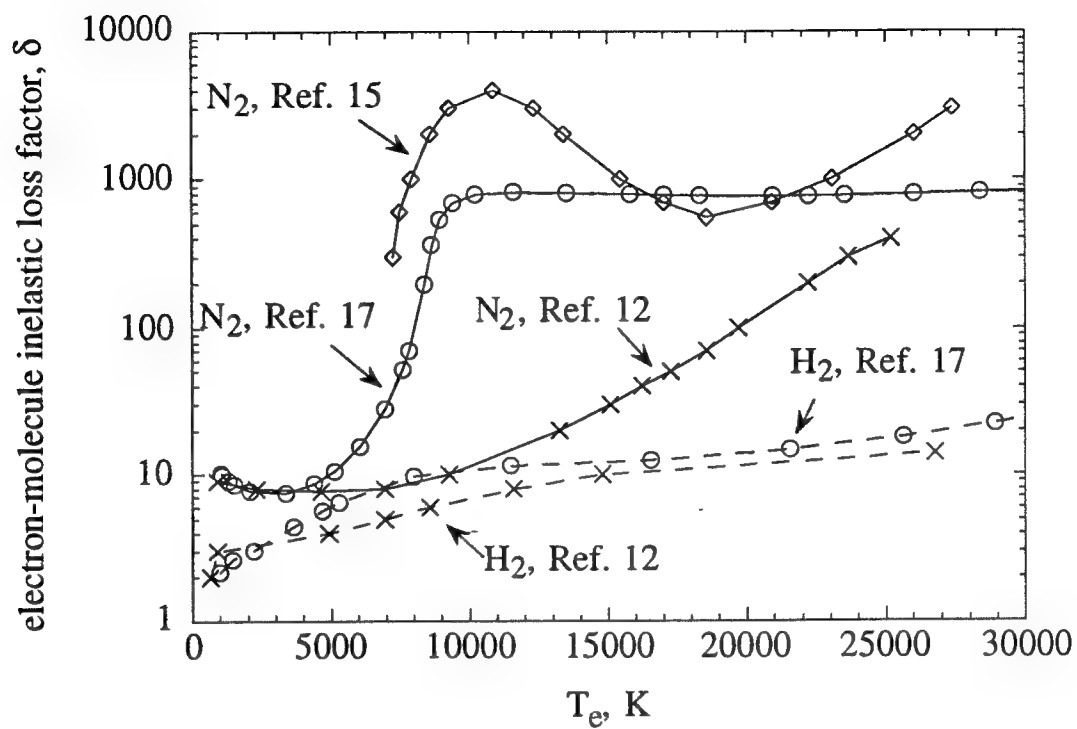


Fig. 12 Electron-molecule inelastic loss factor δ from various sources.

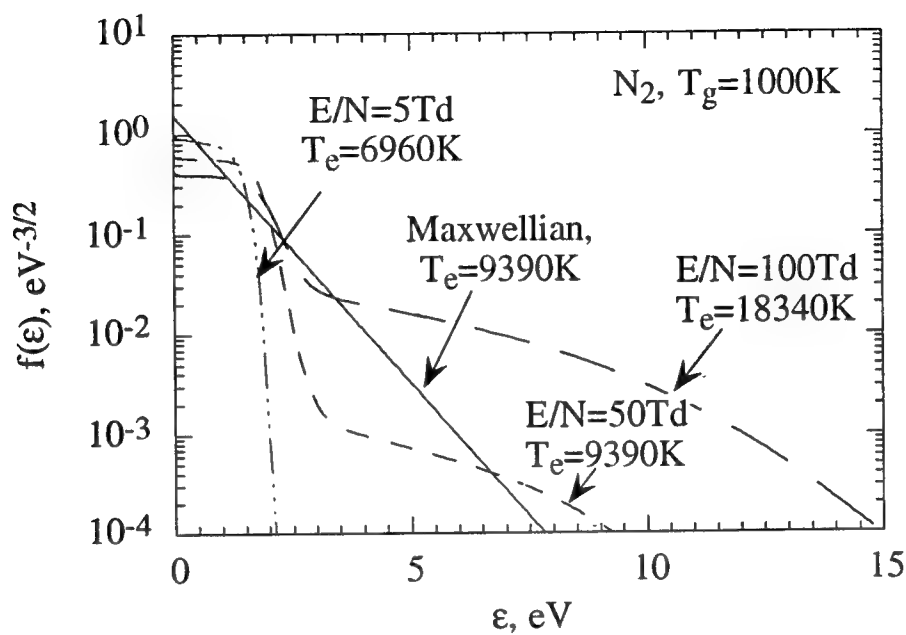


Fig. 13 Calculated electron energy distribution function, f , for various ratios of the electric field to the total number density E/N for a nitrogen plasma.¹⁷ The Maxwellian distribution function is a straight line.

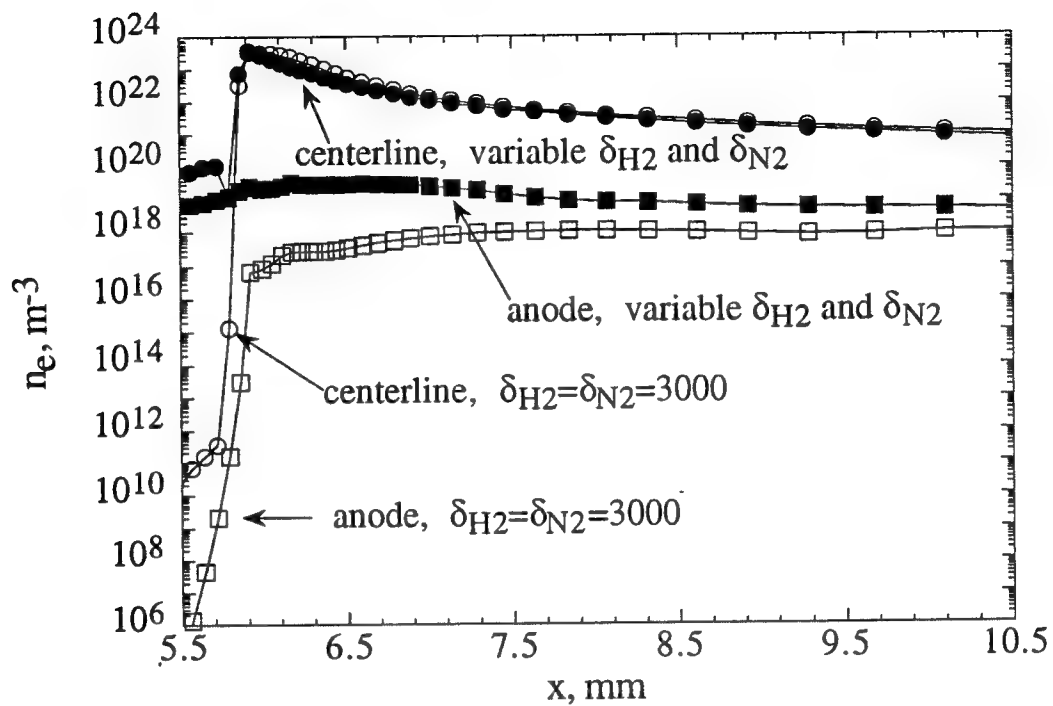


Fig. 14 Electron number density at the centerline and the anode for $\delta_{N_2} = \delta_{H_2} = 3000$ and variable δ_{N_2} and δ_{H_2} from Ref. 17.

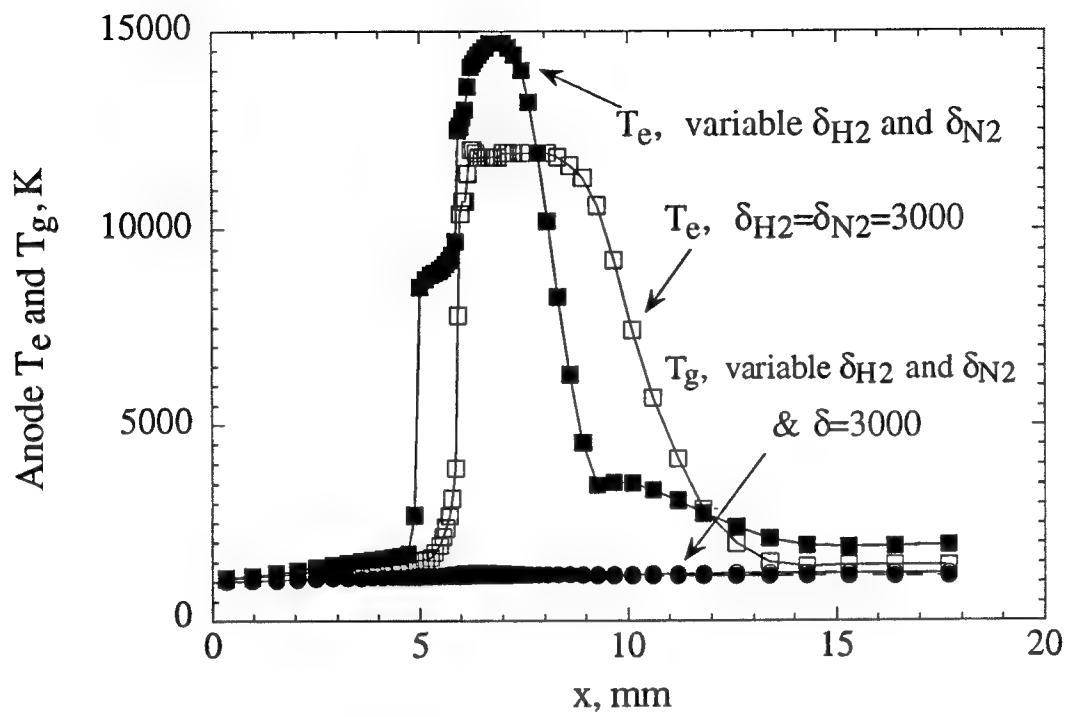


Fig. 15 Electron and heavy species temperature along the anode for $\delta_{N2} = \delta_{H2} = 3000$ and variable δ_{N2} and δ_{H2} from Ref. 17.

Collisionless Cathode Sheath Models to Predict Power Distribution in 1 kW Hydrazine Arcjets

Junqing Lu,^{*} Herman Krier,^{**} and Rodney L. Burton[†]
University of Illinois at Urbana-Champaign, Urbana, IL 61801

and

Keith D. Goodfellow^{††}
Jet Propulsion Laboratory/California Institute of Technology, Pasadena, CA 91109

Abstract

This paper presents two different approaches to predict the cathode sheath potential necessary to account for the total voltage in a 1 kW hydrazine arcjet operating at 10 A. The first approach is a modification of the sheath model first developed by K. Fujita, and the second approach is the cathode sheath model developed by K. D. Goodfellow. The Fujita cathode sheath model is modified here to calculate the cathode sheath potential, electron temperature and number density at the cathode sheath edge of a 1 kW hydrazine arcjet, using near-cathode bulk plasma properties from a nonequilibrium numerical model developed by Megli, Krier, and Burton. The sheath potential is sensitive to current attachment area, cathode tip temperature, and the properties of the near-cathode bulk plasma. For a 1 kW hydrazine arcjet operating at 10 A and 50 mg/s, the sheath potential from the modified Fujita model is approximately -30 volts for a pure tungsten cathode with $2 \times 10^{-8} \text{ m}^2$ attachment area, and 3680 K cathode tip temperature. The Goodfellow model consists of a near-cathode plasma model and a thermal model of the cathode. The plasma model contains models for the surface, sheath, presheath and ionization regions. The input parameters for the combined model are the total pressure, the arcjet current, and one of the following: cathode temperature, sheath voltage, or attachment area/current density. The cathode temperature is the best understood of these three parameters and is used here. Comparisons between the two cathode models have shown good agreement for the determinations of the sheath voltage, electron temperature and the electron number density. However, a factor of 10 or more is calculated for the electric field at the cathode surface.

Nomenclature

area	cathode area that emits current, m^2
A	Richardson constant for thermionic emission, $A/m^2 \cdot K^2$
d	sheath thickness, m or nm
D_A	ambipolar diffusion coefficient, m^2/s
e	electric charge unit, C
E	electric field, V/m
E_{bo}	normalized thermionic electron thermal energy
H_f	heat of fusion for tungsten, kJ/kg
I	arcjet current, A
j_{Ad}	ambipolar diffusion current density at the sheath edge, A/m^2
J_b	normalized thermionic current density
j_d	net current density at the sheath edge, A/m^2
j_{ed}	electron current density at the sheath edge, A/m^2
j_{em}	electron current density due to cathode emission, A/m^2
j_{id}	ion current density at the sheath edge, A/m^2
j_{th}	current density due to electron thermal diffusion toward the cathode, A/m^2
k_b	Boltzmann constant, J/K
L	boundary layer thickness, m
m_e	electron mass, kg
m_i	ion mass, kg
n_d	ion or electron number density at the sheath edge, m^{-3}
n_e	electron number density, m^{-3}
r	radial coordinate
T_C	cathode tip temperature, K

T_{ed}	electron temperature at the sheath edge, K
δ	electron-molecule inelastic collision factor \equiv total energy transfer/elastic energy transfer
ϵ_c	normalized electric field at cathode surface
ϵ_i	effective ionization potential of hydrazine propellant, volts
η_c	normalized sheath voltage
λ_D	Debye length, m or nm
λ	mean free path, m
ϕ_o	sheath potential difference, volts
ϕ_E	reduction in cathode work function due to Schottky effect, volts
ϕ_w	work function of the cathode material, volts
$\phi_{w\text{eff}}$	effective cathode work function, volts

Part A. Modified Fujita Cathode Sheath Model

Introduction

Electrothermal arcjets offer significant propellant savings over chemical satellite propulsion systems, by heating the propellant electrically to achieve better performance. The schematic of a 1 kW arcjet is shown in Fig. 1. A new interpretation of the hydrazine arcjet has been achieved by a numerical model developed by Megli, Krier, and Burton (the MKB model), which features two-dimensional, steady and laminar flow, two temperature (electron and heavies), finite rate chemistry, and nitrogen/hydrogen propellant.¹ The model solves a modified set of Navier-Stokes equations with electron and heavy species (molecules, atoms, and ions) energy equations. The electrical current distribution is self-consistently coupled to the plasma flowfield by equations of charge continuity and Ohm's Law. Although the model has produced useful arcjet performance data and agrees reasonably well with the experimental data, appropriate anode and cathode sheath models were not incorporated such that the predicted voltage is only approximately 50-75% of the experimental value, depending on the assumed values of the electron-molecule inelastic collision factor.¹⁻⁶ The purpose of this study is to model the cathode sheath self-consistently with the MKB model to predict cathode sheath potential.

The cathode sheath model described in the first part of this paper is a modification of a model first developed by Fujita, who incorporated a one dimensional cathode sheath model for a low power hydrogen arcjet.⁷ Unlike most sheath models, the Fujita sheath model solves for the cathode sheath potential and plasma properties (electron temperature, electron or ion number density) at the sheath edge rather than resolving the property distributions in the entire sheath. In the model, the properties at the sheath edge are coupled to the near-cathode bulk fluid properties, yielding a cathode sheath voltage fall from -5 to -30 volts, depending on the conditions near the cathode surface. Here, we have modified the Fujita cathode sheath model and use this one-dimensional collisionless cathode sheath model by coupling in a self-consistent way to the MKB arcjet model¹.

Formulation of the Modified Fujita Sheath Model

The cathode sheath is assumed to be one dimensional. As shown in Fig. 2, the total current density at the sheath edge is given by:

$$j_d = j_{id} + j_{ed} = I / \text{area} \quad (1)$$

Secondary electron emission is neglected in Eq. (1). The secondary electron current density is equal to a constant times the ion current density, where the constant is dependent on the propellant and the cathode material, and typically varies from 0.05 to 0.2. The ion current at the sheath edge is assumed to be equal to the ambipolar diffusion flux from the plasma. The expression for ion current density is:

$$j_{id} = -en_d \sqrt{\frac{k_b T_{ed}}{m_i}} = j_{Ad} \quad (2)$$

The ion velocity is modeled as the Bohm velocity, rather than $\sqrt{2}$ times the Bohm velocity in the Fujita sheath model. The ambipolar diffusion current at the sheath edge is expressed as:

$$j_{Ad} = -e(D_A \frac{\partial n}{\partial r})_d \quad (3)$$

Combining Eqs. (2) and (3), we have

$$n_d \sqrt{\frac{k_b T_{ed}}{m_i}} = (D_A \frac{\partial n}{\partial r})_d \quad (4)$$

The electron current density at the sheath edge consists of two components: the electrons with enough directed thermal energy to go from the bulk plasma to the cathode, and the electrons emitted from the cathode. Hence,

$$j_{ed} = j_{th} + j_{em} \quad (5)$$

Assuming collisionless sheath and Maxwellian electron energy distribution, it follows that

$$j_{th} = en_d \sqrt{\frac{k_b T_{ed}}{2\pi m_e}} \exp\left(\frac{e\phi_o}{k_b T_{ed}}\right), \quad (6)$$

where $\phi_0 < 0$. The Fujita model, which ignores the effect of the electric field at the cathode surface, is modified by describing electron emission from the cathode with the extended Schottky emission equation:⁸

$$j_{em} = -AT_c^2 \exp\left(-\frac{e\phi_{weff}}{k_b T_c}\right) \frac{\pi q}{\sin(\pi q)} \quad (7)$$

where A is the Richardson constant for thermionic emission. The Schottky correction for the lowering of the cathode work function by the electric field is included in the ϕ_{weff} term:⁸

$$\phi_{weff} = \phi_w - \sqrt{\frac{eE_c}{4\pi\epsilon_0}}, \quad (8)$$

where E_c is the cathode surface electric field, and q is the fraction of the electrons escaping by the tunnel effect through the metal surface potential barrier. The term $\pi q/\sin(\pi q)$ accounts for the contribution of the tunneling electrons to the current density of the emitted electrons. For small q , the term $\pi q/\sin(\pi q)$ is equal to 1, and Eq. (7) reduces to the Schottky emission equation. For zero cathode electric field E_c , Eq. (7) reduces to pure thermionic emission. The expression for q is:⁸

$$q = \left(\frac{E_c}{110,000 T_c^{4/3}} \right)^{0.75} \quad (9)$$

where q is dimensionless, E_c is in volts/m, and T_c is in degree Kelvin. The extended Schottky emission mechanism is valid for q less than 1. When the electric field is high enough, the emission mechanism becomes the thermal-field emission, or even pure field emission.

The electric field at the cathode surface needs to be expressed in terms of the sheath potential and the sheath thickness, and the following expression is used:

$$E_c = -\phi_0 / d. \quad (10)$$

The justification for Eq. (10) is discussed below. Substituting the above equations into (1) yields the expression for the total arcjet current density I/area :

$$I/\text{area} = -en_d \sqrt{\frac{k_b T_{ed}}{m_i}} + en_d \sqrt{\frac{k_b T_{ed}}{2\pi m_e}} \exp\left(\frac{e\phi_0}{k_b T_{ed}}\right) - AT_c^2 \exp\left(-\frac{e\phi_{weff}}{k_b T_c}\right) \frac{\pi q}{\sin(\pi q)} \quad (11)$$

The Fujita sheath model obtains an additional equation by using the relationship between the electron temperature at the sheath edge and the fraction of the electrons that are able to reach the cathode. Here, this equation is replaced by the energy flux balance equation. Assuming that electrons and ions are absorbed perfectly by the cathode, and neglecting convective heat transfer and vaporization of the cathode material, then the cathode energy equation is obtained through an energy flux balance:⁹⁻¹²

$$|j_{th}|(\phi_{weff} + \frac{2k_b T_{ed}}{e}) + |j_{id}|(-\phi_o + \varepsilon_i - \phi_{weff} + \frac{2k_b T_c}{e}) - |j_{em}|(\phi_{weff} + \frac{2k_b T_c}{e}) - \varepsilon \sigma T_c^4 = 0 \quad (12)$$

The above simultaneous algebraic equations [Eqs. (4), (11), and (12)] are solved iteratively to determine the sheath potential. First the sheath thickness d is specified as a multiple of the Debye length, and the Debye length is calculated from the initial guesses for ϕ_o , T_{ed} , and n_d . Simultaneous Eqs. (4), (11), and (12) are then solved iteratively for ϕ_o , T_{ed} , and n_d . The equation solver is the Newton-Raphson method with successive under-relaxation. After solutions for one sheath thickness are obtained, the sheath thickness is specified at a different multiple of the Debye length. From the various solutions at different sheath thickness, the solution whose T_{ed} is equal to T_e from the MKB arcjet model is chosen as the sheath solution for the arcjet. Figure 3 shows the electron temperature distribution obtained by the MKB model in the constrictor region of a 1 kW arcjet operating at 10 A, 50 mg/s.¹

A typical sheath thickness, $O(\lambda_D)$, is much smaller than the computational grid spacing. A typical sheath edge and the near-cathode computational grid are shown in Fig. 4. The grid line on the cathode surface is designated by $j = 1$, and the next grid line by $j = 2$. The distance between the radial grid lines j is approximately 3600 nm. A typical sheath thickness is found to be much smaller than 3600 nm, and hence the sheath edge is drawn close to the cathode surface. The computational cell that encloses the current attachment area is also shown.

Input Parameters of the Modified Fujita Sheath Model

The sheath model requires that a number of parameters be specified. These parameters are the current attachment area, the cathode material, and the cathode tip temperature at the attachment area. The choice of these parameters is discussed below.

Current attachment area and corresponding current density

It is generally agreed that current in an arcjet attaches within the cathode spot area. Curran and Haag examined the cathode tip of a 1.2 kW hydrazine arcjet after 1000 hours of operation,¹³ and found that the tip region becomes a crater with a diameter of approximately 0.8 mm. Within the main crater on the tip there is a second, smaller crater with a diameter of approximately 0.16 mm. It was hypothesized that this crater is molten and that arc current attaches in the crater during steady state operation.¹⁴ The 0.16 mm crater corresponds to an attachment area of approximately $2 \times 10^{-8} \text{ m}^2$.

Tiliakos used a microscope to examine the cathode tip region of a 1 kW hydrazine arcjet operated at 10 A for a few hours,⁶ and found a cathode spot diameter of approximately 0.35 mm. Berns et al. conducted on-axis spectral imaging of the cathode region of an arcjet.^{14,15} For a 1.4 kW hydrogen arcjet operating at 9.8 to 10.0 A, the average cathode spot diameter was approximately 0.58 mm.¹⁴ For a 30 kW hydrogen arcjet operating at 146 to 210 A, the cathode spot diameter was approximately 1.0 mm.¹⁵ The arcjets in Refs. 6, 14, and 15 were operated for a few hours.

The magnitude of the total current density is an indication of the emission mode. As noted by Cobine,¹⁶ determination of the cathode current density is subject to considerable uncertainties due to the rapid motion of the cathode spot and the high temperature gradients over the surface of hot cathodes. Based on the above observations, Cobine remarked that both photographs of the cathode spot and measurements of the marks left by the spot would probably indicate too large an area, and therefore too low a current density.¹⁶

Cobine's remarks are partially supported by the experimental work of Berns et al. for a 1 kW hydrogen arcjet.¹⁴ In that study, the average current density based on the cathode spot

diameter inferred from the cathode temperature profile is only about $0.4 \times 10^8 \text{ A/m}^2$, an order of magnitude lower than the peak current density based on the temperature profile. However in a high power hydrogen arcjet, a similar approach by Berns et al.¹⁵ yielded good agreement between the average current density ($\sim 2\text{-}2.67 \times 10^8 \text{ A/m}^2$) based on the cathode spot area and the peak current density ($\sim 4\text{-}5 \times 10^8 \text{ A/m}^2$) based on the temperature profile. The same study also found that the current density profiles are sensitive to mass flow rate and arcjet power. The two studies by Berns et al. suggest that the average current density estimate based on cathode spot area may be a good one for the high power arcjet, but a poor one for the low power arcjet. It is estimated here that cathode spot area based on post-test scanning electron microscope (SEM) photos is close to the spot area based on the cathode temperature profile.

Based on the above discussions, the area of the small crater ($2 \times 10^{-8} \text{ m}^2$) from the Curran and Haag post-test observation is chosen as the attachment area for use in the modified Fujita sheath model. This area corresponds to a current density of $5 \times 10^8 \text{ A/m}^2$. For this attachment area and 10 A current, the induced magnetic field is 0.025 Tesla, which corresponds to a negligible magnetic-field-induced pressure of 0.0025 atm.

At the chosen current density, the electron emission process at the cathode is a mixture of field and thermionic emission, as summarized by Guile.¹⁷ For thermionic emission, the cathode temperature is greater than 3500 K, and the current density is approximately from 10^7 to 10^8 A/m^2 . For field emission, the cathode temperature is less than 3000 K, and the current density is approximately from 10^{10} to 10^{11} A/m^2 . The cathode spot is fixed or slow-moving for thermionic emission, while it moves rapidly over the metal surface for field emission.¹⁷

Somerville¹⁸ classifies arcs with refractory cathodes into burning-spot arcs and burning-spot-free, i.e., thermionic arcs. For relatively low current, the arc contracts strongly into a burning spot at the cathode. For higher current, the arc suddenly attaches at the cathode diffusely and the cathode is burning-spot free. For a burning-spot arc, the current density is of the order of 10^9 A/m^2 or more; for a burning-spot-free arc, the current density is of the order of

10^7 A/m^2 . The chosen current density is therefore between the Guile values for thermionic and the field emission, and the Sommerville values for the burning-spot and the burning-spot-free arc.

Cathode material at the current attachment area

The arcjet cathode is made of 2% thoriated tungsten (W-2% ThO₂). However, an elemental study on arcjet cathode tip composition indicates that the thoria evaporates during the arcjet operation and after a short time the cathode tip is left with pure tungsten.¹⁹ The work functions and Richardson constants for pure tungsten and thoriated tungsten are listed in Table 1, showing significantly lower values for thoriated tungsten.

Table 1 *Work function and Richardson constant for pure and thoriated tungsten.*²⁰

	W	thoriated W
ϕ_w , volts	4.55	2.63
A, $\text{A/m}^2\text{-K}^2$	6.0×10^5	3.0×10^4

Cathode tip temperature

The cathode tip temperature depends strongly on the radiative heat loss, and hence the emissivity of tungsten. Unfortunately, the measured emissivity of tungsten is available in the literature up to 3600 K, below the tungsten melting temperature of 3680 K, and well below the boiling temperature of 5930 K. Hence, at first glance, the temperature of the melted cathode tip could be any value between 3680 and 5930 K.

Berns et al. used a constant emissivity of 0.40 for the cathode tip, and measured gray body intensity to obtain a cathode tip temperature of approximately 4000 K.^{14,15} Goodfellow and Polk used a surface emissivity of about 0.57 for all thermal data measurements, and demonstrated good agreement between the experimental and the modeling results for a 2% thoriated tungsten cathode at a current level of 1000 A and a pressure level of 1.5 to 6.0 kPa.^{21,22} For a pure tungsten cathode under similar conditions,²³ an emissivity of 0.50 yields good agreement between the model prediction and the measured cathode temperature.

For a given radiative power associated with cathode temperature of 4000 K and cathode emissivity of 0.40, the cathode emissivity and the cathode temperature are shown in Fig. 5. The cathode tip temperature is about 3680 K for an emissivity of 0.55, and about 3800 K for an emissivity of 0.50. Goodfellow has calculated, using a cathode thermal model,²³ that a tip temperature of 4000 K causes a melting depth of about 0.1 mm, a layer probably too thick to stay attached under gravity. Hence, the cathode tip temperature is unlikely to be 4000 K and is probably near or slightly above the melting point.

Electron-molecule inelastic collision factor, δ

The sheath is coupled to the bulk plasma through the ambipolar diffusion current. Hence, it is important that the near-cathode bulk plasma properties are accurately modeled. This implies that the current distribution has to be accurately predicted because the plasma properties are coupled to the current distribution within the plasma. It has been shown that the current distribution is strongly coupled to the electron-molecule inelastic collision process.² In Refs. 1 and 2, the total collisional energy loss of electrons is modeled as the product of the electron-molecule inelastic collision factor δ and the elastic energy loss. Physically, the δ factor accounts for the fraction of the electron energy that is transferred into the vibration, rotation, electronic excitation, and ionization modes of the hydrogen or nitrogen molecules.

In Ref. 24, δ is obtained by numerically solving the Boltzmann equation with a two-term spherical harmonic expansion of the electron energy distribution function. The resulting electron energy distribution is non-Maxwellian, although internal Langmuir probe diagnostics⁶ indicate Maxwellian distribution. The value of δ varies with electron energy. For electron temperatures above 10000 K, the δ values are approximately 10 for hydrogen molecules, and 800 for nitrogen molecules. These δ values are referred to as variable δ in this paper. In Ref. 1, the effective δ value for both hydrogen and nitrogen molecules is assumed to be constant and equal to 3000. This δ value of 3000 yields results that agree reasonably well with the experimental data near the exit plane and at the anode.³⁻⁶ Tiliakos⁶ concluded, based on Langmuir probe measurements along the anode wall of a 1 kW hydrazine arcjet operating at 10 A, 50 mg/s, that δ has a value of

approximately 1200. Hence, the cathode sheath solutions are obtained for three δ factors: variable, 1200, and 3000.

Results and Discussion

Based on the above discussion, an attachment area of $2.0 \times 10^{-8} \text{ m}^2$, a cathode tip temperature of 3680 K, and a pure tungsten cathode tip material are chosen as the nominal input to the modified Fujita cathode sheath model. The electron-molecule inelastic collision δ factor was taken as variable, 1200, and 3000. The nominal flow conditions are for a mass flow rate of 50 mg/s, 10 A arcjet current, hydrazine propellant, and 1 kW arcjet geometry. The density ratio of hydrogen ions to nitrogen ions is greater than 100 in the neutral plasma near the cathode, so only the hydrogen ions are accounted for in the sheath model. Ambipolar diffusion current is calculated using properties of the near-cathode bulk plasma, requiring location of the computational grid $j = 2$ as close to the cathode as possible. The present grid is 60 axial, 15 radial for the fluid domain. In a grid refinement study, the radial grid is refined from 15 to 25, reducing the radial distance from the cathode tip to the nearest grid to approximately half that for the 15 grid case.

The grid spacing for the coarse grid is approximately 5 to 6 hydrogen atom mean free paths for the three δ values. For the fine grid, the grid spacing is 3 to 4 hydrogen atom mean free paths. Even for the coarse grid, the continuum assumption is barely satisfied. More reduction in grid spacing would violate the continuum assumption of the bulk plasma solution. Moreover, the electron diffusion speed must not exceed the electron random thermal speed. This restriction can be expressed as:

$$\frac{2\Delta x}{\lambda_e} > 1 \quad (13)$$

i.e., the electron mean free path must be less than twice the grid spacing. For the coarse grid, $2\Delta x/\lambda_e$ is about 12.5 axially and 10 radially at the cathode tip, and is smaller for the fine grid case. It is evident that the grid spacing is very close to the minimum limit so that only 15 radial grids are used for the calculations.

The properties of the bulk plasma at $j = 2$ are summarized in Table 2. The electron temperature and number density do not vary monotonically with δ , although the values for all three cases are close. Because a large δ value indicates more inelastic energy transfer from the electrons to the molecules, it might be expected that the electron temperature should decrease as δ increases. However, δ also affects the anode attachment region, and therefore the current distribution and ohmic heating in the arcjet. Hence, the electron temperature is a result of the combination of these two effects, and is insensitive to δ .

Table 2 *Properties of the bulk plasma at grid line $j = 2$ for the nominal case.*

δ	T_e , K	n_e , m^{-3}
*variable	11320	0.90×10^{23}
1200	11470	1.02×10^{23}
3000	11360	0.93×10^{23}

* $\delta_{H_2} \approx 10$, $\delta_{N_2} \approx 800$ for $T_e > 11,000$ K.

In Fig. 6, sheath potential values are obtained for various assumed sheath thickness from 0.5 to 0.7 times the Debye length. Note that the Debye length varies with sheath thickness, and that the sheath thickness is about 37 nm at an ambient pressure of 3.7 atm. Both the sheath potential and the electron temperature vary linearly as the sheath thickness increases. The cathode surface electric field and electron number density are approximately 1.4×10^9 volts/m and 1.90 - $2.0 \times 10^{22} m^{-3}$, respectively, for this range. At an electron temperature of 11320 K, matching the MKB model, the sheath potential ϕ_0 is about -50 volts.

Note that the cathode surface electric field E_c from the modified Fujita model does not satisfy the Poisson equation, which is:

$$\frac{dE}{dx} = -\frac{d^2\phi}{dx^2} = \frac{e}{\epsilon_0}(n_i - n_e), \quad (14)$$

where n_i is the ion number density. From Eq. (14), the change in electric field across the sheath could be estimated as (based on $n_i \approx n_d$ and $n_e \approx 0$): $\Delta E \approx en_d/\epsilon_0 \approx 10^7$ V/m, which is two orders

of magnitude smaller than $-\phi_0/d$. This discrepancy is a direct result of requiring a discontinuity in electric field at the sheath edge by the modified Fujita model, implying a shock-like charge layer at the sheath edge. With ΔE relatively small, the electric field is approximately constant across the sheath, and it follows that $E_C = -\phi_0/d$, which is Eq. (10). The sheath thickness d is significant in that it is needed to provide an equation for E_C , and it should not be regarded as the physical thickness of the sheath.

The value of q is 0.32, indicating 32% of the electrons are emitted through the tunnel effect. This gives $\pi q/\sin(\pi q) = 1.2$, and the Schottky emission is modified by this factor. The work function of tungsten is lowered 1.4 volts by the surface electric field. The calculated current density and electric field roughly agree with the peak current density of approximately $4 \times 10^8 \text{ A/m}^2$ and average electric field of $3.64 \times 10^8 \text{ volts/m}$ in Ref. 14. However, a theoretical value of $A = 1.202 \times 10^6 \text{ A/m}^2\text{-K}^2$ is used in Ref. 14. If the experimental value of $0.60 \times 10^6 \text{ A/m}^2\text{-K}^2$ and a cathode temperature of 3680 K were used, Schottky emission then yields an effective tungsten work function of 3.15 volts, in good agreement with the modified Fujita model.

Current density contributions and the associated heat transfer for the nominal case with variable δ are summarized in Table 3. Because of the highly negative sheath potential of - 50 volts, few electrons have enough thermal energy to overcome the potential barrier to reach the cathode. Hence, the main contributors to energy balance at the cathode are the ions and the emitted electrons. Ions heat the cathode, and the emitted electrons cool the cathode; and the heat transfer due to electrons and ions is essentially equal and opposite (Table 3). Under these conditions, the cathode radiative power loss is less than 10^7 Watts/m^2 , which is about 1% of the ion heating or electron cooling.

Table 3 *Current density and associated heat transfer for the nominal case, variable δ .*

	thermal electron	ion	emitted electron
$j, \text{ A/m}^2$	8.9×10^{-15}	-2.9×10^7	-4.7×10^8
heat transfer, Watts/m^2	4.5×10^{-14}	1.80×10^9	-1.80×10^9

In the cathode energy equation, vaporization of the cathode material and convective heat transfer to the cathode are neglected. The power needed to melt the cathode tungsten ($H_f = 190$ kJ/kg) is estimated to be about 6 Watts/m² based on the molten crater diameter of 0.8 mm after 1000 hours of operation at 1 kW¹³. The convective heat transfer to the cathode tip is estimated by the one-dimensional Fourier conduction equation $-k(dT_g/dr)$, where k is approximately 0.8 Watts/m-K, according to the MKB model. For the variable δ case, the MKB model data yields a convective heat transfer of 9.1×10^7 Watts/m² to the cathode tip. This is about 5% of the power transfer to the cathode tip by ion current. When convective heat transfer is included in the modified Fujita model, the sheath potential reduces from - 50 to - 47.5 volts, approximately 5% less negative. For $\delta = 1200$, the convective heat transfer is about 20% of the power transfer due to the ion current, and this makes the sheath potential change from -29 to -24 volts, less negative by about 18%.

It is noted here that in the MKB model the cathode temperature is specified as 1000 K at the inlet, and then linearly interpolated up to 3680 K at the cathode tip. Hence, the cathode tip is in fact insulated in the MKB model, and it is consistent for the modified Fujita model to neglect the convective heat transfer. In reality, the cathode tip also loses power to the upstream portion of the cathode. To be fully consistent, there should be a cathode heat transfer model which includes the convective heat transfer from the flow and the conductive heat transfer in the cathode.

Similarly, solutions are obtained for the nominal case with $\delta = 1200$ and 3000, respectively. The sheath model solutions for $\delta =$ variable, 1200, and 3000 are summarized in Table 4. The 1200 and 3000 solutions are almost identical. Compared to the variable δ case, the sheath potential of approximately -30 volts is about 40% less negative, and the sheath thickness is about 40% thinner. The magnitude of the sheath potential still increases linearly with sheath thickness at the 1200 and 3000 values. The electron/ion number densities at the sheath edge are about 45% larger than that for the variable δ case. Note that for all three cases, the electron number density at the sheath edge is lower than that at $j = 2$. This is expected because ion

current in the sheath is generated by the ambipolar diffusion current, thus requiring a gradient to drive this current component. The values of q , E_C , and ϕ_E are almost equal for the three cases. The sheath thickness is about half of a Debye length for all three cases.

Table 4 *Sheath model solutions for the nominal case with $\delta = \text{variable}, 1200, \text{ and } 3000$.*

δ	ϕ_0	$d, \text{ nm}$	$n_d, \text{ m}^{-3}$	q	$E_C, \text{ volts/m}$	$\phi_E, \text{ volts}$
variable	-49.9	37	1.9×10^{22}	0.319	1.36×10^9	1.40
1200	-29.1	22	2.8×10^{22}	0.316	1.35×10^9	1.39
3000	-31.5	23	2.7×10^{22}	0.316	1.35×10^9	1.39

The current density components and the associated heat transfer for the nominal case with constant $\delta = 1200$ and 3000 are summarized in Tables 5 and 6. The thermal electron current density increases from order of 10^{-14} to order of 10^{-4} A/m^2 due to the less negative sheath potential in the exponential term. However, the heat transfer due to thermal electrons is still negligible. The contribution from the radiative power is still less than 1%. Because the ion current density is below 10% of the total current density in the cases considered, the contribution of the secondary electron emission is approximately 1% and can be neglected.

Table 5 *Current density and associated heat transfer for the nominal case, $\delta = 1200$.*

	thermal electron	ion	emitted electron
$j, \text{ A/m}^2$	1.37×10^{-4}	-4.4×10^7	-4.6×10^8
heat transfer, Watts/m^2	7.1×10^{-4}	1.76×10^9	-1.75×10^9

Table 6 *Current density and associated heat transfer for the nominal case, $\delta = 3000$.*

	thermal electron	ion	emitted electron
$j, \text{ A/m}^2$	1.0×10^{-4}	-4.2×10^7	-4.6×10^8
heat transfer, Watts/m^2	5.0×10^{-4}	1.76×10^9	-1.75×10^9

Arcjet potential distribution

The contributions of cathode sheath, plasma, and anode sheath to the total arcjet voltage are summarized in Table 7. The cathode sheath voltage and the plasma voltage are obtained from the modified Fujita sheath model and the MKB arcjet model.^{1,2} The anode sheath voltage is obtained from anode probe measurements.⁶ Although the plasma voltages are quite different between the two constant δ and the variable δ case, the total voltages are fairly close as the modified Fujita sheath model compensates for the decrease in plasma voltage by yielding more sheath voltage. The experimental total voltage is about -112 volts for mass flow rate of 50 mg/s and arcjet current of -9.8 A. It is estimated that cathode erosion, which is not accounted for in the arcjet model, may yield an additional -3 to -5 volts to the plasma voltage. Hence, the total voltage prediction from the combined numerical and experimental results agrees well with the experimental value. The similar total voltage predictions for all three values of δ makes it difficult to determine which one is the most reasonable.

Table 7 *The arcjet voltage distribution for the 50 mg/s, 10A.*

voltage, volts	variable δ	$\delta = 1200$	$\delta = 3000$
cathode	- 49.9	- 29.1	- 31.5
plasma	- 44.3	- 65.7	- 68.9
*anode ⁶	- 11.3	- 11.3	- 11.3
total	-105.5	- 106.1	- 111.7

* from anode probe measurements, with ± 2.4 V uncertainty.

A somewhat indirect criterion for selecting a reasonable δ values is the agreement between the model predictions and the experimental data at the exit plane²⁵ and at the nozzle wall⁶. The agreement at the exit plane favors $\delta = 1200$ or 3000, as shown in Table 8. The measured current density at the nozzle wall also favors the model predictions for $\delta = 1200$.⁶ Arcjet voltage, and therefore power, is consistent with $\delta = 1200$ (Table 7). A value of $\delta = 1200$ is therefore adopted, in the absence of a more accurate approach of solving the molecule vibrational temperature separately from the electron and the heavy species temperatures.

Table 8 Exit plane electron temperature and number density from model predictions (nominal case) and emission spectroscopy measurements²⁵ (1.5 kW hydrazine arcjet operating at 50 mg/s).

	variable δ	$\delta = 1200$	$\delta = 3000$	experimental ²⁵
T_e , K	1770	2590	2530	3000
n_e , m ⁻³	0.394×10^{20}	1.33×10^{20}	1.37×10^{20}	1.30×10^{20}

The modified Fujita sheath solutions are sensitive to the value of the attachment area. When the attachment area is halved, keeping other conditions the same as the nominal case, with $\delta = 1200$, the sheath potential is about - 68 volts with a sheath thickness of 0.90 Debye lengths. Similarly, doubling the attachment area yields a sheath voltage of only - 9 volts with a sheath thickness of 0.23 Debye lengths. The justification for selecting the chosen attachment area is that it produces a solution giving overall agreement with the total voltage of the arcjet. Unfortunately, no way is known at this time to measure attachment area independently.

Because of the uncertainty in tungsten emissivity, solutions for a cathode tip temperature of 3800 K were also obtained, with other conditions nominal. In Table 9, results for cathode tip temperatures of 3680 and 3800 K are compared for the case of $\delta = 1200$. For the higher cathode tip temperature, the sheath potential increases slightly, and the sheath thickness increases by about 28%. The cathode electric field decreases about 15%. Consequently, the fraction of electrons emitted through the tunneling effect decreases about 14%. The lowering of the tungsten potential decreases about 7%. These decreases are expected, because as the cathode tip temperature increases, more electrons are emitted through thermionic emission. The arcjet total voltage and its components are summarized in Table 10 for the cathode tip temperature of 3800 K. Note that the plasma voltage and the anode sheath voltage remain the same. The additional voltage in the cathode sheath is less than - 3 volts for all three cases.

Table 9 Comparisons of the sheath model solutions for cathode tip temperature of 3680 and 3800 K for $\delta = 1200$, and other conditions nominal.

T_c , K	ϕ_o	d, nm	n_d , m ⁻³	q	E_c , volts/m	ϕ_E , volts
3680	- 29.1	22	2.8×10^{22}	0.316	1.35×10^9	1.39
3800	- 31.4	28	2.8×10^{22}	0.271	1.15×10^9	1.29

Table 10 *The arcjet voltage distribution for cathode tip temperature of 3800 K, other conditions nominal.*

voltage, volts	variable δ	$\delta = 1200$	$\delta = 3000$
cathode	-52.7	-31.4	-33.7
plasma	- 44.3	- 65.7	- 68.9
*anode ⁶	- 11.3	- 11.3	- 11.3
total	- 108.3	- 108.4	- 113.9

*from anode probe measurements, with ± 2.4 volts uncertainty.

According to the MKB model, the predicted plasma voltage drop from the cathode to the constrictor exit is approximately - 30 volts for the nominal case with $\delta = 1200$. Together with the - 30 V in the cathode sheath, over half (-60 volts) of the total arcjet voltage drop (-112 volts) occurs in a distance of 0.25 mm (the constrictor length) just off the cathode tip. This corresponds to a volumetric power deposition of approximately 10^{13} W/m³.

Conclusions (Part A)

For a 1 kW hydrazine arcjet operating at 50 mg/s, the modified Fujita sheath model predicts a cathode sheath potential of approximately - 30 volts. The sheath thickness is approximately 0.50 Debye lengths. The electric field at the cathode surface significantly enhances the electron emission through the Schottky and tunneling effects. Combined with the arcjet model prediction and the anode probe measurements, the modified Fujita sheath model is able to obtain a total arcjet voltage in good agreement with the experimental value. However, the modified Fujita sheath model is not consistent with the Poisson equation. Moreover, there are uncertainties in the energy equation due to the lack of a cathode thermal model. A more rigorous approach is to solve the Poisson equation coupled with a cathode thermal model. This approach is presented in the second part of this paper.

Part B: Goodfellow Cathode Model

This section will discuss the application of a previously developed model to the operating conditions described in part A. This cathode model consists of two parts, namely a near-cathode plasma model and a thermal model of the cathode. The near-cathode plasma model connects the properties of the main plasma with the cathode. Specifically, given the plasma properties within a mean-free-path of the surface, the near-cathode model predicts the heat flux and current density to the cathode surface. With these boundary conditions and the traditional thermal transport mechanisms, the thermal model can predict the temperature distribution within the cathode. Because of the strong interdependency of the two models, they must be solved simultaneously. The characteristics of this model will be briefly discussed here. A complete description and experimental validation are presented in Reference 23.

Near-Cathode Plasma Model

An illustration of the near-cathode plasma is shown in Fig. 7. The Debye length, mean free path, and thermal, concentration and momentum boundary layers are represented by λ_D , λ and $L_{T,C,M}$ respectively. For this study, only the surface, sheath, presheath and ionization regions are modeled. In the main body of the plasma, the current is predominantly carried by the electrons, while in the sheath region the ion current may dominate. To match these regions an ionization region (which produces the required number of ions for the sheath region) is required between the sheath and the main plasma body. Similarly, a recombination region exists at the cathode surface to produce a transition to pure electron conduction in the solid. At the surface, ions are also converted to neutrals, which then return to the plasma.

In general, the cathode surface is characterized by the material, the surface finish and the temperature. For this model, the recombination region is assumed to be infinitesimally thin and is considered as a surface effect. Incident ions from the sheath heat the surface while emitted electrons cool the surface. The energy equation at the surface balances the energy that is

deposited and removed by the particles with heat conduction into the solid, and with radiative, convective and mass (surface erosion) transport to the surroundings. The surface heat flux is the net of the energy deposited from the incident ions and plasma electrons, and the energy removed by the thermionic electrons. The incident ions are recombined and reemitted as neutrals. The dominant heating mechanism is the energy deposited by the incident ions while the dominant cooling mechanism is from thermionic emission. Thermionic emission is described by the Richardson-Dushman relation.²⁶ In addition, the surface electric field acts to enhance the emission, a phenomenon known as the Schottky effect.²⁶ The magnitude of the electric field at the cathode surface is primarily determined by the characteristics of the sheath region.

The sheath region is assumed to contain collisionless particles with constant total energy (potential plus kinetic). This model is a variation of the model originally presented by Prewett and Allen.²⁷ Six particle species are considered: monoenergetic thermionic or beam electrons, singly- and doubly-charged monoenergetic ions for two monatomic gases, and Maxwellian electrons originating in the plasma.²³ Further, the sheath thickness is assumed to be much less than the Larmor radii of the particles, and therefore, magnetic field effects on the particle trajectories are negligible.

For a stable sheath to occur, the ions must enter the sheath with energies equal to or greater than the Bohm minimum energy.²⁸ The ions here are assumed to enter the sheath with energies equal to the Bohm minimum energy, which is represented as the Bohm potential. The plasma electrons are assumed to be Maxwellian and referenced to the electron density at the sheath edge. These electrons fall into two classes; those with sufficient kinetic energy to overcome the sheath retarding potential and reach the cathode surface, and those with insufficient energy that are repelled back to the main plasma. The corresponding flux of the high energy electrons constitutes the plasma electron current. The one-dimensional Poisson charge equation is solved to describe the electric field and the electric potential distributions within the sheath.

The ionization and presheath regions connect the sheath region with the main plasma body.^{26,29} The purpose of the presheath region is to accelerate the ions so that they enter the

sheath region with the minimum energy required for a stable sheath (Bohm energy).²⁸ For this model the presheath region is combined with the ionization zone by requiring that ions leave the ionization region with the Bohm energy. The ionization region generates the required number of ion and electron pairs to match the sheath and main plasma body values. The plasma temperature is determined from the energy balance in this region and the particle number densities are determined by the Saha equation (equilibrium ionization/recombination).

Thermal Model

For a given set of boundary conditions, a quasi-two-dimensional axisymmetric thermal model is used to describe the temperature distribution within the cathode. This model determines the axial temperature distribution subject to radial surface radiation, and ohmic heating. The cathode base temperature is fixed and the heat load at the tip is calculated by the near-cathode plasma model. For these calculations, the base temperature is 1000 K, the surface emissivity is 0.5, and the environmental/anode temperature is 500 K, consistent with a water-cooled arcjet. A surface emissivity of 0.5 is assumed. Note that the radiation cooling effects are small so that using emissivity values of 0.5 or 0.57 has little effect.²⁶ The thermal conductivity is assumed to be constant while the electrical resistivity is temperature dependent.

Past one-dimensional thermal models have assumed that the arc attachment area covered the entire tip,²⁹⁻³¹ which in itself presents two problems. First, a changing surface temperature will significantly change the current density and therefore the total current. For cases where ohmic heating is significant this change in the total current will significantly affect the thermal model. Comparing the effects of the different parameters at constant current becomes difficult, since each case produces a different total current. Second, the arc attachment assumption does not correctly account for operation in which the attachment area covers only a small portion of the tip. To correct this problem, a two-dimensional thermal conduction approximation, a surface fit of solutions from a two-dimensional thermal model, is added at the cathode tip. This model

relates three normalized parameters: the ratio of cathode spot temperature to average cathode tip temperature, the ratio of the spot radius to the cathode tip radius, and a normalized heat load.²³

The plasma model and the thermal model are combined to form the overall solution. Solutions are found where the heat flux curves for the two solutions intersect. In general there may be four possible solutions; the trivial solution, two low temperature solutions, and a high temperature solution (typically around where the plasma reaches full ionization as with the previous models). The second low temperature point is a result of adding the quasi-two-dimensional approximation to the thermal model described above.^{21,23} Note that the solution point near full ionization grossly over-predicts the cathode temperature.

Comparisons with Results from the Modified Fujita Model

The cathode geometry considered is a conical tipped cathode with 6 mm along the cone exposed to the plasma. The base diameter is 4.76 mm and the flattened tip diameter is 1 mm. (Base to tip diameter ratios of 4.5 to 5.0 were typically seen on over ten long-duration high-current ammonia arcjet tests at the Jet Propulsion Laboratory). The material is pure tungsten (work function = 4.5 eV, Richardson Coefficient = $6.0 \times 10^5 \text{ A/m}^2\text{-K}^2$). The gas is considered as a monatomic mixture of one part nitrogen and two parts hydrogen (simulated hydrazine) at a total pressure of 370 kPa. The total current is 10 A.

The input parameters for the combined model are the total pressure, the total current, and one of the following: cathode temperature, sheath voltage, or attachment area (current density). The cathode temperature is the best understood of these three parameters. Attachment area estimates can easily vary by more than an order of magnitude depending on which attachment theory is used.¹⁶ Post-test observations of arcjets indicate that the attachment spot is at the melting point or a little above.

The results of the model for the 10 A discharge at a pressure of 370 kPa and simulated hydrazine propellant are shown in Figs. 8 and 9 as functions of the cathode spot temperature. Figure 8 shows that for a given sheath voltage two cathode temperature solutions exist. These

are the two low-temperature solutions mentioned previously. *However, only solutions to the left of the peak in the sheath voltage are stable.* Although a cathode temperature near the melting point of tungsten, 3680 K, is on the unstable solution side, the results are still useful. The location of the peak sheath voltage is primarily affected by the characteristics of the two-dimensional tip approximation thermal model. An existing approximation used here is for a rectangular tipped cathode rather than a conical shaped one.²³ The conical shape increases the axial thermal resistance and would therefore move the cathode temperature corresponding to the peak sheath voltage to higher cathode temperature values. This will probably move the molten tip temperature to the stable side but would not significantly change the results.

A comparison between this model and the model presented in part A is listed in Table 11 for a cathode spot temperature of 3680 K. There is good agreement in the electron temperature, electron number density, and sheath voltage between the models. This indicates that there is good agreement in the plasma models at the sheath edge (MKB model and Goodfellow ionization region) and the energy balances. However, there is a factor of 20 difference in the surface electric field. The difference in the effective work function is also a result of the electric field difference (Schottky effect). The current density difference, which is over a factor of 10, is also primarily a result of the electric field through the lowering of the work function, since the same cathode temperature is used. The 1.4 eV lowering of the surface work function from the surface electric field from the Fujita model is much larger than is normally observed for thermo-field emission. Although, this lowering is possible, it is not likely.²⁶

The modified Fujita model treats the electric field as a shock type discontinuity at the sheath edge and therefore does not resolve the particle distributions within the sheath. The electric field (1.4×10^9 V/m) is almost constant across the sheath because the charge density (2.8×10^{22} m⁻³) does not have a large effect on the high electric field.

The Goodfellow sheath model solves the continuity and energy equations for each particle species (ions, plasma electrons, and thermionic electrons are considered for two gas types) to get number density distributions within the sheath. Electrons originating in the plasma

are considered to be Maxwellian. These number density relations are integrated in the Poisson charge equation to get the electric field distribution and therefore the electric field at the cathode surface.²³ From this, one can get a relation between normalized surface electric field (ϵ_c), and normalized thermionic current density (J_b), for different normalized sheath voltages (η_c), as seen in Fig. 10. The maximum surface electric field exists when the thermionic current is zero. For $\eta_c = 27.45$ (modified Fujita) and $\eta_c = 34.4$ (Goodfellow) the maximum values of ϵ_c are both about 3.4. The maximum surface electric fields are 6.29×10^7 V/m (modified Fujita) and 7.2×10^7 V/m (Goodfellow). The electric field calculated using the Fujita model (1.35×10^9 V/m) is a factor of 23 larger than the maximum calculated from the Goodfellow model. If the field reduction due to the thermionic electrons is added, discussed below, the difference will be even larger. This electric field difference corresponds to a work function difference of a factor of about 4.8 using the Schottky effect.

Table 11 *Comparison of model results.*

Parameter	Modified Fujita	Goodfellow
cathode spot temperature (K)	3680 (input)	3680 (input)*
electron temperature (eV)	0.989 (matched to MKB model)	0.843
ionization fraction	1.45%	1.27%
electron number density (m^{-3})	2.8×10^{22}	2.67×10^{22}
Sheath Voltage (volts)	29.1	29.0 *
Attachment area (m^2)	2.0×10^{-8} (input)	2.289×10^{-7} *
total current density (A/m^2)	5×10^8	4.37×10^7
ion current density (A/m^2)	4.4×10^7	$(2.45 + 0.375) \times 10^7$
surface electric field (V/m)	1.35×10^9	7.17×10^7
effective work function (eV)	3.1	4.17
work function lowering (eV)	1.4	0.33
Debye length (m)	4.4×10^{-8}	4.17×10^{-8}
heat flux to cathode (W/m^2)	0 (to satisfy MKB model)	1.011×10^9
heat load to cathode (W)	0 (to satisfy MKB model)	228

*only one of these three input parameters is needed.

As the thermionic current increases, the surface electric field decreases, due to the presence of the thermionic electrons near the surface, as seen in Fig. 10. The thermionic electrons are emitted with a low energy (cathode thermal energy) and are quickly accelerated out of the sheath.

If there are a sufficiently large number of thermionic electrons near the cathode surface, a double-sheath may be formed. That is, a negatively charged layer next to the surface may be followed by a positive charge layer further away from the surface. The presence of a double-sheath is not necessarily important, but the presence of thermionic electrons near the surface decreases the local space charge, with a resulting lowering of the local electric field. For the conditions in the case of normalized thermionic current $J_b = 0.0277$ and 0, the results are not too different, indicating that the thermionic current effects, although noticeable, are small. For the $J_b = 0.277$ case ($5 \times 10^8 \text{ A/m}^2$), however, there is a significant effect. The surface electric field is lowered by a factor of 1.5 from the $J_b = 0.0277$ case ($5 \times 10^7 \text{ A/m}^2$). A comparison for a simplified case where all of the current is assumed to be thermionic is shown in Table 12. This assumption will over-predict the effects since the ion current is neglected. However, the trends and magnitudes will be the same. The values used in the comparison are: $n_e = 1.9 \times 10^{22} \text{ m}^{-3}$, sheath voltage = 27.2 volts, $T_e = 1.0 \text{ eV}$.

The first three columns in Table 12 are the results of the Goodfellow model. The second to last column shows the modified Fujita/Goodfellow surface E-field ratio calculated with this model. In all conditions, the modified Fujita/Goodfellow surface E-field ratio is more than an order of magnitude. The last column, T_c , indicates the required cathode temperature to get the prescribed current density using the calculated electric field, (Schottky equation and standard Richardson equation used for simplicity).

Table 12 *Simplified sheath comparisons.*

J_b	ϵ_c	surface E-field (V/m)	reduction in work function (eV)	modified Fujita/Goodfellow surface E-field ratio	T_c (K)
0	5.44	1.01×10^8	0.38	14	small
0.0277	5.24	9.7×10^7	0.37	15	3950
0.2770	3.45	6.4×10^7	0.30	23	4770

Conclusions (Part B)

Comparisons between two cathode models have shown good agreement for the determination of the sheath voltage, electron temperature and electron number density. Neglect of the Poisson equation in the modified Fujita model results in a surface E-field a factor of 10 or more higher than that calculated from the Goodfellow model. The large difference in the electric field also produces a large difference (1.4 volts versus 0.35 volts) in the lowering of the work function, and more than a factor of 10 difference in the current density. Direct measurements of the current density or the electric field near the cathode surface are required to determine which model more closely describes the physics.

Acknowledgments

The research described in Part A of this paper was funded by the Air Force Office of Scientific Research under contract F49620-95-1-0363. Dr. Mitat Birkan is the Program Manager. The authors thank Prof. M. Kushner (Department of Electrical and Computer Engineering, University of Illinois at Urbana-Champaign) for invaluable advice in the cathode sheath model and the maximum limit on electron diffusion speed. We also acknowledge helpful discussions with Dr. K. Fujita in the Institute of Space and Astronautical Science in Japan, Dr. T. Megli of Ford Motor Co., and N. Tiliakos (Dept. of Aeronautical and Astronautical Engineering, University of Illinois at Urbana-Champaign).

The research described in part B of this paper was conducted at the Jet Propulsion Laboratory/ California Institute of Technology under contract with the National Aeronautics and Space Administration.

References

- ¹Megli, T. W., Krier, H., and Burton, R. L., "Plasmadynamics Model for Nonequilibrium Processes in N_2/H_2 Arcjets," *Journal of Thermophysics and Heat Transfer*, Vol. 10, No. 4, 1996, pp. 554-562.
- ²Megli, T. W., Lu, J., Krier, H., and Burton, R. L., "Modeling Plasma Processes in 1 kW Hydrazine Arcjet Thrusters," AIAA Paper No. 96-2965, July, 1996. (*in review, Journal of Propulsion and Power*)
- ³Buften, S. A., Burton, R. L., and Krier, H., "Measured Plasma Properties at the Exit Plane of a 1 kW Arcjet," AIAA Paper No. 95-3066, July, 1995.
- ⁴Burton, R. L., and Buften, S. A., "Exit-Plane Electrostatic Probe Measurements of a Low Power Arcjet," *Journal of Propulsion and Power*, Vol. 12, No. 6, 1996, pp. 1099-1106.
- ⁵Tiliakos, N. T., Burton, R. L., and Krier, H., "Energy Transfer to the Anode of a 1 kW Arcjet," AIAA Paper No. 96-2964, July, 1996.
- ⁶Tiliakos, N. T., "Plasma Properties and Heating at the Anode of a 1 kW Arcjet Using Electrostatic Probes," Ph.D. thesis, Department of Aeronautical and Astronautical Engineering, University of Illinois, Urbana, IL, 1997; also AIAA Paper No. 97-3201, "Arcjet Anode Plasma Measurements Using Electrostatic Probes," July, 1997. (*in review, Journal of Propulsion and Power*)
- ⁷Fujita, K. "Performance Computation of a Low-Power Hydrogen Arcjet," AIAA Paper No. 96-3183, July, 1996.
- ⁸Swanson, L. W., and Bell, A. E., "Recent Advances in Field Electron Microscopy of Metals," *Advances in Electronics and Electron Physics*, L. Marton ed., Academic Press, New York, 1973, pp. 296-304.
- ⁹Nichols, L. D., and Mantenieks, M. A., "Analytical and Experimental Studies of MHD Generator Cathodes Emitting in a "Spot" Mode," NASA TN D-5414, Washington D.C., Sept., 1969.

- ¹⁰Subramaniam, V. V., and Hoyter, K. S., "Limits on Steady Diffuse Mode Operation of the Cathode in Magnetoplasma dynamic Thrusters," *Journal of Propulsion and Power*, Vol. 7, No. 4, 1991, pp. 565-572.
- ¹¹Zhou, X., Heberlein, J., and Pfender, E., "Model Predictions of Arc Cathode Erosion Rate Dependence on Plasma Gas and on Cathode Material," *Electrical Contacts*, Sept. 1993, pp. 229-235.
- ¹²Durgapal, P., "Current Distribution in the Cathode Area of an Arcjet," *Journal of Thermophysics and Heat Transfer*, Vol. 7, No. 2, 1993, pp. 241-250.
- ¹³Curran, F. M., and Haag, T. W., "Extended Life and Performance Test of a Low-Power Arcjet," *Journal of Spacecraft and Rockets*, Vol. 29, No. 4, 1992, pp. 444-452.
- ¹⁴Berns, D., Storm, P. V., and Cappelli, M. A., "Spectral Imaging of the Arcjet Electrode Region," AIAA Paper No. 95-1957, June, 1995.
- ¹⁵Berns, D., Storm, P. V., Hargus Jr., A., Cappelli, M. A., McFall, K. A., and Spores, R. A., "Plasma and Cathode Emission from a High Power Hydrogen Arcjet Thruster," AIAA Paper No. 96-2703, July, 1996.
- ¹⁶Cobine, J. D., *Gaseous Conductors*, Dover Publications, New York, 1958, p. 302.
- ¹⁷Guile, A. E., "Arc-Electrode Phenomena," *Proceedings of IEE, IEE Reviews*, Vol. 18, No. 9R, 1971, pp. 1131-1154.
- ¹⁸Somerville, J. M., *The Electric Arc*, New York: John Wiley and Sons Inc., 1959, pp. 64-73.
- ¹⁹Wilbur, P. J., Jahn, R. G., and Curran, F. C., "Space Electric Propulsion Plasmas," *IEEE Transactions on Plasma Science*, Vol. 19, No. 6, 1991, pp. 1167-1179.
- ²⁰Morrow, R., and Lowke, J. J., "A One-Dimensional Theory for the Electrode Sheaths of Electric Arcs," *Journal of Physics D: Applied Physics*, Vol. 26, No. 4, 1993, pp. 634-642.
- ²¹Goodfellow, K. D., and Polk, J. E., "Theoretical Investigation of Cathode Operation in High-Power Arcjets," AIAA Paper No. 95-3061, July, 1995.
- ²²Goodfellow, K. D., and Polk, J. E., "Experimental Verification of a High-Current Cathode Thermal Model," AIAA Paper No. 95-3062, July, 1995.
- ²³Goodfellow, K. D., "A Theoretical and Experimental Investigation of Cathode Processes in Electric Thrusters," Ph.D. dissertation, Department of Aerospace Engineering, University of Southern California, Los Angeles, CA, 1996.
- ²⁴Morgan, W. L., and Penetrante, B. M., MacELENDIF version 1.1, Kinema Software, 1994.

- ²⁵Zube, D. M., and Auweter-Kurtz, M., "Spectroscopic Arcjet Diagnostic Under Thermal Equilibrium and Non-equilibrium Conditions," AIAA Paper No. 93-1792, June, 1993.
- ²⁶Neumann, W., *The Mechanism of the Thermoemitting Arc Cathode*, Akademie-Verlag Press, Berlin, Germany, 1987, pp. 20-44.
- ²⁷Prewett, P. D. and Allen, J. E., "The Double Sheath Associated with a Hot Cathode," *Proceedings of the Royal Society of London*, 348, 1976, pp. 435-446.
- ²⁸Bohm, D., *The Characteristics of Electrical Discharges in Magnetic Plasma*, McGraw Hill, New York, NY, 1949, pp. 77-86.
- ²⁹Bade, W. L. and Yos, J. M., Arcjet Technology Research and Development-Final Report, Technical Report NASA CR-54687, AVCO Corporation, Wilmington, MA, 1965.
- ³⁰Zhou, X., Berns, D. and Heberlein, J., "Investigation of Arc-Cathode Interaction," AIAA Paper 94-3129, July, 1994.
- ³¹Goodfellow, K. D., Pivrotto, T. J., and Polk, J. E., "Applied-Field Magnetoplasma-dynamic Engine Developments," AIAA Paper 92-3293, July, 1992.
- ³²Goodfellow, K. D., and Polk, J. E., "High Current Cathode Thermal Behavior, Part I: Theory," IEPC Paper 93-030, Sept. 1993.
- ³³Haydon, S. C., *Discharge and Plasma Physics*, Department of University Extension, The University of New England, Armidale, N. S. W., Australia, 1964, pp. 319--343.

Figure Captions

Fig. 1 Schematic of a 1 kW electrothermal arcjet thruster. A voltage difference between the cathode and anode produces an electrical discharge which heats the propellant. The thermal energy is converted to kinetic energy as the propellant expands to high velocities in the converging-diverging nozzle.

Fig. 2 One dimensional collisionless sheath model.

Fig. 3 Electron temperature T_e contours in the constrictor region of a 1 kW arcjet operating at 10 A, 50mg/sec. The exit plane is located at $x = 18.4$ mm.

Fig. 4 The sheath edge and the near-cathode computational grid.

Fig. 5 Arcjet cathode temperature as a function of tungsten emissivity, assuming constant radiative power from the cathode with $P_{\text{rad}} = 5.81 \times 10^6$ Watts/m².

Fig. 6 Sheath potential and the sheath edge electron temperature at various sheath thickness for the nominal case with variable δ . The solution matching occurs at $\phi_0 = -50$ volts, $d = 37$ nm, and $T_{\text{ed}} = 11320$ K.

Fig. 7 Near-cathode plasma regions for the Goodfellow model.

Fig. 8 Sheath Voltage and attachment area as a function of cathode temperature, Goodfellow model.

Fig. 9 Electron temperature and effective work function as a function of cathode temperature.

Fig. 10 Normalized electric field as a function of normalized thermionic current density.

Fig. 11 Normalized electric field as a function of normalized position with normalized thermionic current density as a parameter.

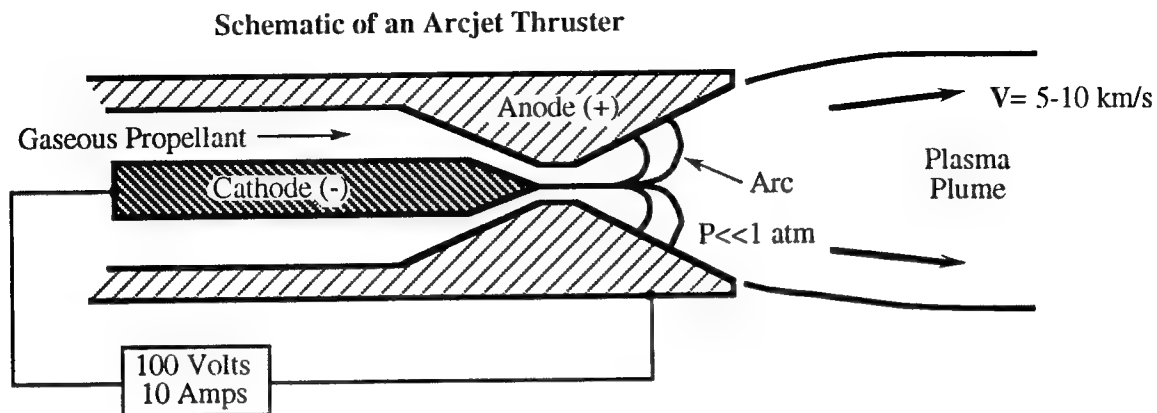


Fig. 1 Schematic of a 1 kW electrothermal arcjet thruster. A voltage difference between the cathode and anode produces an electrical discharge which heats the propellant. The thermal energy is converted to kinetic energy as the propellant expands to high velocities in the converging-diverging nozzle.

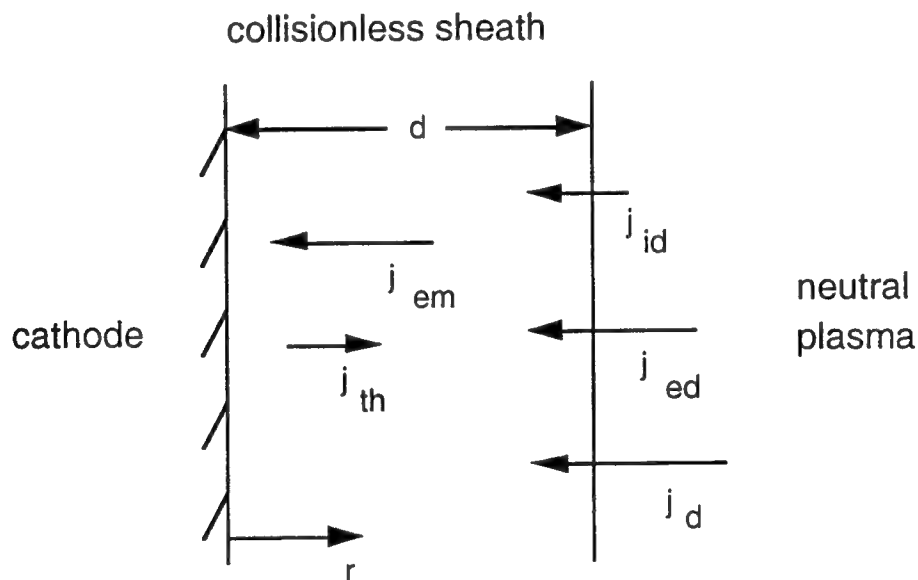
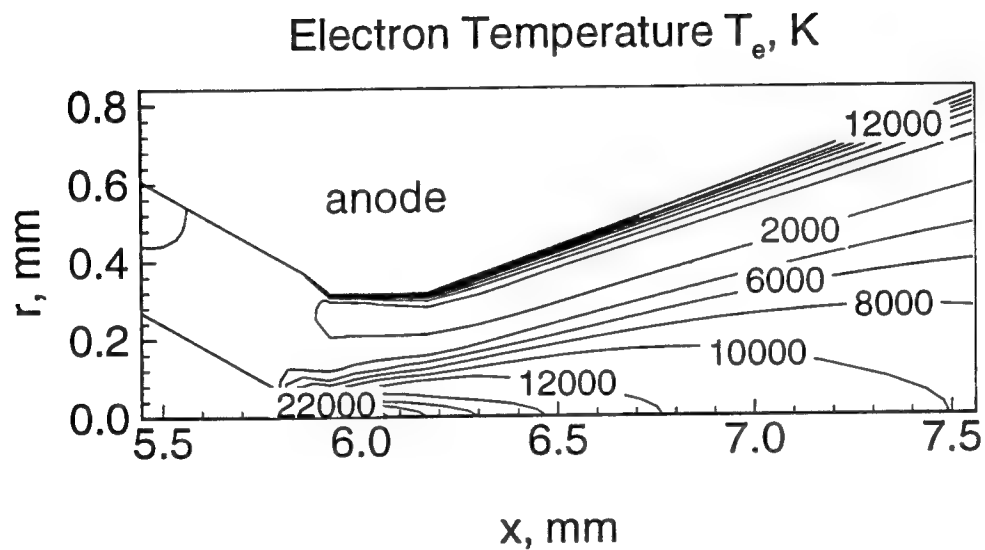


Fig. 2 One dimensional collisionless sheath model.



¹**Fig. 3** Electron temperature T_e contours in the constrictor region of a 1 kW arcjet operating at 10 A, 50mg/sec. The exit plane is located at $x = 18.4$ mm.

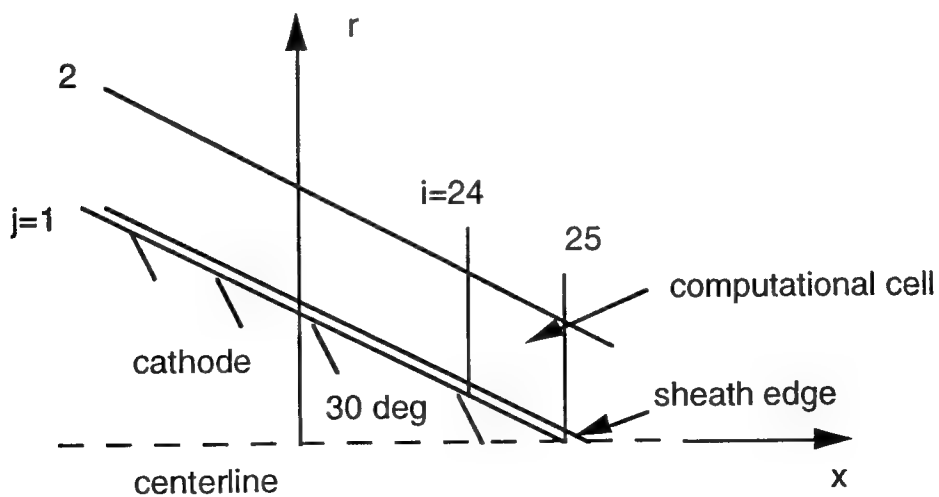


Fig. 4 The sheath edge and the near-cathode computational grid.

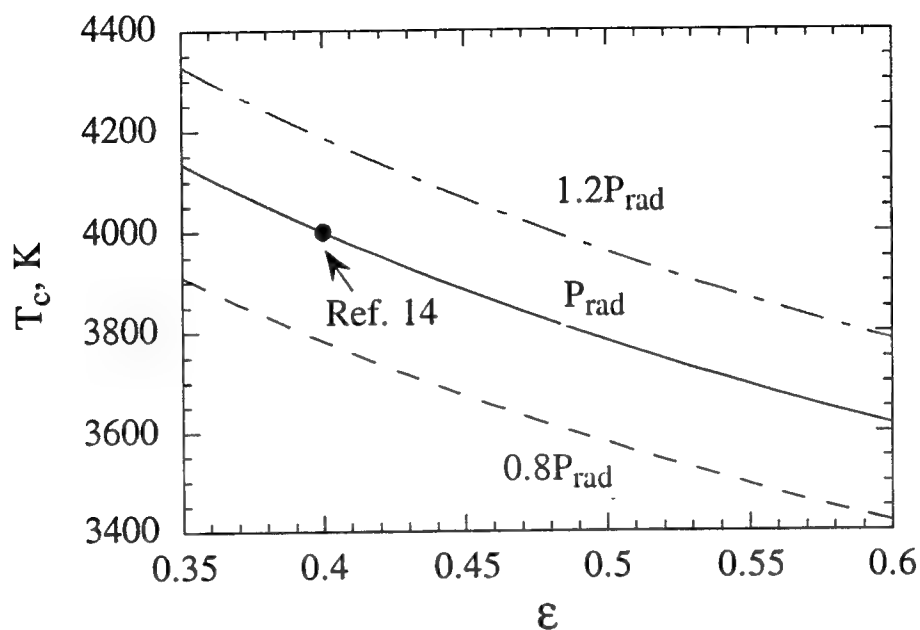


Fig. 5 Arcjet cathode temperature as a function of tungsten emissivity, assuming constant radiative power from the cathode with $P_{rad} = 5.81 \times 10^6$ Watts/m².

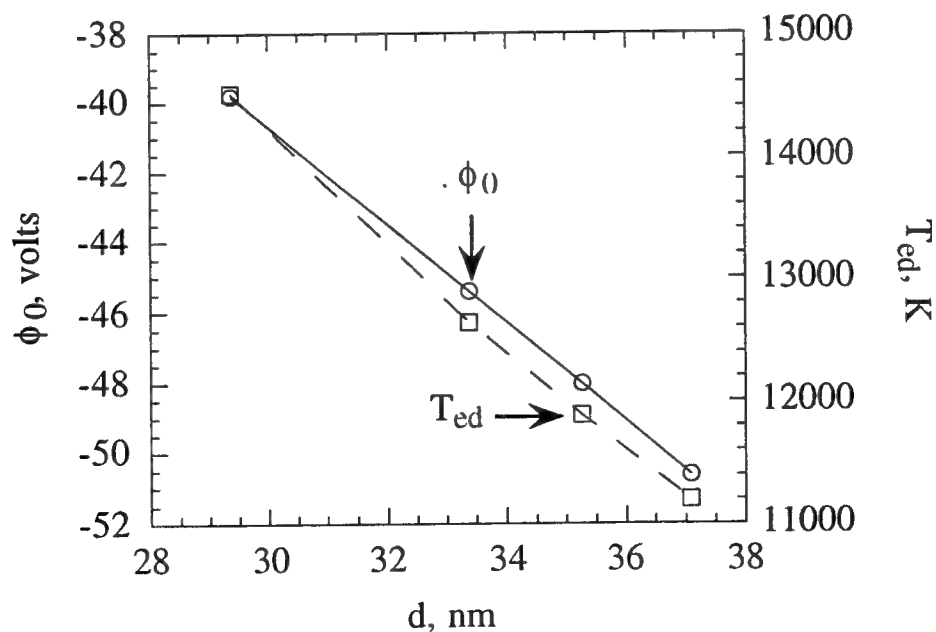


Fig. 6 Sheath potential and the sheath edge electron temperature at various sheath thickness for the nominal case with variable δ . The solution matching occurs at $\phi_0 = -50$ volts, $d = 37$ nm, and $T_{ed} = 11320$ K.

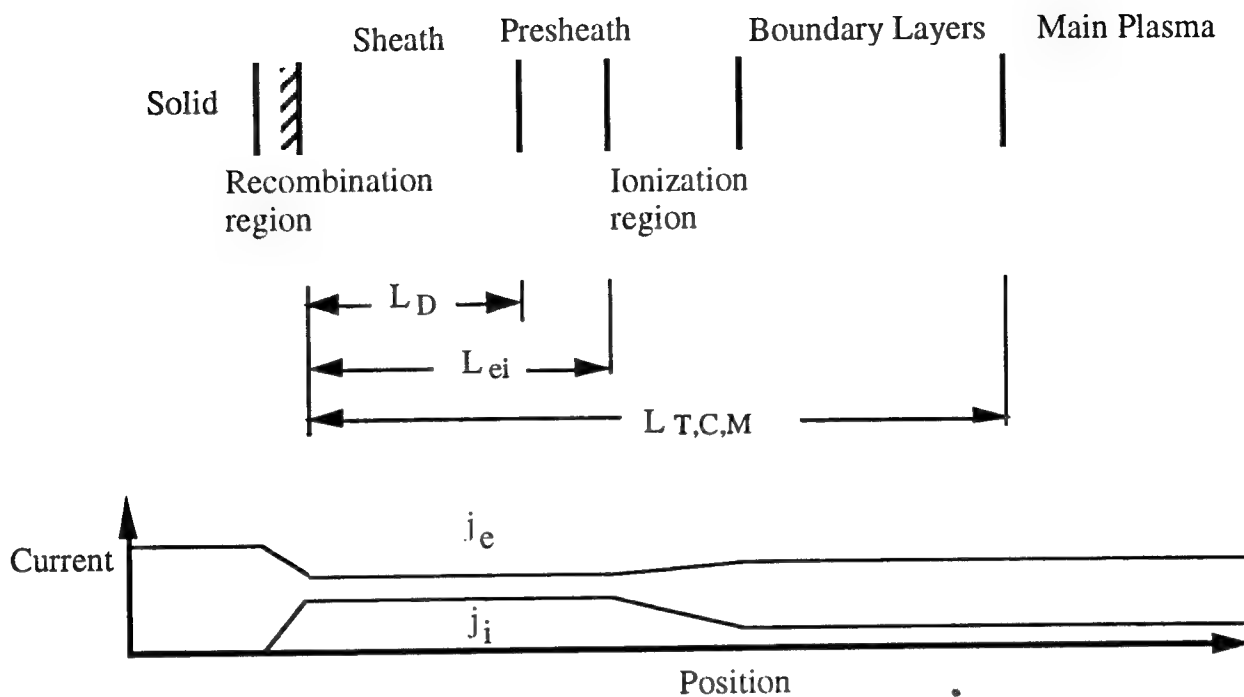


Fig. 7 Near-cathode plasma regions for the Goodfellow model.

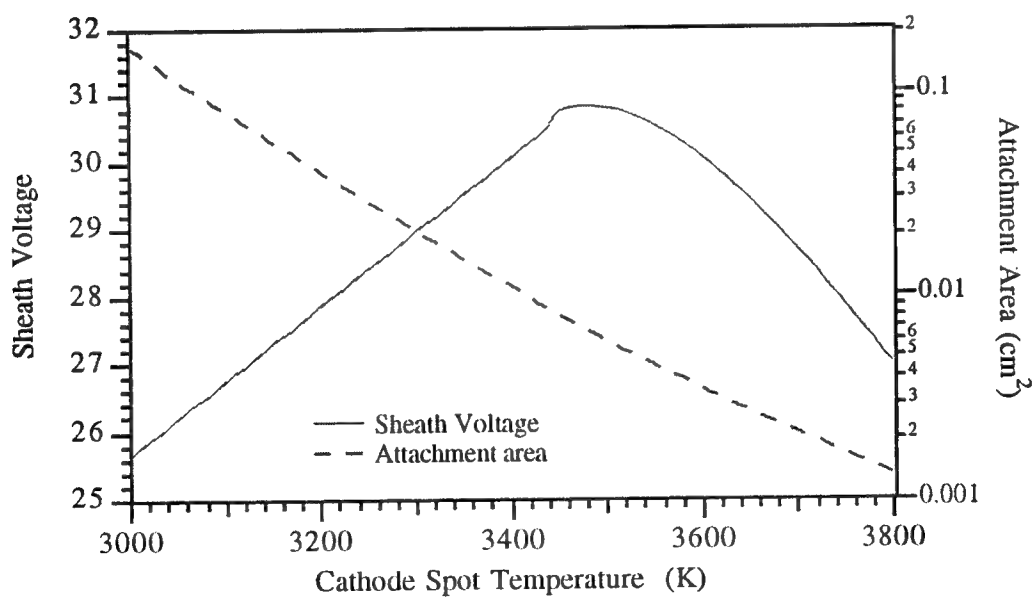


Fig. 8 Sheath Voltage and attachment area as a function of cathode temperature, Goodfellow model.

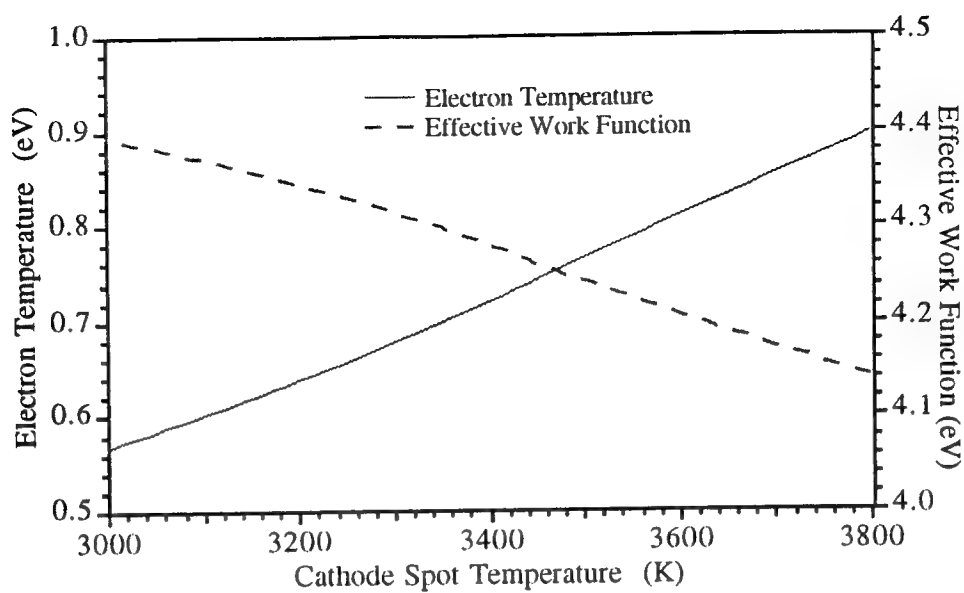


Fig. 9 Electron temperature and effective work function as a function of cathode temperature.

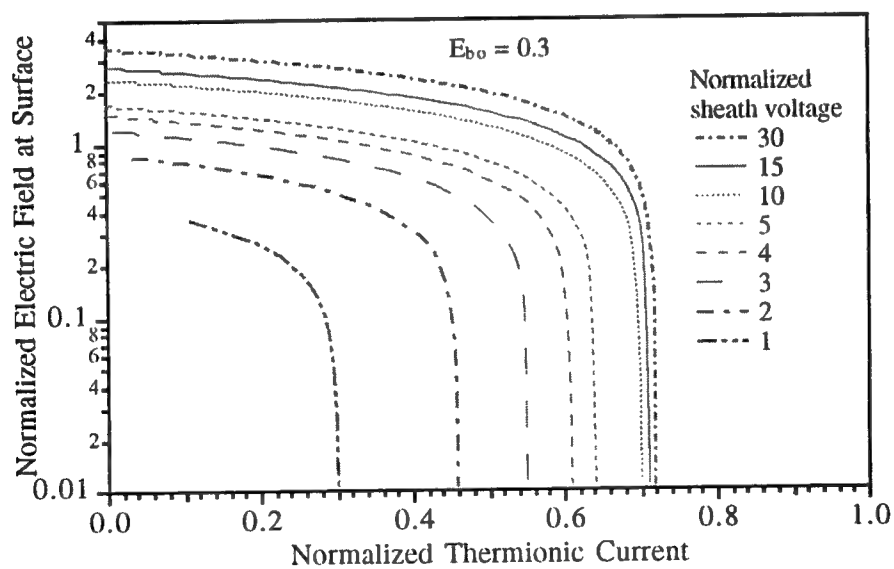


Fig. 10 Normalized electric field as a function of normalized thermionic current density.

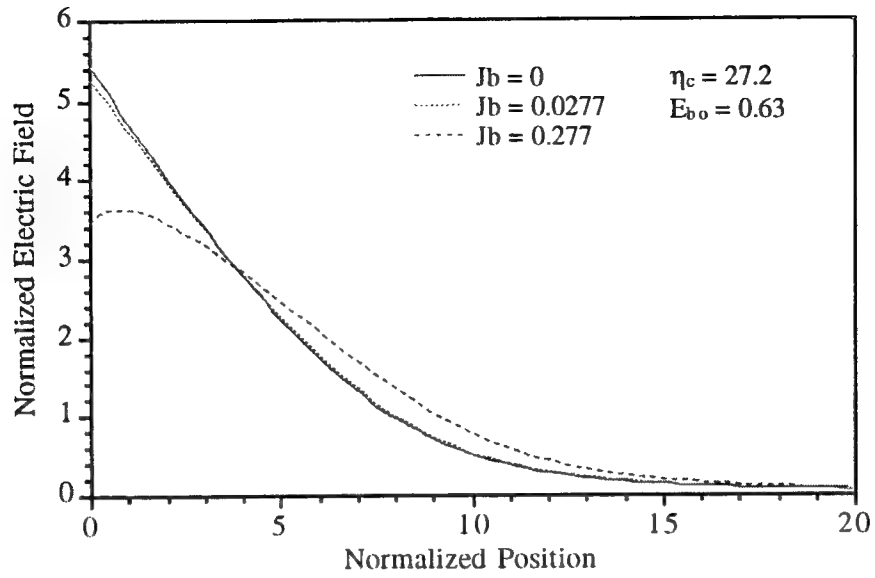


Fig. 11 Normalized electric field as a function of normalized position with normalized thermionic current density as a parameter.

ARCJET ANODE PLASMA MEASUREMENTS USING ELECTROSTATIC PROBES

Nicholas T. Tiliakos*, Rodney L. Burton†, and Herman Krier††
University of Illinois at Urbana-Champaign
Urbana, IL 61801

Abstract

A 1 kW hydrazine arcjet thruster has been modified for internal probing of the anode sheath boundary layer with an array of fourteen electrostatic micro-probes flush-mounted into the anode body. Axial and azimuthal distributions of the plasma properties floating potential, anode sheath potential, wall current density, electron number density and electron temperature have been obtained for arc currents between 7.8 and 10.6 A and propellant flow rates of 40 to 60 mg/s. P/\dot{m} ranged from 18.8 to 27.4 MJ/kg. Azimuthal symmetry has been verified for all arcjet operating conditions. The electron temperature data show that the near-anode plasma is highly non-equilibrium. Most of the current density and anode heating is located within 2-4 mm of the constrictor exit, with the location affected more by mass flow rate than by arc current. The anode heating distribution is closely coupled to current density and accounts for ~18-24% of the total input power. Reasonable agreement between a numerical model and the experimental results is found for a constant value of the electron inelastic energy loss factor.

*Scientist, GASL, Inc., Ronkonkoma, N. Y. 11779-6648; Member, AIAA.

†Professor, Department of Aeronautical and Astronautical Engineering, Associate Fellow, AIAA.

††Professor, Department of Mechanical and Industrial Engineering, Fellow, AIAA.

Nomenclature

A_p	Geometric probe collection area [m^2]
A_{eff}	Effective probe collection area [m^2]
e	Electronic charge [Coulomb]
E	Near-anode electric field [V/mm]
E_{pl}	Electric field in bulk plasma [V/mm]
I_p	Total probe current [mA]
I_{e-sat}	Electron saturation current [mA]
I	Applied current to arcjet [A]
j	Current density [A/cm^2]
j_a	Anode current density, [A/cm^2]
j_{th}	Thermal current density [A/cm^2]
k	Boltzmann constant [$J/^{\circ}K$]
L	Nozzle axial length [mm]
\dot{m}	Propellant mass flow rate [mg/sec]
m_e	Electron mass [kg]
M_i	Reduced N^+ and H^+ mass [kg]
n_{es}	Electron number density [m^{-3}]
n_r	Number density of species r [m^{-3}]
q_e	Anode heating by electrons [W/cm^2]
r_p	Probe radius [mm]
T	Temperature [$^{\circ}K$]
V	Voltage [V]
W	Anode tungsten material work function [eV]

Greek Symbols

ε_i	Ionization potential, [eV]
-----------------	----------------------------

λ_D	Debye length [mm]
λ_{rs}	Mean free path [mm]
λ_s	Sheath thickness [μm]
ϕ	Potential [V]
Subscripts	
arc	Arcjet
a	Anode
e,i	Electron/ion
f	Floating
gas	Plasma-gas flow
p	Probe
s	Pre-sheath/plasma edge.

I. Introduction

There is now a well-developed acceptance of electric propulsion on spacecraft to increase mission capabilities and lower launch costs. Electrothermal arcjet thrusters have matured to the point where they are more than competitive with chemical propulsion systems for satellite stationkeeping, maneuvering and orbital transfer. Development in this field has been driven by the current boom in the global satellite telecommunications industries.

Future space mission scenarios require an increase in the performance of space propulsion systems, in particular arcjet thrusters. To improve arcjet performance, it is desirable to understand the internal flow-field physics through experimentally-validated numerical models.

This paper describes research conducted to improve the understanding of arc attachment and anode heating processes in the boundary layer of a 1 kW arcjet thruster operating on simulated hydrazine ($N_2 + 2H_2$) propellant.¹ An experimental investigation of an arcjet anode plasma boundary layer was performed with electrostatic micro-probes, a type of Langmuir probe. A standard 1 kW arcjet design² was modified to accommodate fourteen micro-probes in the anode body, permitting analysis of anode heat transfer and validation of a numerical model.³ Two main parameters were varied: arcjet operating current from 7.8 to 10.6 A and $N_2 + 2H_2$ propellant flow rate from 40 to 60 mg/s.

Langmuir probes have been employed for plasma diagnostics since the early 1920's, when the method was first developed and implemented.⁴ The probe is a wire or sphere inserted into a plasma, biased positive or negative to collect charged particles. The resulting plot of probe current I_p versus probe voltage V_p yields information on plasma properties. Electrostatic probes have been used as an anode sheath diagnostic^{5,6} and in electric thruster plumes.⁷⁻¹¹ They have also been used in supersonic and hypersonic flows.^{12,13} The utility of electrostatic probes is not limited to cylindrical and spherical geometries only. Flush-mounted probes have been used for analyzing the properties in hypersonic flowfields.¹⁴⁻¹⁸

The first experimental investigations of the nozzle region of a low power arcjet consisted of emission spectroscopy of the plasma flow inside the nozzle of a 1 kW hydrazine arcjet.¹⁹ Additional investigations of plasma conditions inside the nozzle and constrictor have been performed on low and medium power arcjets.²⁰⁻²¹ Other internal diagnostics work includes internal emission spectroscopy measurements in the nozzle expansion region of a 26 kW ammonia arcjet.²²

Curran *et al.* studied arc energy deposition in the segmented anode of a 1-2 kW arcjet, the distribution of the arc attachment, and its effects on the performance characteristics of the device.²³ The current to five anode segments, separated with boron nitride spacers, was individually measured along with floating potential and anode fall voltage. Current was found to attach diffusely to the nozzle wall, with more than 50% in the diverging section of the nozzle. The current attachment distribution down the nozzle was found to be dependent on the mass flow rate, with the highest current density near the constrictor, consistent with previous results for electron number density.¹⁸

Determination of near-anode plasma properties aids in determining the transition between diffuse and constricted modes of arc attachment.²⁴ Operation of an arcjet in a constricted mode leads to high anode heating at the attachment point,²⁵ eventually limiting the electrode lifetime and decreasing thruster performance.²⁶ Knowledge of the current density distribution on the anode also aids in the validation of numerical models, as these models have had difficulty simulating the anode boundary layer region. It was a goal of this work to provide data for model validation to aid in the design of advanced high performance arcjet thrusters.

II. Experimental Approach

For this study a thruster was fabricated with similar dimensions to a standard 1 kW arcjet thruster,² and modified to accept electrostatic probes. The thruster was operated at a simulated hydrazine flow rate of 40-60 mg/s, with a nominal current of 10 amps, and 110 volts across the electrodes. The specific power P/\dot{m} ranged from 18.8 to 27.4 MJ/kg. The converging cone half angle upstream of the constrictor

was 30°, while the diverging section half angle was 20°. The constrictor diameter of 0.63 mm and length 0.25 mm were kept identical to the standard arcjet, as was the axial cathode gap of 0.60 mm \pm 0.13 mm. The exit plane diameter was 9.5 mm, providing an area ratio of 225:1.

The arcjet nozzle (anode) was fabricated from 2% thoriated tungsten. The cathode was also fabricated from 2% thoriated tungsten and had a 30° half-angle tip, with a diameter of 4.8 mm at the thruster head.

The major difference from the standard design was elimination of an anode insert and associated seal² and implementation of a single-piece thruster body. Use of a monolithic body facilitated modeling of the anode heat transfer, as well as placement of the array of fourteen electrostatic micro-probes at various axial and azimuthal locations in the anode wall (Fig. 1).

The probes were numbered to designate the axial distance (mm) from the constrictor exit. Probes 1, 4, 7, and 10 and probes 1', 4', 7' and 10' were at the same axial location, but separated azimuthally 180° (Fig. 1). The remaining probes were located at 120° and 240° to provide information on current symmetry.

Micro-probes 2-10' were made from 0.43 mm diameter, 99.95% pure tungsten wire, surrounded by an alumina (Al_2O_3) insulator tubing with an outer diameter of 0.86 mm and inner diameter of 0.51 mm, inserted into a Type 304 stainless steel tube, with an inner diameter of 1.22 mm. For probes 1 and 1', 0.17 mm diameter tungsten wire was used, surrounded by an Al_2O_3 tube with an outer diameter of 0.58 mm and inner diameter of 0.20 mm and inserted into a Type 304 stainless steel tube with an inner diameter of 0.81 mm.

To summarize, fourteen micro-probes were located in the anode housing at 10 axial and 4 azimuthal locations downstream of the constrictor. The tungsten probe wire and alumina tubing were held in place with high temperature (4000 °F) zirconia adhesive. The wire probe tip could be extended into the plasma flow at various distances from the tubing end (Fig. 2). Tungsten was selected for the probe material because of its high melting point, 3680 °K, and high work function,²⁷ 4.55 eV, giving low electron emission. Further details regarding probe fabrication techniques are discussed in Ref. 1.

After each test, all probes were removed from the anode for inspection and re-measurement of their diameter. Data from visibly contaminated or eroded probes was not included in the analysis. The probes were then abrasively cleaned and re-used.

The thruster was mounted inside a 1.5 m³ vacuum tank, with a background pressure range of 0.1 - 0.2 Torr for flow rates between 40-60 mg/sec. The N₂ + 2H₂ propellant flow rate is controlled by two Unit Instruments mass flow controllers. A radiation-shielded chromel-alumel type K thermocouple recorded nozzle surface temperature at 9.4 mm from the exit plane.

The plasma properties of floating potential, sheath potential, electron density and temperature at the sheath edge, and anode current density were derived from the probe V-I characteristic,¹ obtained by biasing the probe with a sinusoidal function generator and measuring the probe current I_p with a 103.7 Ω current sensing shunt resistor. The function generator frequency was 10 Hz to avoid distortion in the probe V-I characteristic, as well as unwanted voltage drops across the low inductance current sensing resistor.

Probe Length Scales

The magnitude of the current to a biased probe depends on the sheath thickness and elastic and inelastic collisions in the sheath, and on the probe surface conditions; e.g. contamination, thermionic emission, and sputtering. Interpretation of the probe characteristic depends on the collisionality of the probe sheath. For no collisions in the sheath, obtaining n_{es} and T_{es} from the characteristic is relatively straightforward and the Laframboise method²⁸ can be used to estimate the ion current I_i at all voltages up to the plasma potential ϕ_{pl} , providing a convenient analytical approach to the data analysis.

If sheath collisionality is significant, an analytical approach may not be readily available. Sheath collisionality is assessed by comparing the Debye length λ_D , probe radius r_p and charged particle mean free paths, λ_{rs} . The sheath thickness λ_s is also compared with λ_{rs} and r_p .¹

To calculate the sheath length scales, a numerical arcjet model³ was used to obtain values for $n_{H^+}, n_H, n_{H_2}, n_{N^+}, n_N, n_{N_2}$ for the nominal conditions of $\dot{m} = 50$ mg/sec and $I_{arc} = 10$ A. These values were used to calculate Debye length and mean free paths at each probe location, for 31 collisional reactions.¹ The mean free paths for the 31 separate collisional reactions were calculated using the cross-sectional data used in the numerical model.³

For the sheath to be termed "thin" $r_p/\lambda_D \gg 1$, and for the sheath to be collisionless, $\lambda_{rs} \gg \lambda_s$. For ion collection, probes 1-4' are found to be highly collisional and probes 5-10' are moderately collisional. For electron collection all the

probe sheaths are relatively collisionless. For both ion and electron collection the probe sheath is thin.¹

Probe Collection Area

Whether the probes are flush-mounted or extended partially into the flow, determining their geometric area is complicated if the alumina tubing is damaged, exposing an additional collection area. Damage to the alumina probe sheath was almost exclusively confined to probes 1, 1' and 2, located in the region of maximum current density. The damage was characterized by cracking or vaporization of the Al_2O_3 tubing caused by intense heating and thermal stresses, which exposed more probe surface to the plasma flow, adding to the uncertainty in the probe area calculation. When damage occurred, probe area was calculated by averaging the pre-test and post-test A_p values. The post-test geometric probe area was given as:¹

$$A_{\text{post-test}} = \pi D_p^2 / 4 + \pi D_p c \bar{L} \quad (1)$$

where: D_p is the probe diameter, c is the fraction of Al_2O_3 tip cracked, and \bar{L} is an average probe exposure length due to the Al_2O_3 cracking. The values for D_p , c and \bar{L} are based on post-test visual observations of each probe with a magnifying lens.

The sheath surrounding the probe creates an effective collection area A_{eff} which is somewhat larger than the geometrical probe collection area A_p . Accounting for the sheath is particularly important if the probe bias is high, in which case the probe sheath may extend far enough into the boundary layer that convection effects must be included in the analysis of the probe characteristic.^{1, 29}

When λ_s is comparable to the probe dimensions, the sheath is termed thick and the probe effective collection area is appreciably larger than the physical area of

the probe. Based on calculations of the sheath thickness for all fourteen probes,¹ the sheath effect increased the probe collection area by a maximum of 10%.

Probe Damage and Contamination

Contamination of the probe surface can severely distort the probe V-I characteristic, leading to erroneous results in j_a , T_{es} and n_{es} .³⁰ If the probes are clean then the current for probes at the same axial location should be equal. However, the signal from a contaminated probe is much less than from a clean probe, and a contaminated probe has an altered characteristic slope, resulting in a spuriously high T_{es} measurement.

Once a probe was contaminated *in situ* it was very difficult to clean and was replaced. The greatest chances for probe contamination to occur were within the first 1-2 minutes of arcjet start-up before attaining a steady arcjet operating voltage, and when the probes collected too much current during cleaning, causing melting of the Al_2O_3 tip.

In this work, the probes were maintained in a clean state using a pulsed ion bombardment technique, in which the probes were sequentially cleaned with 1-2 square-wave pulses of negative 160 volts amplitude, with a duration of about 0.15 sec. The cleaning efficiency was found to be relatively insensitive to the probe cleaning voltage, the cleaning pulse duration time, the number of cleaning pulses and the probe diameter.¹

Typical Probe V-I Characteristic

A typical probe V-I characteristic is shown in Fig. 3. The floating potential ϕ_f , plasma potential ϕ_{pl} , ion and electron saturation regions and electron-retarding

regions are shown. The slope in this latter region provides a measure of the electron temperature T_{es} at the pre-sheath/plasma edge.³¹ The electron number density is derived from knowing the probe current at ϕ_{pl} , T_{es} and A_p .³¹

III. Experimental Results

Table I summarizes the steady state thruster operating conditions using flush probes. Results with probes extended up to 0.3 mm into the flow were similar to those of the flush probes.¹

Table I. Summary of steady state arcjet thruster operating conditions.

Operating Condition	\dot{m} (mg/sec)	Avg. I_{arc} (Amps)	Avg. V_{arc} (Volts)	Power (Watts)	P/\dot{m} (MJ/kg)	T_a (°K)
a	40	10.6	104	1102	27.4	945
b	45	9.8	109	1068	23.6	935
c	50	7.8	121	944	18.8	870
d	50	8.9	115	1023	20.6	900
e	50	9.8	112	1098	22.0	910
f	60	9.9	121	1198	20.0	895

Floating Potential Distribution

Figure 4 presents the measured floating potential distributions along the anode wall for four operating conditions. It was observed that regardless of these conditions, the floating potential data for the 120° and 240° probes lie on the same curve as the 0° and 180° probes, implying azimuthal symmetry.

As the propellant flow rate increases, i.e. P/\dot{m} decreases for fixed I_{arc} , the floating potential becomes more negative, with azimuthal symmetry at all conditions. At all flow rates studied there is an absolute maximum in floating potential between 2 and 3 mm; for $x > 3$ mm, ϕ_f monotonically approaches zero volts. This result is consistent with high T_{es} between 2 and 3 mm, so that a larger probe potential is required to maintain $j_p = 0$ for a floating probe. Likewise, as the plasma flow expands through the nozzle, the electron temperature decreases, so that a smaller ϕ_f is required.

Keeping \dot{m} constant and varying I_{arc} from 7.8 to 10.6 A produces very little effect on the ϕ_f distribution. The observed variation is within the experimental error of ± 1 V except for a variation of ± 2.5 V at $x = 2$ mm.

Anode Sheath Potential Distribution

The anode sheath potential ϕ_s is also derived from the probe V-I characteristic, and is the negative of the plasma potential ϕ_{pl} ,³² where ϕ_{pl} is determined by the intersection of the electron-retarding and electron saturation regions of the V-I curve (Fig. 3).

An expression can be written for anode sheath potential which provides an estimate of the electron temperature:^{1,33}

$$\phi_s = -\phi_f + \frac{kT_{es}}{e} \left\{ \ln(\alpha_c) + \ln \left(0.61 \sqrt{\frac{2\pi m_e}{M_i}} \right) \right\} \quad (2)$$

$$\text{where } \alpha_c \equiv \left[1 + \frac{\pi \lambda_D}{2 \lambda_{H^+ - H_2}} \right]^{-1/2}$$

The effect of propellant flow rate on the anode sheath potential distribution is shown in Fig. 5. As the propellant flow rate is increased from 40 mg/sec to 60 mg/sec, ϕ_s increases at all probe locations and the maximum in the ϕ_s axial profile distribution shifts from probe 2 to probe 3.

For flow rates of 40 to 50 mg/sec an absolute maximum exists in the sheath potential at about $x = 2$ mm, similar to the ϕ_f data. In all cases, ϕ_s decreases monotonically for $x \geq 2$ mm. Throughout the anode boundary layer $\phi_s > 0$, so that the anode sheath is always electron-attracting.

Current Density Distribution

The current density j_a is evaluated by averaging the digital samples of probe current over a range of ± 0.1 V centered at zero probe volts. Figure 6 shows the current density for 45, 50, and 60 mg/sec at 9.8 A, and for 40 mg/sec at 10.6 A.

- (1) The current density j_a decreases monotonically with x , except for 60 mg/s and 9.8 A, where j_a peaked at 3 mm.
- (2) As the propellant flow rate was increased from 40 mg/ to 60 mg/sec, the location of peak current density shifts from $x = 2$ to $x = 3$ mm.
- (3) For $\dot{m} = 40, 45$, and 50 mg/sec the current density was maximum at 1 mm. The current density decreases from 38 ± 11.5 A/cm² near the constrictor to $\sim 3.0 \pm 0.6$ A/cm² at 10 mm.
- (4) For most of the experimental conditions studied, azimuthal current symmetry is inferred from the j_a data obtained, within experimental error. The exception is a significant discrepancy between probes 1 and 1'.

At 40 mg/s, probe 1 gave a current density 5 times larger than 1'. Percent discrepancy decreased from 42% at 45 mg/sec to 36% at 50 mg/sec and to 24% at 60 mg/sec. Some of this uncertainty is ascribed to the uncertainty in the probe collection area, [O~(15-35%)] as these probes adjacent to the constrictor experienced the highest thermal stresses, damaging the alumina insulator.

(5) The most significant change in the current density distribution occurred for 60 mg/s, for which the current density peak shifted downstream to $x = 3$ mm. At lower propellant flow rates maximum current density was fixed at $x = 1$ mm. Based on the \dot{m} and I_{arc} parameter studies it appears that \dot{m} affects the j_a distribution more than I_{arc} with regards to the location of maximum current density.

A weighted anode sheath potential is calculated as:

$$\bar{\phi}_s = \frac{\int_0^L j_a(x) \phi_s(x) dA(x)}{I_{arc}} \quad (3)$$

where x is in mm, $j_a(x)$ is the current density distribution and $\phi_s(x)$ is the anode sheath potential distribution. For the $j_a(x)$ and $\phi_s(x)$ distributions the values for the 0° and 180° probes are averaged to obtain a single data point in Eq. (3).

The weighted anode sheath potential as a function of propellant flow rate exhibits a minimum at 50 mg/s and 9.9 A, increasing for $\dot{m} \geq 50$ mg/s. The largest value for $\bar{\phi}_s$, 17 ± 5.1 V, occurs at 60 mg/s and P/\dot{m} of 19.9 MJ/kg. Similarly, for 40 mg/s and 27.4 MJ/kg, $\bar{\phi}_s$ has a low value of 8.1 ± 1.6 V. The results agree in general with Curran et al.,²³ who found that the anode fall voltage was O(10-20V).

Electron Number Density

Figure 7 presents the electron number density results for 60, 50 and 45 mg/sec at 9.8 A, and 40 mg/s at 10.6 A. For all flow rates studied, the electron number density n_{es} , which ranges from $\sim 10^{18}$ - 10^{19} m^{-3} , was largest at 1 mm with a secondary peak at 4 mm, and decreased down the nozzle. For all cases, the axial variation of n_{es} varied from $3.5\text{-}10 \times 10^{18} \text{ m}^{-3}$ at 1 mm, to $7\text{-}10 \times 10^{17} \text{ m}^{-3}$ at 10 mm.

Symmetry in the n_{es} data is reasonable for all flow rates except 45 mg/sec, where the largest n_{es} difference between the 0° and 180° probes was 60%, for probes 1 and 1' only. This corresponds to the symmetry observed earlier for the j_a data at the same conditions.

In the region of attachment of 2 - 4 mm, n_{es} increases with increasing P/\dot{m} and fixed I_{arc} ; as P/\dot{m} increases 38% n_{es} increases by 74%. For $x > 5$ mm, increasing P/\dot{m} does not have as large an effect on the n_{es} distribution.

Electron Temperature

The electron temperature T_{es} at the pre-sheath/plasma edge, coupled with the ϕ_s and j_a results, is needed to estimate the anode heating q_e . In addition, T_{es} allows calculation of scalar electrical conductivity σ and thermal conductivity κ in the anode boundary layer.

The T_{es} distribution is derived from the classical V-I characteristic method, using the inverse slope of the electron-retarding region. However, as shown below, different test results were obtained from the sheath potentials (Eq. 2).

Electron temperatures derived from the V-I slope method are plotted in Fig. 12 for 3 values of mass flow rate at 9.8 A. For all mass flow rates T_{es} was highest from 1-3 mm, at $30,000 \pm 5,000$ K, falling to $16,000 \pm 4,000$ K further from the constrictor.

The symmetry in the T_{es} data for the 0° and 180° probes at 1, 4, 7 and 10 mm is reasonably good, especially at 50 and 60 mg/s. For 45 mg/s the T_{es} data for probes 1, 1' and probes 7, 7' differ by about 32%.

For all propellant flow rates tested, the ratio T_{es}/T_g is much greater than unity in the near-anode region, at all probe locations. For a gas temperature of 1400 K, slightly above that of the anode wall, $T_{es}/T_g \sim O(10-20)$. This value for the gas temperature is reasonable since nozzle surface temperature measurements yield $T_{noz} \sim 950$ K and the numerical model predicts $T_{gas} \sim 1200$ K along the anode wall. This strongly suggests that a nonequilibrium two-temperature plasma exists in the near anode region of the arcjet.

Anode Heating

The anode energy deposition q_e is mainly due to the electron energy transferred from the arc to the anode, via the current attachment. The electron energy deposition in the anode sheath was studied as a function of propellant flow rate \dot{m} , arcjet operating current I_{arc} and specific power P/\dot{m} .

The energy deposition into the anode for an electron-attracting sheath is calculated from:^{1,34}

$$q_e = j_a [5kT_{es} / 2e + \phi_s + W] \quad (5)$$

where the first term in brackets represents the thermal energy of the electrons, the second term is the electron energy gained in traversing the sheath and the last term is the energy gained when the electron recombines with the anode surface. The work function W of the 2% thoriated tungsten anode is 3.7 eV, an average value between that for 2% thoriated and pure tungsten.²⁷ The plasma properties j_a , n_{es} , and T_{es} vary with propellant flow rate, arcjet operating current and specific energy, affecting anode heating through Eq. 5.

It was stated above that the location of maximum j_a was more sensitive to the mass flow rate than to the arcjet operating current. The effects of propellant flow rate on anode heating are shown in Fig. 8 for $I_{arc} = 9.8A$, $\dot{m} = 45, 50$ and 60 mg/s and 40 mg/s and $I_{arc} = 10.6$ A, using flush-mounted probes.

There is a minimal difference in the q_e distribution for 40, 45 and 50 mg/s. Results for these flow rates show a peak in q_e at 1 mm, with a minor secondary peak at $x = 4$ mm, similar to the j_a distribution. As with the j_a results, when \dot{m} is increased to 60 mg/s, $(q_e)_{max}$ is displaced downstream to 3 mm, again coinciding with $(j_a)_{max}$. Thus, the peak in anode heating is a function of the current density and both are dependent more on the propellant flow rate than on I_{arc} . For 45 mg/s the anode heating varies from approximately 480 W/cm² at 1 mm to 41 W/cm² at 10 mm. Similarly, for 50 mg/s, q_e varies from 440 ± 140 W/cm² at 1 mm to ± 8 W/cm² at 10 mm.

The q_e distribution for the highest specific power tested, 27.4 MJ/kg (40 mg/s, 10.6 A) gave a heat flux of 1420 ± 600 W/cm² at 1 mm, the largest value obtained for all flow rates tested. This coincides with the largest current density obtained, 140 ± 57 A/cm² at $x = 1$ mm, for the same operating conditions. For all propellant flow rates

studied, $q_e(x)$ monotonically decreases after $(q_e)_{\max}$, a trend also observed in the current density distribution.

The total electron energy power deposition to the anode Q_a is written for an electron-attracting sheath as:

$$Q_a \equiv \int_0^L \bar{q}_e(x) dA(x) = \int_0^L j_a \left[\frac{5kT_{es}}{2e} + \phi_s + W \right] dA(x) \quad (6)$$

where $dA(x) = 2\pi r(x)(\cos 20^\circ)^{-1} dx$. For the 0° and 180° probes an average value is used for $q_e(x)$ at $x = 1, 4, 7$ and 10 mm.

Using measured values, the electron energy deposition in the anode ranged from 18-24% of total arcjet power, for 18.8 MJ/kg to 27.4 MJ/kg. These fractional energy values agree well with previous results in experiments with a water-cooled arcjet simulator,³⁵ for which the percentage of the total power lost to the anode was 20-25 % of the total input power.

For a fixed 50 mg/s, Q_a was a maximum of 229 ± 49 W (22% of input arc power) at $I_{\text{arc}} = 8.9$ A, then decreased to 197 ± 42 W (18% of arc power) as I_{arc} was increased to 9.8 A. For increasing flow rate at fixed current, Q_a varied from 18% of the total input power for 50 mg/s and 9.8 A to 287 ± 60 W (24% of arc power) for 60 mg/s and 9.9 A. Thus, the maximum anode heating occurred for the highest propellant flow rate, indicating that when operating the arcjet at low specific power, a larger fraction of the total input power is absorbed into the anode.

Plasma Properties

Once the electron temperature and number density distributions are known, plasma transport properties such as scalar electrical conductivity can be calculated along the anode. The degree of ionization α for this multi-species plasma is defined as:

$$\alpha_{\text{ioniz}} \equiv \frac{n_e}{n_{\text{H}_2} + n_{\text{N}_2} + n_{\text{H}} + n_{\text{N}}} \approx \frac{n_e}{n_{\text{H}_2} + n_{\text{N}_2}} \quad (5)$$

For 50 mg/s and 9.8 A, based on the measured n_e and predicted n_{H_2} and n_{N_2} from a numerical model,³ α_{ioniz} varies from 7×10^{-6} at 1 mm to 3×10^{-5} at 5 mm to 8×10^{-5} at 10 mm. In this range of α_{ioniz} the electrical conductivity is dominated by electron-neutral collisions.

Comparison With Previous Experiments

The only previous published current density measurements in a low power hydrazine arcjet were by Curran et. al.²³ The main findings were that the total current had minimal effect on the measured current distribution, the propellant flow rate had a strong effect on the current distribution, the anode fall was found to be between 10-20 V, and for $\dot{m} = 49.7$ mg/sec and 10 A, approximately half of the total operating arcjet current was collected on the segment closest to the nozzle exit, within 5 mm of the exit plane. Because of the segmented geometry, no conclusions could be reached with respect to symmetry and anode heating.

The results of this work generally agree with these findings. Figure 9 shows a comparison between the flush probe current density data for 50 mg/sec and 9.8 A, $V_{\text{arc}} = 112$ V and the data of Ref. 23, for 49.7 mg/sec, 10 A and 134 V. The experimental data in Fig. 9 compare reasonably well, even with a 16% difference in arcjet operating voltage and an 18% difference in P/m. The largest difference between the two experiments occurs at 1 mm and in the anode region at 5 to 8 mm. At 1 mm, Ref. 23 data lies between the results of probes 1 and 1', though much closer to probe 1'. For 5 to 8 mm the Ref. 23 current density measurements give 2.9 A/cm², compared to 7-9 A/cm² measured here. Both sets of data display a maximum current density at 1 mm, with a smaller secondary peak at 4 mm.

Comparison with Numerical Model

An important recent advance has been the simulation of arcjet physics with multifluid nonequilibrium models.^{3,36} The MKB model of Megli, et al.³ employed here provides a self-consistent approach to solving Ohm's Law and the particle energy equations, which are coupled to the equations of chemical nonequilibrium kinetics, the Navier-Stokes equations and Maxwell's equations with appropriate boundary conditions. The model assumes steady-state, laminar flow, and includes injection flow swirl and anode heat transfer in a converging-diverging nozzle geometry with variable cathode arc gap. It also includes a variable nozzle geometry, a variable mixture of nitrogen and hydrogen, and accounts for the chemical kinetics of seven species: H₂, N₂, H, N, H⁺, N⁺ and e⁻.

The model's electron energy equation accounts for inelastic losses to molecular internal energy modes, i.e. rotational, vibrational, excitational, and ionization, through multiplying the electron-molecule collision frequencies by an energy loss

factor, δ . The δ factor is strongly dependent on the collision partner and T_e , and weakly on T_g .³

Large uncertainties are found in the literature for δ of various molecules.^{3,37} The selection of a proper energy loss factor strongly affects the model arc attachment location, and the electron temperature and density populations near the anode wall.

The model results were compared with experimental flush probe current density data for the nominal arcjet conditions of 50 mg/s and 9.8 A. Numerical results for a variable locally-adjusted variable δ , $\delta = 1200$, and $\delta = 3000$ are shown in Fig. 10. There is reasonably close agreement between experimental results and the $\delta = 1200$ and 3000 cases. The $\delta = 1200$ case provides better agreement than $\delta = 3000$ within 2 mm of the constrictor exit, where the axial current density gradient is largest. Agreement between the experiment and the variable δ model is poor.

These results imply that an accurate accounting of inelastic energy losses in the anode sheath layer is important for realistic simulation of current attachment. The best agreement in the arc attachment zone, 2 - 6 mm, is obtained with $\delta = 1200$ or 3000. A better fit to the experimental data is obtained at probes 1 and 1' using $\delta = 1200$. Obtaining good agreement between the model and the experimental data in the arc attachment zone is important because most of the anode heating occurs there.

As with the current density distribution results, the predicted electron number density distribution $n_{es}(x)$ in the anode sheath layer is dependent on the δ factor. Figure 11 shows n_{es} at all probe locations for 50 mg/sec and 9.8 A, compared with the model with variable δ and $\delta = 1200$ and 3000.

As with the current density predictions, reasonable agreement between experiment and $\delta = 1200$ and 3000 exists for the region $2 - 10$ mm, with $\delta = 1200$ providing a better fit to the experiment at 1 mm.

As discussed, $T_{es} \gg T_g$ near the anode wall, so that a high degree of thermal non-equilibrium exists in the anode boundary layer. This condition results in an elevated population of charged species,³ permitting the conduction of electrical current through the relatively cold gas layer adjacent to the anode.

Figure 13 shows experimental electron temperature determined by two different methods for 50 mg/sec and 9.8 A, compared with the model results with variable and constant δ factors. Higher values of T_{es} are obtained with the "V-I slope" method, and lower values with the " $\phi_f - \phi_s$ " method. Both methods agree at 1 mm, but predict $T_{es} = 22,000$ K vs. $12,000$ K from the model. The $\delta = 1200$ and 3000 cases predict a maximum electron temperature at $x = 2$ mm, in agreement with the V-I method. The model and both experimental methods show that the electron temperature decreases for $x > 2$ mm, and all results predict $T_{es} \gg T_g$.

Both T_{es} methods, V-I slope and $\phi_f - \phi_s$, assume that the electron sheath is thin and collisionless with the electrons exhibiting a Maxwellian distribution. The electron temperature based on the slope appears to be more sensitive to probe contamination, which artificially reduces the slope, raising the calculated T_{es} . It has been observed that even when a probe is "clean," hysteresis is sometimes present on the probe V-I characteristic, introducing uncertainty in the analysis.

Using the electron temperature based on the V-I slope method leads to calculations of j_a which, when integrated over the internal anode surface area,

result in $10 \pm 2.5A$, reasonably close to the I_{arc} value. Using T_{es} based on the $\phi_f - \phi_s$ method results in $I_{arc} = 8 \pm 2A$. However, Fig. 13 shows better agreement between the model T_{es} results and T_{es} based on the $\phi_f - \phi_s$, when compared with the V-I slope method.

In summary, it is difficult to state which method of evaluating T_{es} is better or preferable. The probe V-I characteristic indicates a Maxwellian distribution for the electrons, suggesting that extracting a temperature by this method is appropriate. However, T_{es} based on the plasma potential measurements shows better agreement with the numerical model. The experimental data are also more consistent with measurements by Bufton in the arcjet exit plane,^{8,9} as shown in Fig. 13.

IV. Conclusions

Internal arcjet diagnostics experiments were conducted using fourteen electrostatic micro-probes flush-mounted in the anode of a 1 kW arcjet thruster operating on simulated hydrazine, and compared with a numerical model. It was shown that useful plasma measurements can be obtained with this diagnostic tool in the harsh environment of an arcjet.

Principal conclusions are:

1. All plasma properties were found to be azimuthally symmetric beyond 1 mm downstream of the constrictor.
2. The temperature ratio T_{es}/T_g is much greater than unity in the near-anode region, so that a highly nonequilibrium plasma is present at the wall, requiring separate species energy equations for accurate simulation of the arcjet physics.

3. The propellant flow rate affects the axial location of maximum sheath potential, current density and electron heating more than the arc current.
4. Most of the current density and anode heating occurs within 2 - 4 mm of the constrictor exit.
5. The electron power deposition into the anode accounts for ~18-24% of the total input power, increasing with mass flow rate.
6. The anode sheath potential is everywhere electron-attracting and accounts for over 50% of the anode heating; a weighted effective anode sheath potential varies between 8-17 V depending on the thruster operating conditions.
7. Reasonable agreement between a numerical model and the experimental results was found, using an energy loss factor δ of 1200 in the model.

V. Acknowledgments

The authors acknowledge support by AFOSR/NA under contracts F49620-92-J-0448 and -0280. Dr. Mitat Birkan is the program monitor. We gratefully acknowledge illuminating discussions with Profs. M. J. Kushner and D. Ruzic; critical assistance from W. Johnson, K. Elam, D. Foley, and J. Frizzell of the University of Illinois; advice and equipment support through T. Haag of NASA Lewis Research Center; and assistance in the laboratory from G. Willmes.

VI. References

- ¹Tiliakos, N., *Plasma Properties and Heating at the Anode of a 1 kW Arcjet Using Electrostatic Probes*, Ph. D. Thesis, University of Illinois, 1997.
- ²Curran, F. M., and Haag, T. W., "Extended Life and Performance Test of a Low-Power Arcjet," *Journal of Spacecraft and Rockets*, Vol. 29, No. 4, 1992, pp. 444-452.
- ³Megli, T. W., Lu, J., Krier, H., and Burton, R. L., "Modeling Plasma Processes in 1 kW Hydrazine Arcjet Thrusters," AIAA Paper 96-2965, July, 1996.
- ⁴Langmuir, I., and Mott-Smith, H. M., *Gen. Elec. Rev.*, Vol. 26, 1923, pp. 731; Vol. 27, 1924, pp. 449, 583, 616, 726, 810; *Phys. Rev.*, Vol. 28, 1926, pp. 727.
- ⁵Soulas, G. C., and Myers, R. M., "Mechanisms of Anode Power Deposition in a Low Pressure Free Burning Arc," NASA Contractor Report 194442, IEPC Paper 93-194, Sept., 1993.
- ⁶Gallimore, A. D., Kelly, A. J., and Jahn, R. G., "Anode Power Deposition in Magnetoplasmadynamic Thrusters," *Journal of Propulsion and Power*, Vol. 9, No. 3, May-June 1993, pp. 361-368.
- ⁷Carney, L. M., and Keith, T. G., "Langmuir Probe Measurements of an Arcjet Exhaust," *Journal of Propulsion and Power*, Vol. 5, No. 3, May-June 1989, pp. 287-293.
- ⁸Burton, R. L. and Bufton, S. A., "Exit-Plane Electrostatic Probe Measurements of a Low-Power Arcjet," *Journal of Propulsion and Power*, Vol. 12, No. 6, Nov.-Dec. 1996, pp. 1099-1106.
- ⁹Bufton, S. A., *Exit Plane Plasma Measurements of a Low-Power Hydrazine Arcjet*, Ph. D. Thesis, University of Illinois, 1996.
- ¹⁰Kim, S. W., Foster, J. E., and Gallimore, A. D., "Very-Near-Field Plume Study of a 1.35 kW SPT-100," AIAA Paper 96-2972, 1996.
- ¹¹Sankovic, J. M., "Investigation of the Arcjet Plume Near Field Using Electrostatic Probes," NASA Technical Memorandum 103638, Oct., 1990.
- ¹²Tan, W. P. S., "Transverse Cylindrical Probe in Plasma Diagnostics," *J. Phys. D: Appl. Phys.*, Vol. 6, 1973, pp. 1188-1205.

- ¹³Segall, S. B., and Koopman, D. W., "Application of Cylindrical Langmuir Probes to Streaming Plasma Diagnostics," *Physics of Fluids*, Vol. 16, No. 7, July 1973, pp. 1149-1156.
- ¹⁴Hayes, D. T., and Rotman, W., "Microwave and Electrostatic Probe Measurements on a Blunt Re-Entry Vehicle," *AIAA Journal*, Vol. 11, No. 5, May 1973, pp. 675-682.
- ¹⁵Bredfeldt, H. R., Scharfman, W. E., Guthart, H., and Morita, T., "Boundary-Layer Ion Density Profiles As Measured by Electrostatic Probes," *AIAA Journal*, Vol. 5, No. 1, Jan. 1967, pp. 91-98.
- ¹⁶Boyer, D. W., and Touryan, K. J., "Experimental and Numerical Studies of Flush Electrostatic Probes in Hypersonic Ionized Flows: I. Experiment," *AIAA Journal*, Vol. 10, No. 12, Dec. 1972, pp. 1667-1674.
- ¹⁷Russo, A. J., and Touryan, K. J., "Experimental and Numerical Studies of Flush Electrostatic Probes in Hypersonic Ionized Flows: II. Theory," *AIAA Journal*, Vol. 10, No. 12, Dec. 1972, pp. 1675-1678.
- ¹⁸Tseng, R. C., and Talbot, L., "Flat Plate Boundary-Layer Studies in a Partially Ionized Gas," *AIAA Journal*, Vol. 9, No. 7, July 1971, pp. 1365-1372.
- ¹⁹Zube, D. M., and Myers, R. M., "Techniques for Spectroscopic Measurements in an Arcjet Nozzle," *Journal of Propulsion and Power*, Vol. 8, No. 1, Jan.-Feb. 1992, pp. 254-256.
- ²⁰Zube, D. M., and Auweter-Kurtz, M., "Spectroscopic Arcjet Diagnostic Under Thermal Equilibrium and Nonequilibrium Conditions," *AIAA Paper 93-1792*, June 1993.
- ²¹Glocker, B., and Auweter-Kurtz, M., "Numerical and Experimental Constrictor Flow Analysis of a 10 kW Thermal Arcjet," *AIAA Paper 92-3835*, July 1992.
- ²²Hargus, W., Micci, M., and Spores, R., "Interior Spectroscopic Investigation of the Propellant Energy Modes in an Arcjet Nozzle," *AIAA Paper 94-3302*, June 1994.
- ²³Curran, F. M., Manzella, D. H., and Pencil, E. J., "Performance Characterization of a Segmented Anode Arcjet Thruster," *IEPC Paper 90-2582*, July 1990.
- ²⁴Self, S. A., and Eskin, L. D., "The Boundary Layer Between Electrodes and a Thermal Plasma," *IEEE Transactions on Plasma Science*, Vol. P. S.-11, No. 4, Dec. 1983, pp. 279-285.

²⁵Meeks, E., and Capelli, M. A., "A Multi-Fluid Model of Near-Electrode Plasma Behavior," AIAA Paper 93-2103, June 1993.

²⁶Lichon, P., and Sankovic, J., "Development and Demonstration of a 600 Second Mission Average Arcjet," *Journal of Propulsion and Power*, Vol. 12, No. 6, Nov.-Dec., 1996, pp. 1018-1025.

²⁷Goodfellow, K. D., and Polk, J. E., "Experimental Verification of a High-Current Cathode Thermal Model," AIAA Paper 95-3062, July 1995.

²⁸Laframboise, J. G., "Theory of Spherical and Cylindrical Langmuir Probes in a Collisionless, Maxwellian Plasma at Rest," University of Toronto, Institute for Aerospace Studies, UTIAS Report No. 100, June 1966 (NTIS AD-634596).

²⁹Clements, R. M., and Smy, P. R., "Sheath-Convection Effects with Flush-Mounted Electrostatic Probes," *Canadian Journal of Physics*, Vol. 49, May 1971, pp. 2540-2546.

³⁰Thomas, T. L., and Battle, E. L., "Effects of Contamination on Langmuir Probe Measurements in Glow Discharge Plasmas," *Journal of Applied Physics*, Vol. 41, No. 8, July 1971, pp. 3428-3432.

³¹Swift, J. D., and Schwar, M. J. R., *Electrical Probes for Plasma Diagnostics*, New York American Elsevier Publishing Company, 1969, pp. 220-245.

³²Tiliakos, N. T., and Burton, R. L., "Arcjet Anode Sheath Voltage Measurement by Langmuir Probe," *Journal of Propulsion and Power*, Vol. 12, No. 6, Nov.-Dec., 1996, pp. 1174-1176.

³³Godyak, V. A., and Sternberg, N., *IEEE Trans. Plasma Sci.*, Vol. 18, 1990, pp. 159.

³⁴Oberth, R. C., *Anode Phenomena in High-Current Discharges*, Ph.D. Dissertation, Dept. of Mechanical and Aerospace Engineering, Princeton University, Princeton, N. J., 1970.

³⁵Curran, F. M., "An Experimental Study of Energy Loss Mechanisms and Efficiency Considerations in the Low Power dc Arcjet," AIAA Paper 85-2017, Sept. 1985.

³⁶Miller, S. A., and Martinez-Sanchez, M., "Two-Fluid Non-Equilibrium Simulation of Hydrogen Arcjet Thrusters," *Journal of Propulsion and Power*, Vol. 12, No. 1, 1996, pp. 112-119.

³⁷Sutton and Sherman, *Engineering MagnetoHydrodynamics*, McGraw-Hill, New York, 1965, pp. 148 - 190.

³⁸Martinez-Sanchez, M., and Miller, S. A., "Arcjet Modeling: Status and Prospects," *Journal of Propulsion and Power*, Vol. 12, No. 6, Nov.-Dec., 1996, pp. 1035-1043.

FIGURE CAPTIONS

Fig. 1 Shown above is a schematic of the array of 14 electrostatic micro-probes located at various axial and azimuthal locations. Probes 1, 4, 7, 10 and 1', 4', 7' 10' are used to verify current symmetry.

Fig. 2 Shown above is a drawing to scale of the tungsten probe- Al_2O_3 configuration inside the anode. The probe tip extension is varied between 0 and 0.25-0.3 mm into the plasma flow.

Fig. 3 A typical probe V-I characteristic curve obtained in these experiments is shown with the various regions of interest highlighted.

Fig. 4 Floating potential data for $\dot{m} = 45, 50$ and 60 mg/sec and $I_{\text{arc}} = 9.9 \text{ A}$, and $\dot{m} = 40 \text{ mg/sec}$, $I_{\text{arc}} = 10.6 \text{ A}$, $V_{\text{arc}} = 104 \text{ V}$. Note that the error on the floating potential is $\pm 1 \text{ V}$; the error bars were omitted for clarity.

Fig. 5 Sheath potential for $45, 50$ and 60 mg/sec and $I_{\text{arc}} = 9.9 \text{ A}$, and $\dot{m} = 40 \text{ mg/sec}$ and $I_{\text{arc}} = 10.6 \text{ A}$. In all cases the sheath is electron attracting since $\phi_s > 0$. The error on the sheath potential is $\pm 1 \text{ V}$. Data for probes 1,1' (40 mg/s , 10.6 A) were not available.

Fig. 6 Current density distribution along the anode for $\dot{m} = 45, 50$ and 60 mg/s , 9.8 A and for $\dot{m} = 40 \text{ mg/s}$, 10.6 A .

Fig. 7 Electron number density distribution along the anode for $\dot{m} = 45, 50$ and 60 mg/s , $I_{\text{arc}} = 9.8 \text{ A}$ and for $\dot{m} = 40 \text{ mg/s}$, $I_{\text{arc}} = 10.6 \text{ A}$.

Fig. 8 The anode heating distribution q_e for fixed $I_{\text{arc}} = 9.8 \text{ A}$ and variable flow rate, $\dot{m} = 45, 50$ and 60 mg/s and $I_{\text{arc}} = 10.6 \text{ A}$ for $\dot{m} = 40 \text{ mg/s}$. Error bars are omitted for clarity.

Fig. 9 Comparison between the current density measurements of this work for 50 mg/sec , $I_{\text{arc}} = 9.8 \text{ A}$, $V_{\text{arc}} = 112 \text{ V}$ and the experimental work of Curran *et al.* [1990] for 49.7 mg/sec , $I_{\text{arc}} = 10 \text{ A}$ and $V_{\text{arc}} = 134 \text{ V}$.

Fig. 10 Comparison of experimental and numerical results for current density j_a data at all probe locations. The MKB model was used with both variable δ and constant $\delta = 1200$ and 3000 ; numerical results were taken at $r = 0 \text{ mm}$, i.e. at the wall. The experimental conditions were for $\dot{m} = 50 \text{ mg/sec}$, $I_{\text{arc}} = 9.8$.

Fig. 11 Comparison of experimental and numerical results for n_{es} at all probe locations. The MKB model was used with variable δ and constant $\delta = 1200$ and 3000 ; numerical results were taken at $r = 0$ mm, i.e. at the wall. The experimental conditions were for $\dot{m} = 50$ mg/sec, $I_{arc} = 9.8$ A.

Fig. 12 Experimental results for T_{es} using the V-I slope method, for 3 mass flow rates and 9.8 A.

Fig. 13 Comparison of experimental and numerical results along the anode for T_{es} at all probe locations for 50 mg/s and 10A. The numerical model was used with variable δ and $\delta = 1200$ and 3000 . The T_{es} data point at the exit plane was obtained from the measurements of Ref. 8, with an uncertainty of $\pm 15\%$.

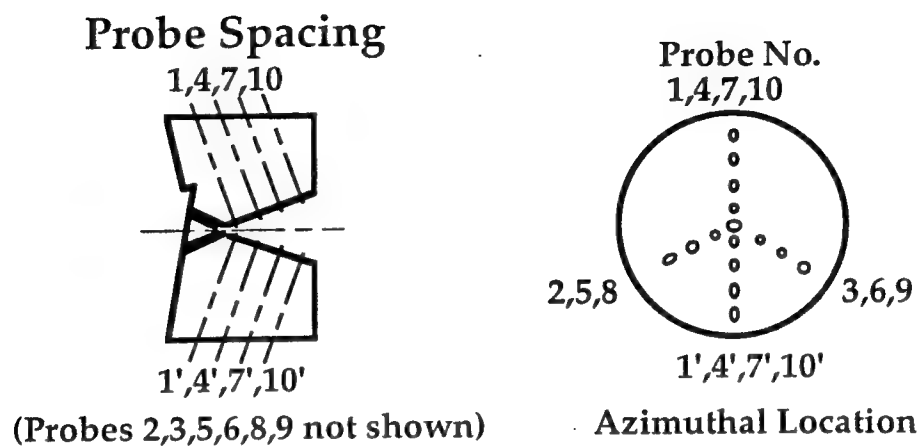


Fig. 1 Schematic of the array of 14 electrostatic micro-probes at millimeter-spaced axial locations. Probes 1, 4, 7, 10 and 1', 4', 7', 10' are used to verify current symmetry.

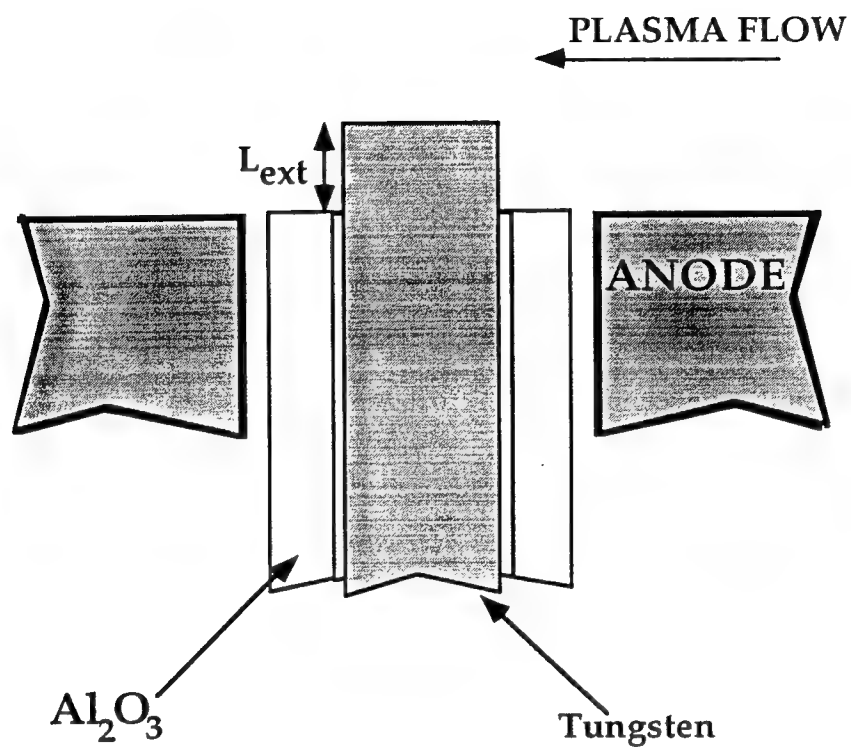


Fig. 2 Shown above is a drawing to scale of the tungsten probe-Al₂O₃ configuration inside the anode. The probe tip extension L_{ext} can be 0.0 - 0.3 mm into the plasma flow, and is set at zero for this paper.

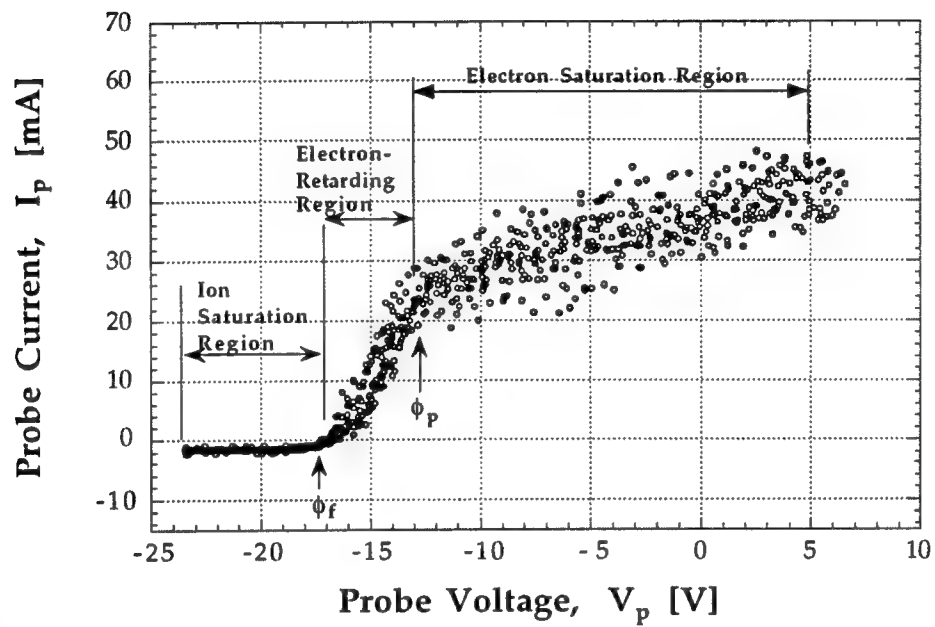


Fig. 3 A typical probe V-I characteristic curve with regions of interest indicated.

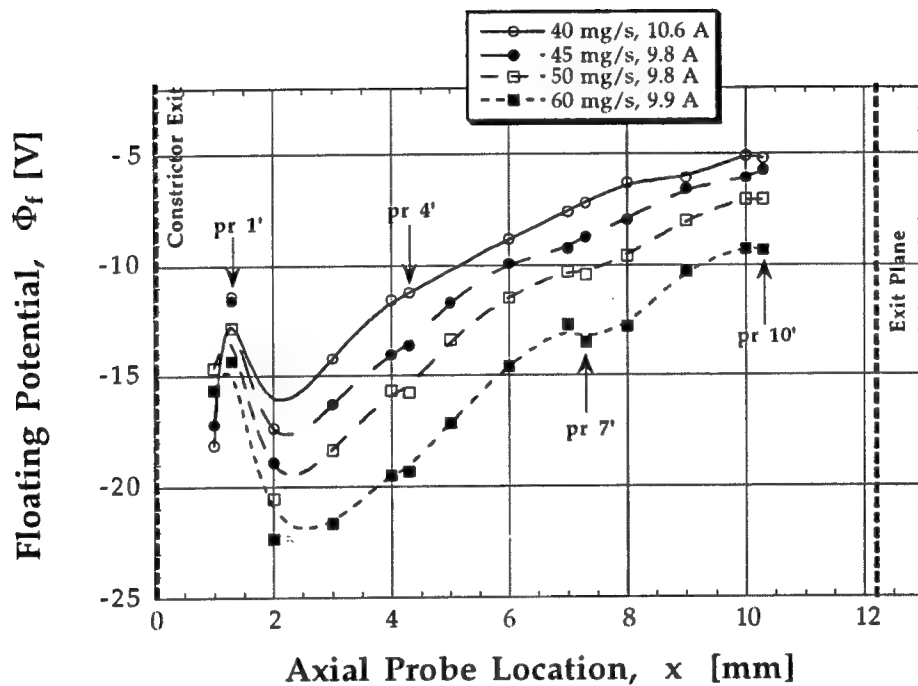


Fig. 4 Floating potential data for 45, 50 and 60 mg/sec and 9.9 A, and 40 mg/sec, 10.6 A, $V_{arc} = 104$ V. The error on the floating potential is ± 1 V; the error bars are omitted for clarity.

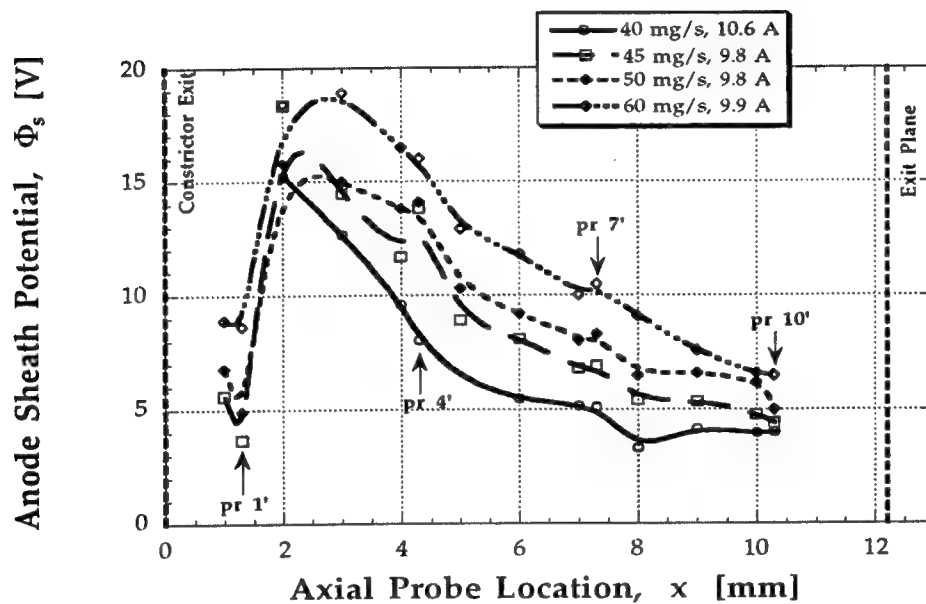


Fig. 5 Sheath potential for 45, 50 and 60 mg/sec and 9.9 A, and $\dot{m} = 40$ mg/sec and 10.6 A. In all cases the sheath is electron attracting since $\phi_s > 0$. The error in the sheath potential is ± 1 V.

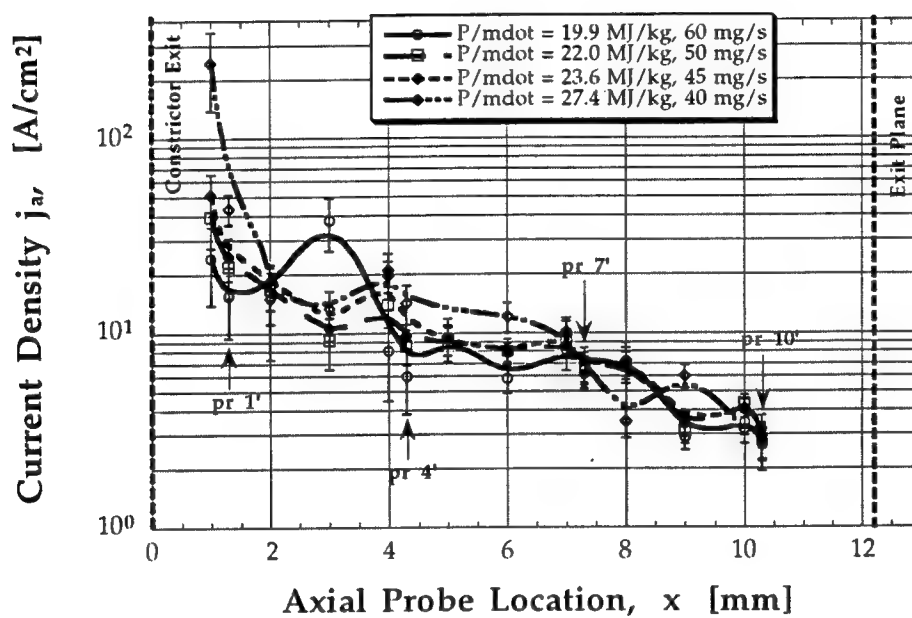


Fig. 6 Current density distribution along the anode for 45, 50 and 60 mg/s, and 9.8A and for 40 mg/s and 10.6A.

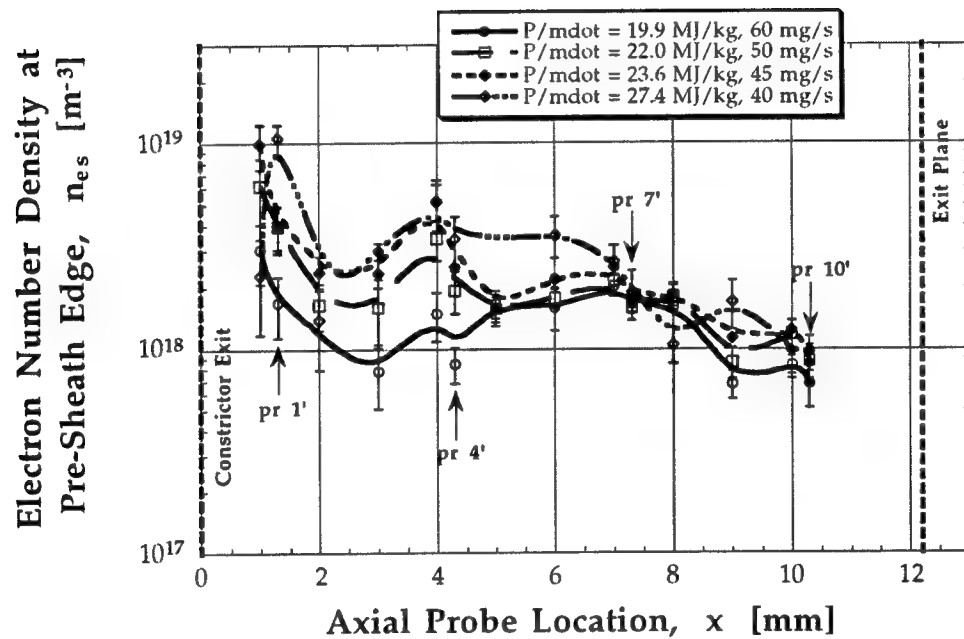


Fig. 7 Electron number density distribution along the anode for 45, 50 and 60 mg/s and 9.8 A, and 40 mg/s and 10.6 A.

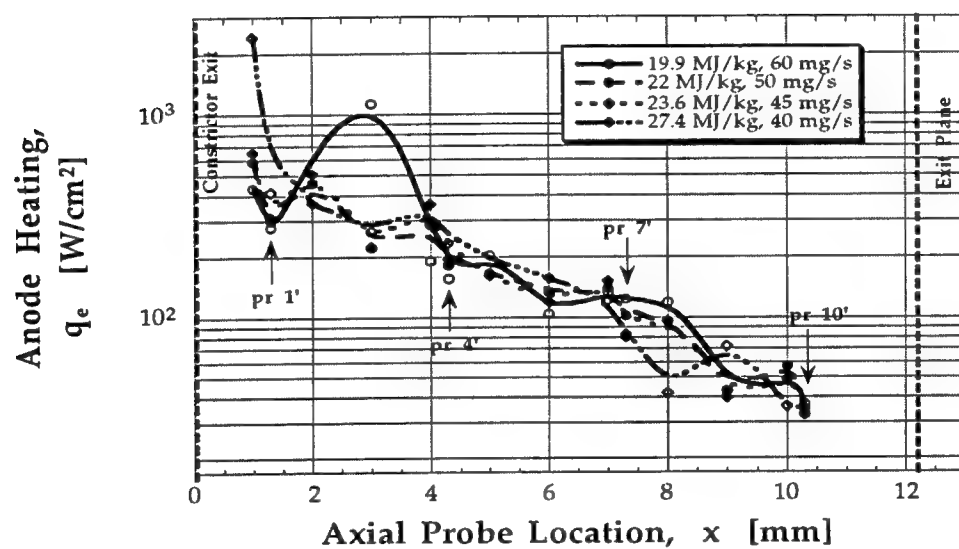


Fig. 8 The anode heating distribution q_e for 45, 50 and 60 mg/s and 9.8 A, and 40 mg/s and 10.6A. Error bars are omitted for clarity.

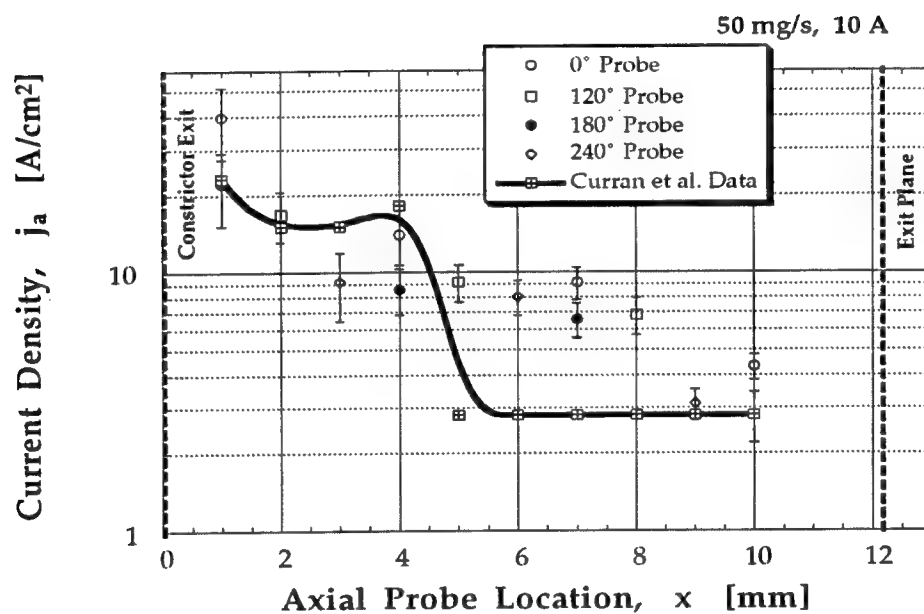


Fig. 9 Comparison between measured current density measurements for 50 mg/sec, 9.8 A, $V_{arc} = 112$ V and Ref. 23 for 49.7 mg/sec, 10 A and $V_{arc} = 134$ V.

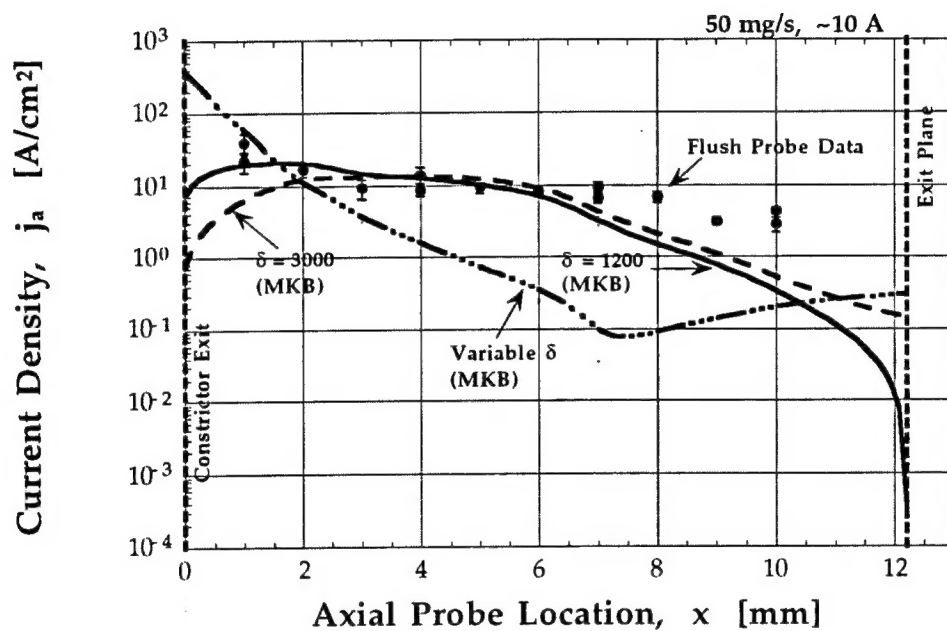


Fig. 10 Comparison of experimental and numerical results for current density at all probe locations. The numerical model was used with both variable δ and constant $\delta = 1200$ and 3000 ; numerical results were taken at the wall. The experimental conditions were 50 mg/sec and 9.8 A .

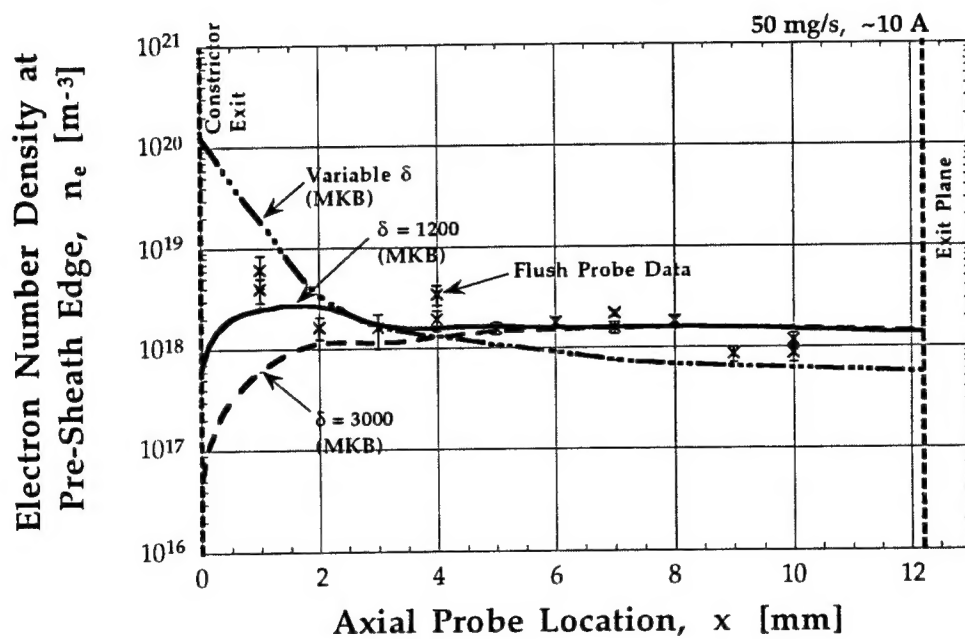


Fig. 11 Comparison of experimental and numerical results for n_{es} at all probe locations. The numerical model was used with variable δ and constant $\delta = 1200$ and 3000 ; numerical results were taken at the wall. The experimental conditions were 50 mg/sec , and 9.8 A .

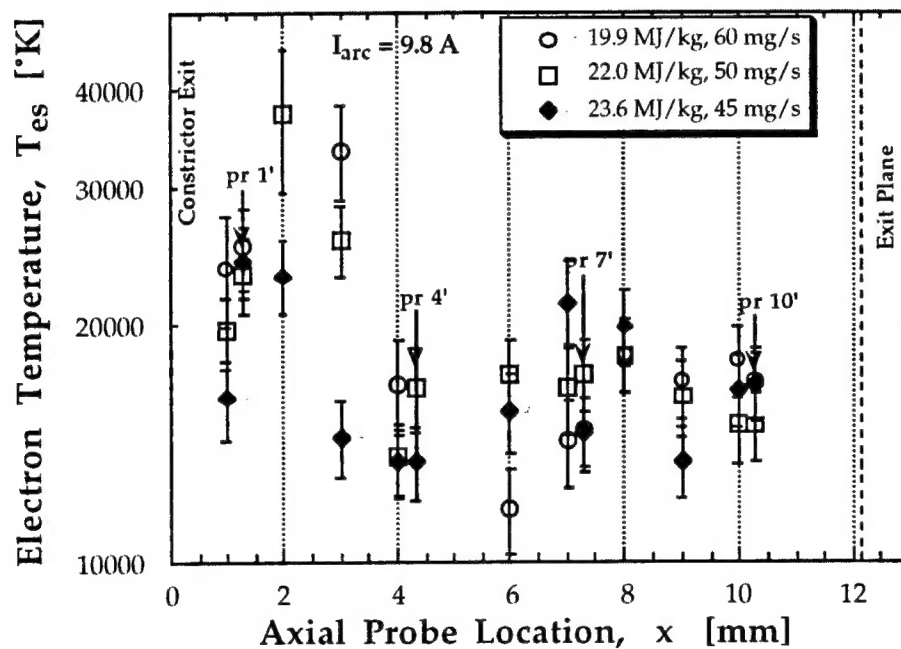


Fig. 12: Electron temperature distributions along the anode for 45, 50, and 60 mg/s and 9.8 A.

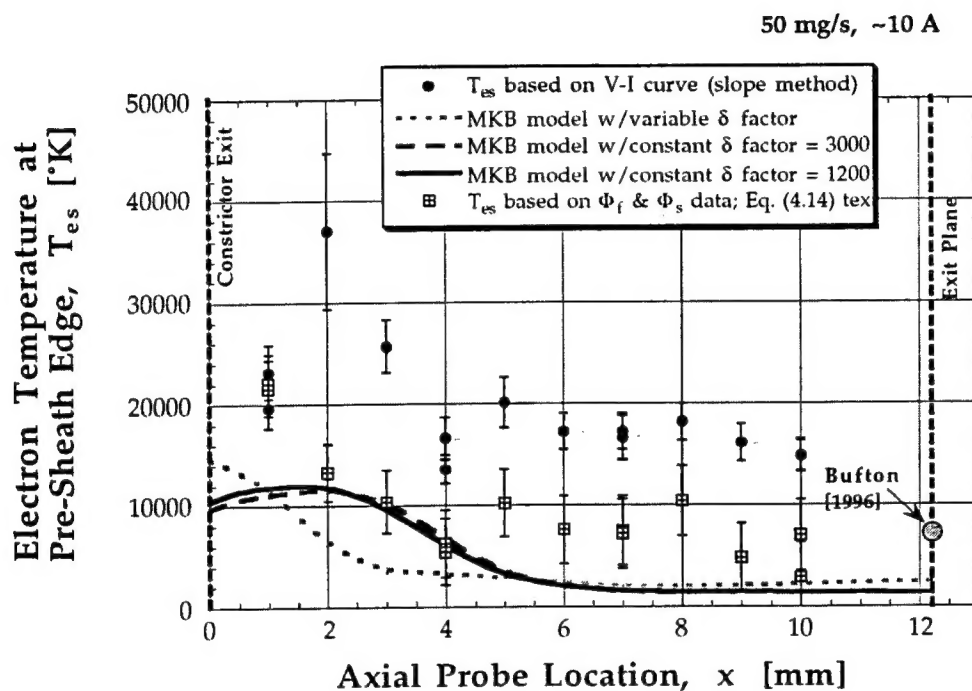


Fig. 13 Comparison of experimental and numerical results along the anode for T_{es} at all probe locations for 50 mg/s and 10A. The numerical model was used with variable δ and $\delta = 1200$ and 3000. The T_{es} data point at the exit plane was obtained from the measurements of Ref. 8, with an uncertainty of $\pm 15\%$.